Sum-frequency generation microscopy: infrared sub-diffractional imaging of surface phonon polaritons

Dissertation

zur Erlangung des Grades eines
Doktors (Dr. rer. nat.)

am Fachbereich Physik
der Freien Universität Berlin

vorgelegt von

Richarda Niemann

Berlin, Dezember 2023

Erstgutachter
Prof. Dr. Martin Wolf
Fritz-Haber-Institut der Max-Planck-Gesellschaft
Abteilung Physikalische Chemie

Zweitgutachterin
Prof. Dr. Katharina Franke
Freie Universität Berlin
Fachbereich Physik

Arbeitsgruppenleiter
Dr. Alexander Paarmann
Fritz-Haber-Institut der Max-Planck-Gesellschaft
Abteilung Physikalische Chemie - Lattice Dynamics Group

Tag der Disputation: **21.02.2024**

FRITZ-HABER-INSTITUT
MAX-PLANCK-GESELLSCHAFT

This work has been performed in the Lattice Dynamics Group of the Department of Physical Chemistry at the Fritz Haber Institute of the Max Planck Society in Berlin between November 2019 and December 2023.

Abstract

Various super-resolution imaging techniques have been established to overcome the diffraction limit of light. However, most of these techniques are limited to resonance imaging in the visible regime, while mid- to far-infrared (IR) approaches are rare. The prime tool for IR super-resolution microscopy is scattering-type scanning near-field optical microscopy (s-SNOM). In nanophotonics, s-SNOM is often employed to study phonon polaritons (PhPs), quasi-particles which enable light confinement to length scales far below the diffraction limit. Although s-SNOM has provided great insight to PhPs, the technique often suffers from long image acquisition times, due to the point-scanning approach, and the limitation for the applied laser power to avoid laser induced damage.

This thesis introduces a novel approach to IR sub-diffractional imaging of phonon polaritons by wide-field sum-frequency generation (SFG) microscopy. Here, the IR electric fields of phonon polaritons are upconverted with a visible laser, resulting in a non-linear SFG signal. This provides IR resonance information and a spatial resolution of 1.4 µm ($\sim \lambda_{IR}/9$) that is well below the IR-diffraction limit. By using a tunable IR free-electron laser (FEL), polaritons can be excited across the whole mid- to far-IR range.

In this work, the newly-developed SFG microscope is first employed for interferometric imaging of propagating surface PhPs on an AlN substrate. A detailed analysis gives insight into the anisotropy- and polarization-dependent dispersion of the propagating modes. Structuring substrates with microresonators leads to confinement on the µm-scale and the observation of localized PhPs. By employing SiC 1D resonator chains with lengths from one to several resonators, the formation of a collective response is detected, originating from coupling between the individual localized polaritons.

The thesis continues with the observation of hybridization of localized and propagating polaritons in a 2D metasurface consisting of SiC microresonators on a SiC substrate. Spectro-microscopy allows for two complementary approaches to measure the hybridized polariton dispersion, namely angle-dependent resonance imaging and polariton interferometry. The analysis reveals the effect of strong coupling on the localization of polaritons, as well as the formation of edge states.

Moving from cylindrical to elongated rod-like resonators, standing waves inside the rods are observed despite losses to the substrate. SFG imaging reveals tunable resonances by changing the rod's length which is in good agreement with s-SNOM experiments and simulations.

Overall, this work introduces a novel technique for IR sub-diffractional imaging, which is extensively employed to study PhPs. The findings form a basis for future applications and investigations of PhPs in nanophotonic devices.

Kurzfassung

Super-Resolution-Mikroskopie ist eine vielfältig angewandte Methode, um das natürliche Auflösungslimit von Licht zu umgehen. Die meisten etablierten Techniken sind allerdings auf resonante Mikrokopie im sichtbaren Spektralbereich limitiert, während es nur wenige Ansätze für den mittel- bis fern-infraroten (IR) Bereich gibt. Für hochauflösende IR-Mikroskopie ist optische Rasternahfeldmikroskopie (s-SNOM) das gängige Instrument. s-SNOM wird häufig für Experimente an Phononpolaritonen (PhPs) eingesetzt, durch die Licht auf Längenskalen unterhalb des Auflösungslimits lokalisiert werden kann. Mittels s-SNOM wurden viele Erkenntnisse über PhPs gewonnen, allerdings limitieren langsame Bildgenerierung sowie der niedrige Schwellwert für laserverursachte Schäden diese Punktraster-Technik.
Diese Arbeit stellt einen neuen Ansatz zur hochauflösenden IR Mikroskopie von PhPs vor, der auf Weitfeld-Summenfrequenzerzeugung (SFG) basiert. Dabei werden die IR Felder der PhPs durch einen sichtbaren Laser upkonvertiert, was die Resonanzinformationen des IR mit der räumlichen Auflösung eines sichtbaren Lasers kombiniert. Durch diese Technik wird eine Auflösung von $1.4\,\mu m$ ($\sim \lambda_{IR}/9$) erreicht, die weit unter dem natürlichen IR Auflösungslimit liegt. Durch einen durchstimmbaren IR freien Elektronenlaser (FEL) ermöglicht diese Technik hochauflösende Mikroskopie im gesamten mittel- bis fern-IR Spektralbereich.
Die Arbeit zeigt, wie SFG basierte Spektro-Mikroskopie für interferometrische Bildgebung propagierender SPhPs verwendet werden kann. Dabei konnten Erkenntnisse über die Anisotropie- und Polarisationsabhängigkeit der propagierenden Polaritonen in AlN gewonnen werden. Zudem wurde die Lokalisierung von IR Licht in Mikroresonatoren aus SiC beobachtet, in denen sich lokalisierte Polaritonen ausbilden. In Messungen an 1D-Ketten aus solchen Resonatoren wurden kollektive Moden beobachtet, die durch die Kopplung der lokalisierten Polaritonen entstehen.
Der Übergang von 1D-Ketten zu 2D-Gittern ermöglichte die Untersuchung von lokalisierten und propagierenden SPhPs auf Metaoberflächen. Dabei konnte die Hybridisierung beider PhP-Arten beobachtet werden. Spektro-Mikroskopie ermöglichte hier zwei komplementäre Ansätze zur Messung der Ausbreitung der hybridisierten Polaritonen: winkelabhängige, resonante Bildgebung und Polaritoneninterferometrie. Dabei konnte der Einfluss starker Kopplung auf die Lokalisierung der Polaritonen sowie die Entstehung von Kantenzuständen untersucht werden.
Wechselt man von zylindrischen auf längliche, stabartige Resonatoren, konnten stehende Wellen innerhalb der Resonatoren trotz Verlusten an das Substrat beobachtet werden. Die Resonanzen konnten hier durch geänderte Längen der Resonatoren beeinflusst werden, was auch in s-SNOM Experimenten und Simulationen beobachtet wurde.
Insgesamt stellt diese Arbeit eine neue Technik für hochauflösende IR-Mikroskopie vor, die für umfangreiche Experimente an PhPs genutzt wurde. Die Ergebnisse bilden einen Grundstein für zukünftige PhP-Anwendungen in nanophotonischen Bauteilen.

Contents

1

Introduction

With the emergence of the field of nanophotonics, research on light-matter interactions has become an important and intensively studied field of interest. Particular focus has been placed at achieving a profound understanding of light confinement effects at length scales far below the diffraction limit of light [1]. Structuring of materials enables light confinement to the nanoscale, which leads to tremendous enhancement of the electrical fields compared to free-space propagating light. Such enhanced fields are of great interest for, e.g., photovoltaic devices [2, 3] and sensing applications [4, 5]. Additionally, the diminutive length scales constitute an excellent basis for the size reduction of optoelectronic devices such as on-chip detectors [6] or nanolasers [7].

In the past decades, one main component for nanophotonics was the surface plasmon polariton (SPP), a quasi-particle arising due to the coupling of light to the collective charge motion inside a metal (plasmon) [8–11]. Discoveries based on the SPP include the application of surface-enhanced Raman spectroscopy [12], increased data storage [13] and plasmon-enhanced fluorescence spectroscopy [14]. Recent studies, however, have started to focus on the surface phonon polariton, as an alternative approach in nanophotonics. A phonon polariton is an electro-magnetic excitation resulting from strong coupling of light to a lattice vibration (phonon) [15–17]. These quasi-particles are promising candidates for overcoming limitations of the plasmon polariton which suffers from high losses and correspondingly short life times [15]. Thus, phonon polaritons are a promising tool in mid-infrared nanophotonics, and are currently revolutionizing the manipulation of light on a sub-wavelength scale.

With the accomplishment of light confinement to length scales far below the diffraction limit, the route towards sub-diffractional resolution microscopy techniques becomes more and more important. Super-resolution can, by now, be reached with a variety of techniques, based on different approaches, such as fluorescence-based microscopy or tip-based microscopy. The most common microscopy technique for research on phonon polaritons nowadays is scattering-type scanning near-field optical microscopy (s-SNOM) [18, 19]. As a nanotip-based technique, the resolution mainly depends on the miniature size of the tip, rather than on the imaging wavelength. Therefore, resolutions on the order of 10 nm have been reported [18]. Despite its great spatial resolution, s-SNOM, however, suffers from long acquisition times due to its point-scanning nature, and limited power operation due to sample damage induced by tight focusing. Moreover, a nanotip-based influence on the sample is a source for additional noise [20]. Alternatives are mainly based on fluorescence, e.g.,

structured illumination microscopy or stimulated emission depletion microscopy, limiting the sample range to fluorescent or functionalized samples and, thus, imaging in the visible [21].

An attractive alternative to these established techniques is provided by nonlinear optical frequency-mixing approaches such as sum-frequency generation (SFG). In an SFG microscope, the resonant far-IR light is upconverted by a second laser, usually in the visible regime, leading to the generation of a new visible beam with the resonance information provided by the IR and a resolution limited by the diffraction limit of visible light [22]. In a wide-field approach, obstacles, such as long acquisition times and sample damage as well as sample limitations, can be avoided. Although SFG microscopy is a common tool in biological imaging, the goal of subdiffractional imaging is a novel approach, as the ratio of the excitation and upconversion lasers is smaller in previously reported experiments [23–25]. In combination with a far-IR tunable light source, SFG wide-field microscopy makes an ideal tool for sub-diffractional imaging of phonon polaritons, which has not been reported before this work.

This thesis describes a novel technique for IR sub-diffractional imaging, which is intensely used to study surface phonon polaritons. To provide the basic knowledge on phonon polaritons, Chapter 2 discusses the theoretical basics of these light-matter interactions. Starting with the basic concept of a bulk phonon polariton, the chapter introduces more and more precise kinds of polaritons from bulk to surface phonon polaritons, including propagating and localized polaritons, and their hybridization with one another. The principle of strong coupling is introduced to fully prepare for the discussion of the results in later chapters.

The necessary basics for the technique of sum-frequency generation microscopy are provided in Chapter 3. Here, general light microscopy and different techniques of super-resolution microscopy are discussed and compared. Nonlinear optics is introduced, before discussing the specific concept of sum-frequency generation in greater detail. Different types of SFG microscopes are discussed and compared regarding their advantages and disadvantages.

Chapter 4 provides insight into the laser systems and methods used for this thesis. The general concept of a free-electron laser (FEL) is explained, before introducing the FHI-FEL in greater detail. In addition, the table-top laser systems used for the SFG experiments are discussed and analyzed, before introducing the final setup of the SFG wide-field microscope. The microscope is further characterized in Chapter 5, where the IR sub-diffractional resolution is determined and general advantages of the technique, such as spectro-microscopy, are introduced.

After the theoretical discussion of propagating and localized polaritons, the upcoming chapters discuss these and their hybridization experimentally.
First, the possibility of imaging propagating polaritons, as frequently done with techniques such as s-SNOM, is demonstrated in Chapter 6, theoretically and experimentally using MoO_3 flakes on an AlN substrate. The results show a large

dependency on the IR frequency and are analyzed via dispersion plots. The effect of the anisotropy of the used materials is discussed, as well as the effect of directional launching of propagating waves, due to polarization sensitivity. Open questions are touched, such as considering interesting effects when using s-polarized light, and the response of the MoO_3 flake itself to the IR excitation.
In Chapter 7, localized polaritons in microresonators of SiC are discussed. The content bridges the gap between the discussion of single resonators and large resonator arrays by focusing on localized resonators in finite one-dimensional (1D) chains. Here, the build up of 1D collective modes is studied by stepwise increasing the number of resonators in a chain.
Thereafter, the hybridization of propagating and localized polaritons is a point of discussion in Chapter 8. Two complementary approaches of measuring the strong coupling dispersion are introduced, which are simultaneously achieved with the SFG spectro-microscopy setup. The data also provide access to polariton propagation lengths and edge states, which open the discussion of the effect of strong coupling to localized resonances on the propagation of polaritons.

After discussion of resonators much smaller than the IR wavelength, Chapter 9 introduces phonon polariton standing waves in microrods with lengths comparable to the IR excitation wavelength. Recent publications demonstrated the appearance of such polaritonic standing waves in rod-like structures, however, experiments in this thesis focus on individual rods on a same-material substrate which has not been studied so far. It is shown that light confinement is achieved, despite losses to the substrate. Furthermore, the microrods seem to act as excellent launchers for propagating waves on the substrate which is briefly touched in the chapter's outlook.

Finally, a general outlook is given in Chapter 10 where the applicability of the SFG microscope, not only for various phonon polariton platforms, but also for photonic structures or other physico-chemical systems is highlighted.

2

Theoretical Background: Phonon Polaritons

This chapter introduces the basics of phonon polaritons. After a short introduction on polaritons, bulk phonon polaritons will be described, Sec. 2.1, and the dielectric function and the dispersion relation are derived. The rest of the chapter will place emphasis on surface phonon polaritons, which are introduced in Sec. 2.2. The special case of localized modes in resonators is discussed in Sec. 2.3 and the hybridization of these modes and surface polaritons in the strong coupling regime is discussed in Sec. 2.4.

Nanophotonics relies on light-matter interactions. Light can be described as electromagnetic waves by Maxwell's equations. In matter, here specifically crystals, eigenfunctions of excited states can also be regarded as plane waves, but in this case of a polarization field [26]. The hybridization of these electro-magnetic waves with polarization waves leads to mixed light-matter states, known as polaritons [27]. The concept of polaritons has first been introduced by Huang in 1951 [28].
Different kind of polaritons are distinguished according to the kind of polarization wave in the crystal. A distinction is made between, e.g., exciton waves [29], plasmon waves [30] and optical phonon waves [31]. This leads to exciton-, plasmon-, and phonon-polaritons [32].

The dispersion of a bulk polariton in a three-dimensional material is illustrated in Fig. 2.1. The material's resonance frequency (dashed line) can be approximated as horizontal line, i.e., a flat dispersion, since the wavevector $\mathbf{k}$ is much smaller than the material's Brillioun zone. It has a theoretical crossing point with the linear dispersion of the photon field (dotted line), where an avoided crossing arises.[1] This leads to two individual polariton branches, known as the upper and lower polariton branch, respectively. The anti-crossing leads to a polaritonic band gap with no allowed optical states, called the Reststrahlen (German for 'residual rays') band. This band gap gives rise to propagating waves at the boundaries of the material called surface polaritons. This will be discussed in more detail within this chapter. The bulk polariton dispersion shown in Fig. 2.1 applies to all the polariton types.

In the field of nanophotonics already outlined in Chapter 1, plasmon polaritons played a key role. Phonon polaritons gained significant attention due to their application in the mid-IR regime and low optical losses, leading to long lifetimes and propagation lengths. The photon coupling to phonons, i.e., crystal lattice vibrations, is significant only in polar crystals [15]. A polar crystal does not have a permanent

[1] The avoided crossing is a result of strong coupling, which is discussed in detail in Sec. 2.4.1.

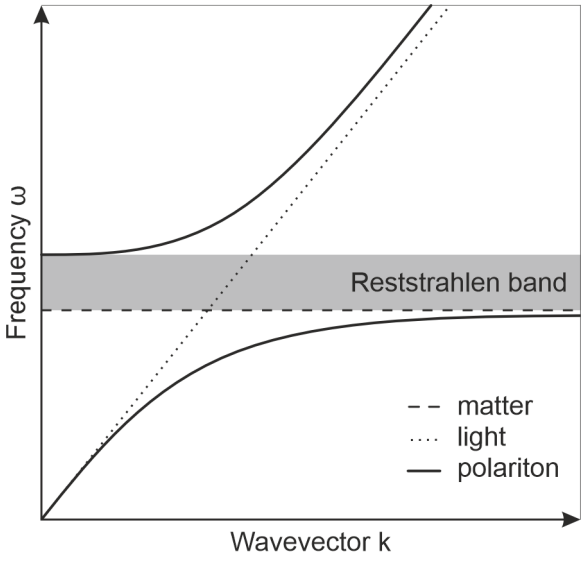

Figure 2.1. *Bulk polariton dispersion.* The coupling of a polarization wave (dashed line) to an electro-magnetic wave (dotted line) leads to an avoided crossing with a splitting into an upper and lower polariton branch (solid lines). Between these branches, a polaritonic band gap is formed, the so-called 'Reststrahlen band' (gray shaded area). Typically, the material resonance is non-dispersive (horizontal line) while the light dispersion is linear.

polarization, because the charge separations cancel to zero net total dipole. When interacting with an incoming light field, a net dipole moment and a resulting polarization is induced. This is true for a variety of materials. In fact, ten out of the 32 crystal classes are polar [33].

2.1 Bulk phonon polaritons

In 1900, the physicist Paul Drude established a model for the movement of free electrons in a metal, which sufficiently describes the optical response for the case of plasmon polaritons [34]. For electrons which are bound to a nucleus instead, the Drude model has to be extended by adding a restoring force term, which was done by Hendrik Lorentz leading to the so-called Lorentz model [35]. Although designed for electrons, the model can be applied to any kind of charged particles with a restoring force. Thus, it is also valid for ions or partially charged atoms in a crystal lattice and can therefore be used to analyze phonon polaritons.

The corresponding equation of motion for a lattice vibration can be written as

$$\mu\ddot{x} + \mu\gamma\dot{x} + \mu\omega_0^2 x = e^* E. \tag{2.1.1}$$

Here, μ is the reduced mass of the oscillating ions and e^* the Born effective charge taking into account the polarity of the crystal unit cell [36]. x is its one-dimensional displacement from the equilibrium position, γ is the damping constant, and ω_0 the

resonance frequency of the phonon polariton in the harmonic potential. The electromagnetic field of the incident light E is given by $E = E_0 e^{i\omega t}$ with ω being the corresponding frequency. Following the typical ansatz of $x = x_o e^{i\omega t}$, the equation of motion can be solved by

$$x = \frac{e^* E}{\mu \left(\omega_0^2 - \omega^2 + i\omega\gamma\right)}. \tag{2.1.2}$$

The response of a material is described through a group of oscillators, with a density of unit cells $n = 1/V_{\mathrm{uc}}$, where V_{uc} is the unit cell volume, giving rise to the polarization

$$P = ne^* x = \varepsilon_0 \left(\varepsilon - 1\right) E, \tag{2.1.3}$$

with ε_0 the permittivity in vacuum. Considering also the non-resonant electronic contributions ε_∞, the dielectric permittivity can be written as

$$\varepsilon\left(\omega\right) = \varepsilon_\infty + \frac{ne^{*2}}{\varepsilon_0 \mu} \frac{1}{\omega_0^2 - \omega^2 + i\omega\gamma}. \tag{2.1.4}$$

To determine the resonance frequency ω_0, crystal lattice modes have to be considered. A crystal combining N atoms in its unit cell supports three acoustic modes and $3N - 3$ optical modes [37]. Here, only the optical modes are considered, which are further subclassified into transverse optical (TO), and longitudinal optical (LO), depending on the polarization of the wave with respect to the propagation direction, which is shown in Fig. 2.2 [15]. In contrast to non-polar crystals, the resonance frequencies ω_{TO} and ω_{LO} are not equal at the zone center of the Brillouin zone in polar crystals, leading to a gap with $\omega_{\mathrm{LO}} > \omega_{\mathrm{TO}}$ [38]. Since the LO is a longitudinal wave ($\mathbf{k} \parallel \mathbf{P}$), it cannot be excited by (transversal) electromagnetic waves, leaving the TO mode as the only resonance frequency in a polar crystal, $\omega_0 = \omega_{\mathrm{TO}}$. The formation of a polariton leads to the formation of the Reststrahlen band, whose width is interestingly given by exactly the LO-TO splitting. This is because the upper polariton coincides with the LO phonon frequency at the Brillouin zone center.

A longitudinal mode corresponds to a zero-crossing of the dielectric permittivity [39]. Hence, to express Eq. (2.1.4) not only in terms of ω_{TO}, but also ω_{LO}, it can be solved for $\varepsilon\left(\omega_{\mathrm{LO}}\right) = 0$:

$$\omega_{\mathrm{LO}}^2 = \frac{ne^{*2}}{\varepsilon_\infty \varepsilon_0 \mu} + \omega_{\mathrm{TO}}^2. \tag{2.1.5}$$

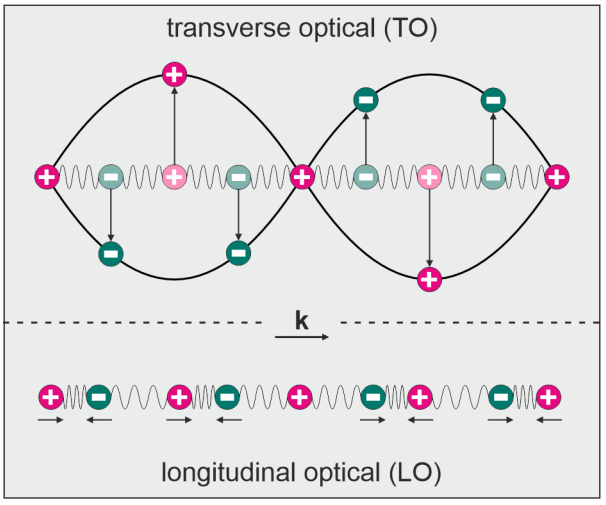

Figure 2.2. *Atomic vibrations of optical lattice modes.* The transverse optical modes (top) oscillate orthogonal to the propagation direction while the longitudinal optical modes (bottom) oscillate along the propagation direction given by the wavevector **k**.

Implementing this expression into Eq. (2.1.4) leads to the dielectric function

$$\varepsilon(\omega) = \varepsilon_\infty \left(1 + \frac{\omega_{\mathrm{LO}}^2 - \omega_{\mathrm{TO}}^2}{\omega_{\mathrm{TO}}^2 - \omega^2 - i\omega\gamma}\right). \tag{2.1.6}$$

Solving this equation for $\varepsilon(0)$, i.e. the low-frequency limit, leads to

$$\left(\frac{\omega_{\mathrm{LO}}}{\omega_{\mathrm{TO}}}\right)^2 = \frac{\varepsilon(0)}{\varepsilon_\infty}, \tag{2.1.7}$$

which is known as the Lyddane-Sachs-Teller relation [40]. It directly shows the correspondence of a large Reststrahlen band width ($\omega_{\mathrm{LO}}/\omega_{\mathrm{TO}}$ large) to a large refractive index $n = \sqrt{\varepsilon(\omega)}$ below the Reststrahlen band.

Figure 2.3(a) shows the dielectric function of 4H-SiC, following Eq. (2.1.6). The dielectric function is complex-valued, with the real part (blue) describing to first-order an approximation of the material dispersion and the imaginary part (orange) the optical absorption. In the low-frequency limit, $\Re[\varepsilon(\omega \to 0)]$ approaches the static dielectric constant ε_{s} ($\equiv \varepsilon(0)$), while it approaches the optical dielectric constant ε_∞ in the high-frequency region [38].

The dashed lines mark the TO and LO resonance frequencies ω_{TO} and ω_{LO}, respectively. The imaginary part of the dielectric function has its peak value at the TO resonance where light is absorbed by coupling to the TO mode. The real part has two zero-crossings at ω_{TO} and ω_{LO}, leading to $\Re(\varepsilon) < 0$ for the whole region of the Reststrahlen band. The negative permittivity leads to a reflectivity close to 100 % across the entire Reststrahlen band, as can be seen in Fig. 2.3(b). Here, only

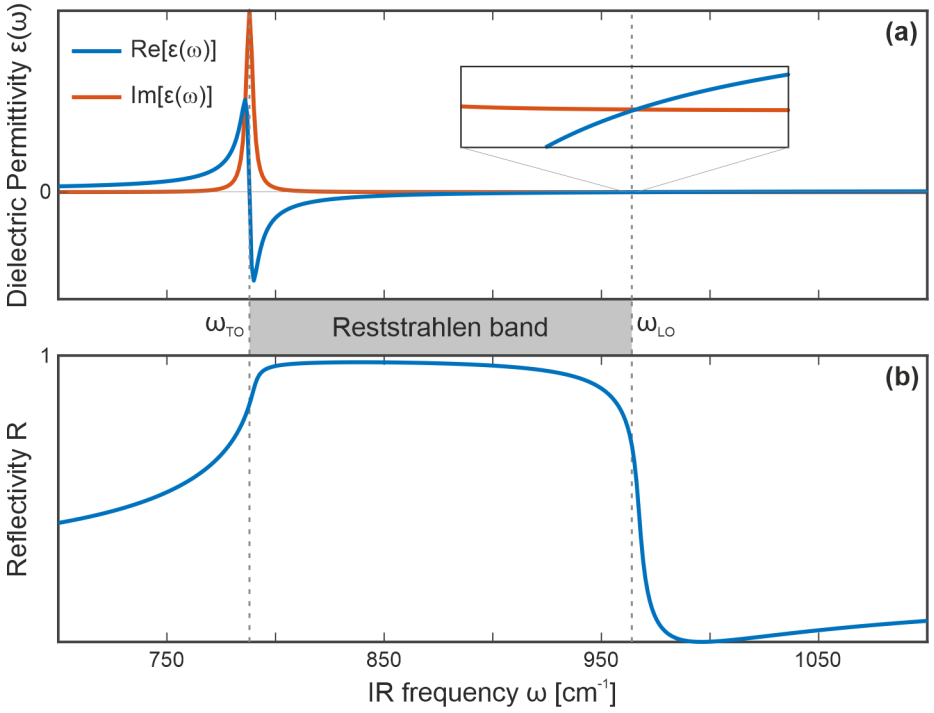

Figure 2.3. *Dielectric function and reflectivity of 4H-SiC.* (a) Real (blue) and imaginary (orange) parts of the dielectric permittivity. The region of $\mathrm{Re}(\varepsilon) < 0$ marks the Reststrahlen band bounded by the transverse optical (ω_{TO}) and the longitudinal optical (ω_{LO}) resonance frequencies (dashed lines). (b) The reflectivity inside the Reststrahlen band is close to unity, prohibiting light propagating in this region.

evanescent decay appears, but no light propagation into the crystal is supported due to coherent oscillations of the optical phonons leading to a metallic behavior of the crystal [15]. The reflectivity of the material for illumination under normal incidence can be calculated using the dielectric function following [41]

$$R = \left| \frac{\sqrt{\varepsilon(\omega)} - 1}{\sqrt{\varepsilon(\omega)} + 1} \right|^2 . \tag{2.1.8}$$

Bulk phonon polaritons (BPhPs) are only permitted outside the Reststrahlen band. Light propagation, on the other hand, is possible on the material surface in the form of surface phonon polaritons (SPhPs).

The dispersion of the BPhPs can be calculated using the refractive index n, with $\mathbf{k}_{\mathrm{BPhP}} = \frac{\omega}{c} n(\omega)$ and $n(\omega) = \sqrt{\varepsilon(\omega)}$ [26], producing a dispersion relation:

$$k_{\mathrm{BPhP}} = \frac{\omega}{c} n(\omega) = \frac{\omega}{c} \sqrt{\varepsilon(\omega)} = \frac{\omega}{c} \sqrt{\varepsilon_\infty \left(1 + \frac{\omega_{\mathrm{LO}}^2 - \omega_{\mathrm{TO}}^2}{\omega_{\mathrm{TO}}^2 - \omega^2 - i\omega\gamma} \right)}, \tag{2.1.9}$$

leading to the two polariton branches as depicted in Fig. 2.1. The physical origin of the two individual branches will be subject of discussion in Sec. 2.4.1. This dispersion

can be compared against that of light in vacuum/air, were $n = 1$, producing a straight line (referred to as light line).

2.2 Surface phonon polaritons

The frequency region $\omega_{\mathrm{TO}} < \omega < \omega_{\mathrm{LO}}$ is of central importance in the context of this thesis. In this region, no propagating bulk modes are supported. As will be expanded upon below, the electromagnetic field strength is exponentially decreasing into the material, because the incoming light cannot propagate into the crystal, and the polariton modes only exist on the crystal surface. This is illustrated in Fig. 2.4. The electromagnetic field strength of the wave has its maximum at the surface ($z = 0$) and has an exponential decay in both directions, i.e., into air ($z > 0$) and into the substrate ($z < 0$), while the decay into the substrate is stronger because of the suppressed bulk mode.

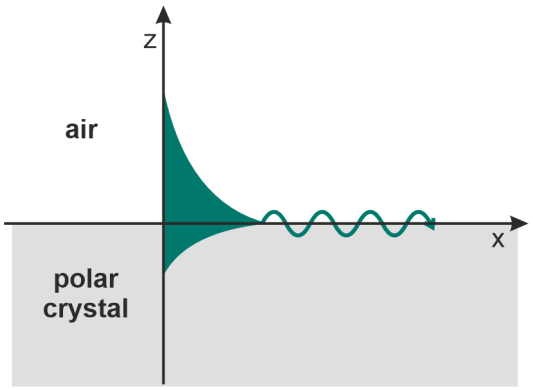

Figure 2.4. *Propagating phonon polariton wave on a crystal surface.* The electromagnetic field strength (green area) decays strongly with increasing depth into the substrate, z>0: air, z<0: polar crystal. The phonon polariton mode is localized on the surface and can only propagate along it. Adapted from [42].

The fields can be expressed as [42]

$$\begin{aligned} E_1 &= E_1^0 e^{ik_{\mathrm{x}} + \kappa_1 z} \\ E_2 &= E_2^0 e^{ik_{\mathrm{x}} - \kappa_2 z}, \end{aligned} \tag{2.2.1}$$

with $z < 0$ for E_1 and $z > 0$ for E_2. 1,2 denote the two media, i.e., a polar crystal and air, k_{x} is the wavevector in the direction of the propagating wave and $\kappa_{1,2}$ denote the imaginary part of the z-components of the wavevectors in the respective media with

$$\kappa = ik_{\mathrm{z}} = i\sqrt{\varepsilon\omega^2/c^2 - k_{\mathrm{x}}^2} \tag{2.2.2}$$

with the purely imaginary out-of-plane momentum $k_z = \sqrt{\varepsilon\omega^2/c^2 - k_{\mathrm{x}}^2}$ [26]. These equations satisfy Maxwell's equations for p-polarized light and together with the

boundary conditions at the crystal surface, $E_1^0 = E_2^0$, it follows

$$-\frac{\kappa_1}{\varepsilon_1} = \frac{\kappa_2}{\varepsilon_2}. \tag{2.2.3}$$

This relation shows that a surface mode can only exist if the dielectric functions of the two media have opposite signs. Since κ_1, κ_2 and ε_2 ($\equiv \varepsilon_{\text{air}} = 1$) are positive by definition [43], a SPhP mode is only supported for $\varepsilon_1 < 0$ which is the case only inside the Reststrahlen band.

By plugging Eq. (2.2.2) into Eq. (2.2.3), the dispersion relation for SPhPs can be formulated as

$$k_{\text{x}} = k_{\text{SPhP}} = \left(\frac{\omega}{c}\right)\sqrt{\frac{\varepsilon_1\varepsilon_2}{\varepsilon_1 + \varepsilon_2}}. \tag{2.2.4}$$

The real part of k_{SPhP} describes the compression of the light wavelength, when guided along the crystal surface, while the imaginary part expresses the attenuation of the mode along its propagation [42].
For an interface with air, the SPhP dispersion Eq. (2.2.4) simplifies to

$$k_{\text{SPhP}} = \frac{\omega}{c}\sqrt{\frac{\varepsilon(\omega)}{\varepsilon(\omega) + 1}}. \tag{2.2.5}$$

The difference between the dispersion relations for bulk, Eq. (2.1.9), and surface, Eq. (2.2.5), polariton arises from the denominator $\varepsilon(\omega)+1$, which appears due to the continuity conditions on the sample surface [26]. The calculated dispersion relations for bulk and surface phonon polaritons in 4H-SiC are plotted in Fig. 2.5. The BPhP modes (black lines) split into two branches and only exist outside the Reststrahlen band. The lower branch converges to $\omega/c\sqrt{\varepsilon(0)}$ for $\omega \to 0$, while the upper polariton branch converges to $\omega/c\sqrt{\varepsilon_\infty}$ for $\omega \to \infty$, following from Eqs. (2.1.6) and (2.1.7). The bulk phonon polariton becomes localized as propagating into the substrate is not supported anymore at ω_{TO} with $k_{\text{BPhP}} \to \infty$ for $\omega \to \omega_{\text{TO}}$. Inside the Reststrahlen band, only SPhP modes with wavevectors larger than that of photons in air are supported. The lower limit of supported SPhP eigenfrequencies is the TO frequency, the upper limit is given by a cut-off frequency[2] ω_{S} [26, 44]. For 4H-SiC, this cutoff frequency is $\omega_{\text{S}} \approx 942\,\text{cm}^{-1}$, which is $22\,\text{cm}^{-1}$ below the LO frequency.

Between the momentum of the incoming light, $k_i = \omega_i/c$, and the dispersion of the SPhP, a momentum[3] mismatch has to be overcome to successfully couple the incoming light to surface modes, see Fig. 2.5. This can be achieved by prism coupling [46, 47], with the use of a diffraction grating [42, 48, 49] or by tip-based cou-

[2] A derivation of the cut-off frequency can be found in, e.g., Refs. [26, 43, 44].

[3] Phonons actually are not considered to possess a momentum since along their propagation no mass is involved. Therefore the momentum value $p = \hbar k_{\text{phonon}}$ is referred to as 'crystal-momentum' or 'quasi-momentum' [45].

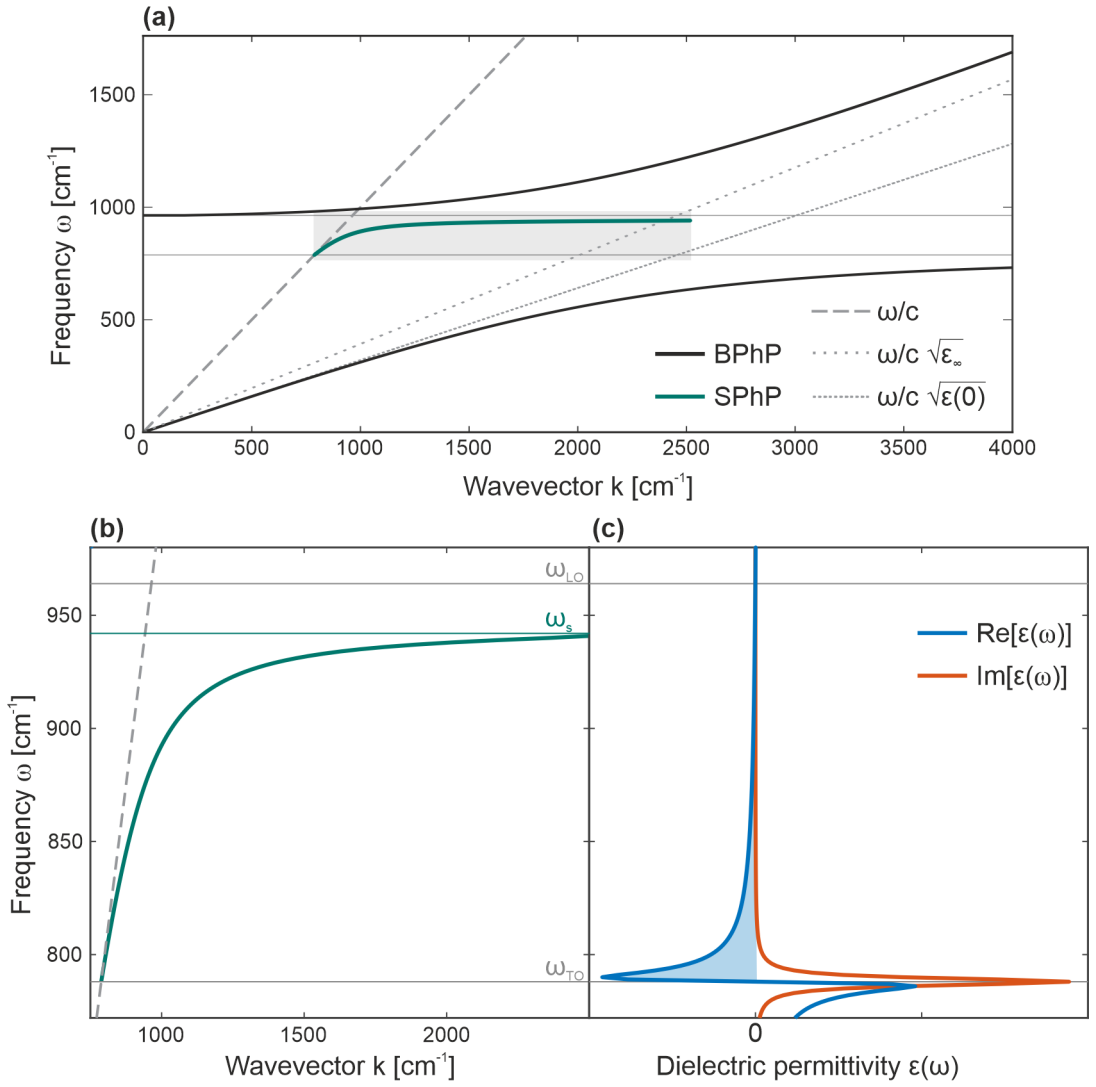

Figure 2.5. *Dispersion relation of BPhP and SPhP.* (a) The dispersion of BPhPs (black lines) and SPhPs (green line). The BPhPs exist outside of the Reststrahlen band, while the SPhP mode is only allowed inside, converging at the cutoff frequency ω_s. The dotted lines give the low and high frequency limits, and the gray dashed line illustrates the linear dispersion for a photon traveling in air (light line). (b) Zoom into Reststrahlen band, gray area of (a) with (c) corresponding plot of the dielectric function between TO and LO, where the real part (blue) is negative leading to the suppression of BPhPs.

pling [50, 51]. The three techniques are illustrated in Fig. 2.6.

Inside a prism (Fig. 2.6(a)), the incoming IR beam is refracted and travels through the prism at an angle θ with respect to the surface normal leading to total internal reflection. Its in-plane momentum changes accordingly from k_{IR} to $k_{\mathrm{IR,p}} = k_{\mathrm{IR}} n_{\mathrm{p}} \sin\theta$ inside the prism and the resulting evanescent wave can couple to the SPhP momentum if $k_{\mathrm{IR,p}} > k_0$ [46]. When using a grating on the sample, Fig. 2.6(b), an additional grating vector G can be added to the in-plane momentum of the IR beam $k_{\mathrm{IR,x}}$. The grating momentum is defined by $G_{\mathrm{m}} = m/p$ with p the grating period and m the diffraction order. The total in-plane momentum coupling to the SPhP momentum

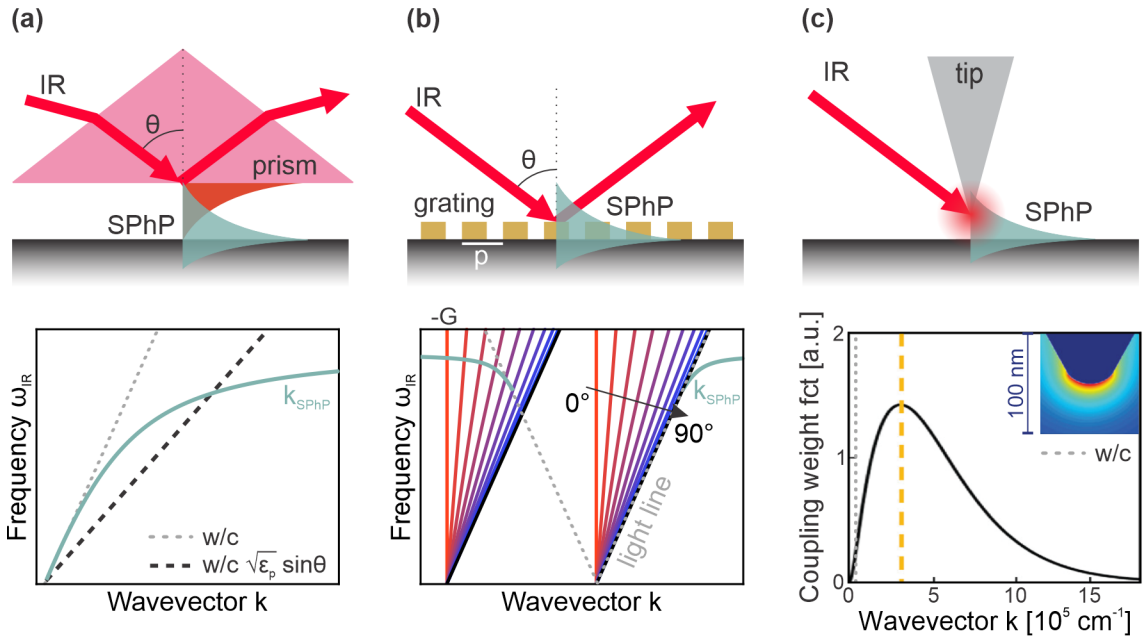

Figure 2.6. *Momentum matching via prism coupling, grating coupling and tip-based coupling.* (a) Prism coupling. Overlap with SPhP momentum is achieved by changing light momentum due to different refractive index of prism. Adapted from [43]. (b) Grating coupling. The grating adds a grating momentum to the light momentum to overcome the momentum mismatch between photon and SPhP. Adapted from [49]. (c) Tip-based coupling. The tip scatters the incoming wave into waves covering a wide range of in-plane momenta. Plot shows the momentum dependence of near-field coupling, adapted with permission from [52]. Copyright 2024 American Chemical Society. Gray dashed line shows light line for $\omega_{IR} = 1000\,\mathrm{cm}^{-1}$. Inset shows field enhancement at the tip apex, adapted with permission from [53]. Copyright 2024 American Chemical Society.

is then $k = k_{\mathrm{IR,x}} + G_{\mathrm{m}}$ [49]. In tip-based techniques, the tip itself can be used to overcome the momentum mismatch, which is illustrated in Fig. 2.6(c). Here, the IR beam is focused on the tip which scatters the light wave into waves covering a broad range of in-plane momenta. The plot shows the coupling weight as a function of the in-plane wavevector with a peak (yellow dashed line) at $k \approx 1/a$ with the tip radius a [52], the field enhancement at the tip apex is shown in the inset [53]. Thus, the tip-based technique enables coupling to a wide range of in-plane momenta, the photon momentum is illustrated by the gray dashed line. All these approaches lead to an evanescent in-plane momentum k_{x} larger than the original light momentum k_0 enabling the coupling to SPhP momenta k_{SPhP}.

2.3 Localized surface phonon polaritons

Surface phonon polaritons can appear, not only as propagating waves, but also as confined, localized modes in, e.g., nanostructures. The simplest structure here is a spherical resonator, similar to the appearance of localized plasmon polaritons in noble-metal nanospheres [54]. Mutschke et al. theoretically and experimentally discuss localized surface phonon polaritons in spherical SiC particles [55]. By extending

the particle range from spherical to ellipsoidal shapes, they also discuss the resonance frequency dependence on the resonator shape. By now, a common geometry for experiments on localized SPhPs are cylindrical resonators [56–58].

Previous studies dealt with the detailed analysis of localized modes in free-standing resonators and in the vicinity of a substrate, as well as in arrays of multiple resonators [44, 59]. It was shown that longitudinal and transverse dipole modes appear, whose frequencies shift for changing diameters and inter-resonator gaps. Spectra for different inter-resonator gaps G are shown in Fig. 2.7(a).

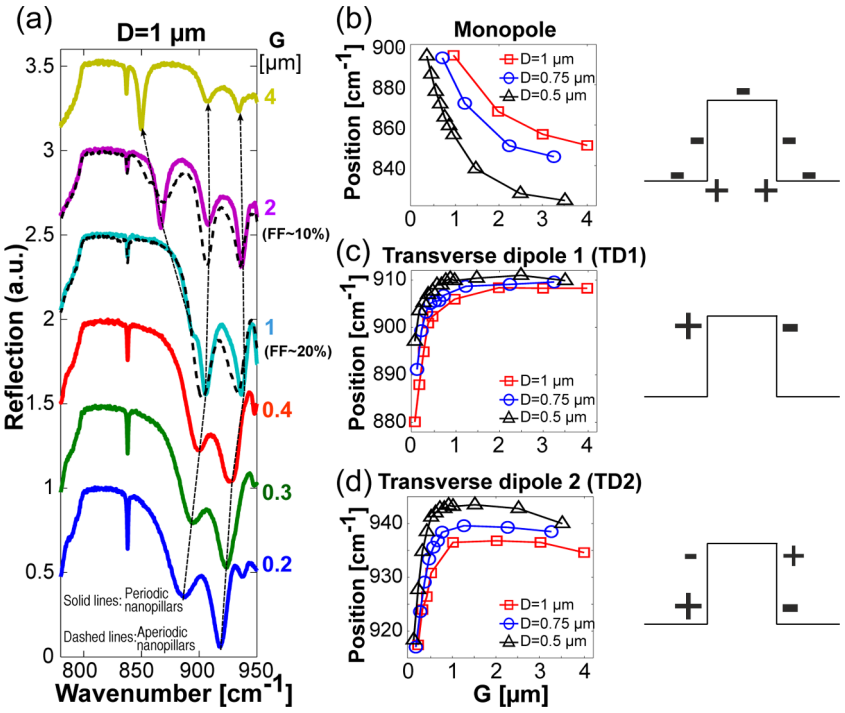

Figure 2.7. *Resonance frequencies in dependency of resonator parameters.* (a) Spectra showing shifts in resonances frequencies for different interresonator gap sizes. (b-d) Left: Resonance frequency dependence of individual monopolar and dipole modes on resonator diameter and interresonator gap. Right: Sketches of charge distributions of the three modes. Reprinted with permission from [59]. Copyright 2024 American Chemical Society.

The longitudinal dipole mode has its charge separation along the height of the resonator, while the transversal dipole modes confine charges separated along the resonator's diameter, as illustrated in Fig. 2.7(b-d,right). When placing the resonator on a substrate, the bottom charge of the longitudinal dipole mode is obscured by the substrate, such that only the top charge is observable. Because of this, it is usually referred to as a monopole mode [56]. The panels (b-d) in Fig. 2.7 show the modes' resonance frequency dependencies on the resonator diameter D, and the interresonator gap G. As can be seen by changing the resonator and array parameters, the monopolar resonance frequency shifts over a broad range of $> 60\,\mathrm{cm}^{-1}$. The dipolar modes (TD1 and TD2), instead, shift comparably little in frequency. This observation gives rise to the assumption that monopolar modes couple to their surrounding while dipolar modes are rather individual modes inside the resonators. The analysis

in Ref. [59] does not take into account the effect of coupling between localized resonator modes and propagating substrate modes, which will be discussed in the next section.

2.4 Hybridized phonon polaritons

Before moving on with the discussion of coupling between resonantors in a lattice, the underlying theory and the origin of strong coupling and avoided crossings will be introduced. This theory does not only explain the coupling between propagating modes and lattice resonances, but also, e.g., the coupling between photons and propagating polaritons leading to the Reststrahlen band. However, the discussion below will focus on the example of propagating polaritons and localized modes.

2.4.1 Strong coupling

In a system supporting not only propagating surface modes but also localized modes, these two modes can hybridize enabling strong coupling. Strong coupling between these modes opens the way for many applications such as molecule sensing [60, 61], directional thermal emission [62, 63], or topologically protected edge states [64].

The modes can be expressed as oscillators and their coupling can be described using a two-coupled oscillator model. In the quantum mechanical expression following a Hopfield model [27], the corresponding Hamiltonian reads

$$\mathcal{H} = \sum_q \hbar\omega_q^{\mathrm{m}} \hat{a}_q^\dagger \hat{a}_q + \hbar\omega_q^{\mathrm{s}} \hat{b}_q^\dagger \hat{b}_q + \hbar g_0 \left(\hat{a}_q^\dagger \hat{b}_q + \hat{a}_q \hat{b}_q^\dagger \right). \tag{2.4.1}$$

Here, ω_q^{s} and ω_q^{m} are the frequencies of the uncoupled SPhP and a localized mode at the in-plane wavevector q, g_0 denotes the coupling strength, also referred to as Rabi frequency, whereas $\hat{a}_q^\dagger$ ($\hat{a}_q$) and $\hat{b}_q^\dagger$ ($\hat{b}_q$) are the bosonic creation (annihilation) operators of the two modes.

When the two dispersions cross, the coupling leads to a Rabi splitting into two hybrid states. This anti-crossing occurs if the Rabi frequency is larger than the losses of both individual modes, a condition known as the strong coupling regime [57]. The coupled modes act as one system where energy is resonantly exchanged between both modes [65]. The anti-crossing of the two modes is depicted in Fig. 2.8. The eigenfrequencies of the upper and lower branch, respectively, can be calculated by diagonalizing the Hamiltonian in Eq. (2.4.1) using a Hopfield-Bogoliubov transformation leading to [57, 66]

$$\omega_q^{\pm} = \frac{\omega_q^{\mathrm{m}} + \omega_q^{\mathrm{s}} \pm \sqrt{\left(\omega_q^{\mathrm{m}} - \omega_q^{\mathrm{s}}\right)^2 + 4g_0^2}}{2}. \tag{2.4.2}$$

The entire system can also be modeled in a classical way by solving the equations of motion for two coupled oscillators leading to the same eigenfrequencies [67].

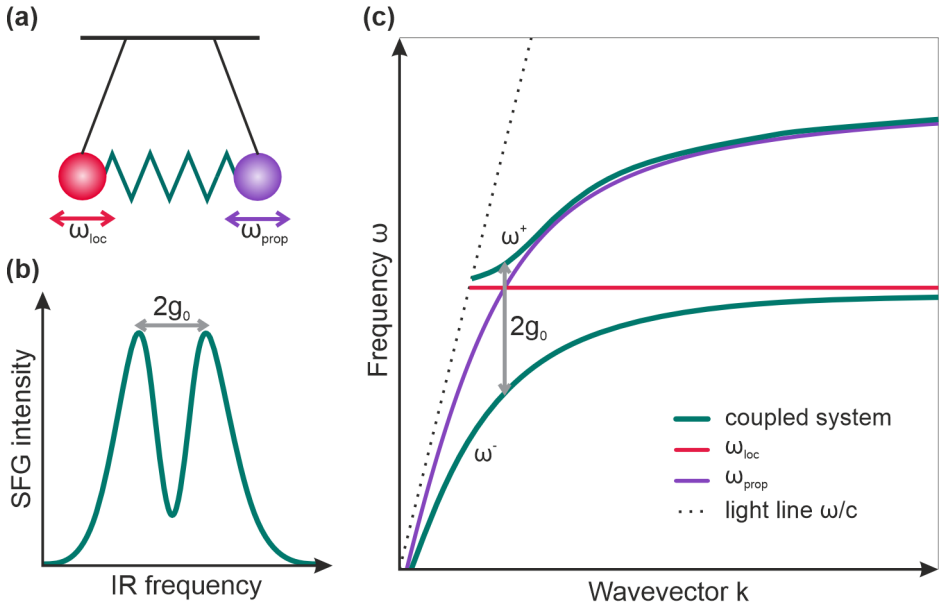

Figure 2.8. *Rabi splitting of a propagating and a localized surface phonon polariton in the strong coupling regime.* (a) Illustration of the coupled oscillating system. (b) Splitting of the resonance peak. (c) Dispersion plot illustrating avoided crossing. The individual mode frequencies (red and purple) couple, leading to an avoided crossing and splitting into two branches of new states (green lines) with Rabi frequency g_0.

The Rabi splitting is an unambiguous sign for strong coupling and the corresponding Rabi frequency g_0 equates to half of the difference between upper and lower polariton branch $2g_0 = \omega^+ - \omega^-$ [67, 68]. The magnitude of the Rabi frequency strongly depends on the overlap of the individual modes, and their respective oscillator strengths.

The concept of strong coupling is essential for the discussion of resonators on a substrate. After touching on a single resonator on a substrate in the previous section, a lattice of resonators is considered in the following, taking strong coupling into account.

2.4.2 Lattice resonances of SiC nanopillar arrays

After the analysis of the interplay of a single resonator with a substrate, the coupling between multiple resonators with a substrate will be discussed in the following, see the sketch of a lattice in Fig. 2.9.

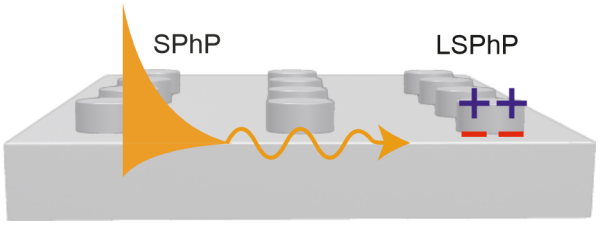

Figure 2.9. *Resonator lattice.* Illustration of resonator lattice with propagating surface polariton and localized resonance. Adapted from [P3].

Experiments and simulations on this topic have been performed in several previous works [44, 56, 59, 69]. This section focuses on the simulated findings by *Gubbin et al.* reported in Refs. [44, 57]. In Sec. 2.2, grating coupling has been introduced as a technique to overcome the momentum mismatch between incident light and propagating polariton. In their publications, the authors examined the dependence of the grating periodicity on the modal shifts, and the hybridization of monopole mode and SPhP.

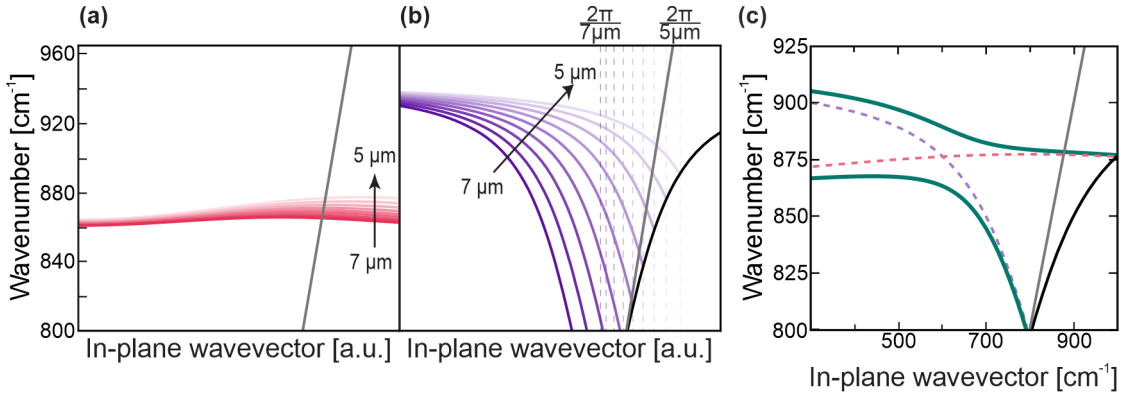

Figure 2.10. *Grating supported hybridization of monopole resonance and SPhP.* Grating periodicity dependent frequency shift of monopole mode (a) and backfolding of SPhP dispersion (b). The gray lines depict the light line and the dashed vertical lines mark the periodicity corresponding wavevectors. Black line gives the original SPhP dispersion. Both adapted with permission from [44]. Copyright 2024 by the American Physical Society. (c) Resulting hybridization (green) and avoided crossing between localized mode (red) and backfolded SPhP (purple). Adapted with permission from [57]. Copyright 2024 by the American Physical Society.

Simulations based on a tight-binding model [57] show clearly that the monopole resonance blueshifts with decreasing periodicity, see Fig. 2.10(a). This shift occurs due to dipolar coupling between the resonators, and is mainly important for the monopole mode. In contrast to the transverse dipole modes, for which the charge imbalance is located inside the resonator, the monopole mode induces a charge imbalance between the resonators and the sample substrate. In the solid-state picture of a crystal, the lattice vector given by the periodicity p, i.e., $G = \frac{2\pi}{p}$, marks the edge of the first Brillouin zone. Here, the dispersion of the propagating polariton folds back into the first Brillouin zone and thus creates wavevectors within range of the light line. The backfolding of the SPhP dispersion is illustrated in Fig. 2.10(b), where the black curve marks the original SPhP dispersion and the purple curves show SPhP disper-

sions backfolded with respect to the lattice vector. By this, the SPhP dispersion is folded into the light cone, thus momentum matching and polariton excitation is possible.

The backfolding of the SPhP dispersion also gives rise to a crossing point with the monopole resonance, as depicted in Fig. 2.10(c). Provided that the coupling strength g_0 is larger than the losses of the individual modes, the two modes cannot be treated individually anymore but hybridized. The green solid lines show the dispersion of the hybridized modes according to the strong coupling picture. With the change of the lattice constant, the resonance frequencies for the monopole mode and SPhP shift, see Fig. 2.10(a,b), however, the shift is much more prominent for the SPhP. Thus, with changing the lattice period, the resonances of hybridized polaritons can be tuned.

3

Theoretical Background: Sum Frequency Generation Microscopy

This chapter discusses the fundamentals of sum-frequency generation (SFG) microscopy. First, the concepts of optical microscopy are introduced in Sec. 3.1. The choice of SFG for high resolution imaging is motivated and compared to other imaging techniques. The chapter continues by discussing the theory of nonlinear optics with a closer look onto the nonlinear susceptibility and the theory of sum-frequency generation in Sec. 3.2. Finally, experimental setups for SFG microscopy are presented and compared, Sec. 3.3.

3.1 Optical microscopy beyond the diffraction limit

Generally, microscopy is the main tool for observation of objects with sizes below the diffraction limit of the human eye. The oldest known technique is light microscopy [70], which was invented at the end of the 16^{th} century. By today, a multitude of microscopy techniques, not only based on light but also, e.g., on electrons, neutrons or ions, using several physical principles exist [71–73]. To provide a basic understanding of the microscopy technique discussed in this thesis, the next paragraphs provide fundamental information on light microscopy, and tools for high-resolution imaging.

3.1.1 Brief introduction to light microscopy

The classical light microscope consists of two lenses, referred to as objective and ocular lens, while the observer's eyes serve as detectors. In scientific experiments, however, the detector is commonly a camera and the ocular lens is replaced by a tube lens. The objective usually is a lens system itself, using a set of different lenses to provide the best image. The magnification is dependent on both objective and tube lens, while the possible resolution is only dependent on the objective's characteristics and the light source, as will be discussed in Sec. 3.1.2.
Here, the general working principle of a light microscope as well as the terms magnification and numerical aperture (NA) shall be introduced briefly, following the descriptions in Refs. [74, 75]. When light is travelling from an object to an objective, the objective creates a real image of the object which will be projected onto the

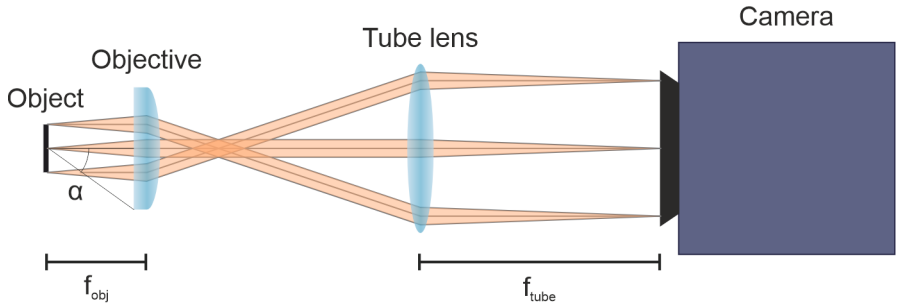

Figure 3.1. *Illustration of beam path magnification.*

camera by the tube lens. To create a sharp image, the object has to be positioned in the focal plane of the objective. The distance between focal plane and objective is referred to as the working distance d_{w}, and is a characteristic of the objective. A distinction is made between 'regular' objectives and 'long working distance' objectives, the latter being constructed in a way enabling the object to be at a larger distance from the objective but still providing large magnification. The microscope's magnification is given by

$$M_{\mathrm{mic}} = \frac{f_{\mathrm{tube}}}{f_{\mathrm{obj}}}, \tag{3.1.1}$$

with the two focal lengths f_{obj} and f_{tube} of the objective and the tube lens, respectively. An example beam path is illustrated in Fig. 3.1, where the objective is depicted as a single lens for simplicity.

As will be discussed in Sec. 3.1.2, the resolution is dependent on the imaging wavelength and the objective's numerical aperture (NA). The NA is defined by the opening angle α, see Fig. 3.1, and the refractive index n of the medium between the object and objective

$$\mathrm{NA} = n \sin \alpha. \tag{3.1.2}$$

The opening angle α describes the size of the light cone that can be detected by the objective, thus light rays with a larger angle than the opening angle do not enter the objective.

3.1.2 Super-resolution microscopy

Super resolution is achieved when a microscope is able to resolve two objects in an image that are much closer than the wavelength of the imaging light. Such microscopes circumvent the diffraction limit of light, which will be introduced in the following.

The diffraction limit

Throughout the years, several definitions for the diffraction limit have been introduced, of which this introduction will discuss the three most popular ones.

Abbe Limit In 1873, Abbe defined the diffraction limit by the experimental ability to distinguish two neighboring lines in a grating [76]. Light shining through such a lattice is diffracted, and the denser the lines in the lattice, the stronger the diffraction of the light is. The Abbe limit is given by

$$R_{\text{Abbe}} = \frac{\lambda}{2 \cdot NA}, \tag{3.1.3}$$

depending on the imaging wavelength λ and the objective's numerical aperture. This equation is based on the fact that the NA of the objective needs to be of a specific minimum size such that not only the zero-order but also at least the first-order diffraction maximum can be collected by the objective, leading to $R = \lambda/NA$. This holds for illumination under normal incidence. If the light is illuminating the sample under an angle that is comparable to the opening angle of the objective, the before mentioned correlation can be divided by two, leading to the Abbe Limit in Eq. (3.1.3).

Rayleigh Limit The Rayleigh limit is based on the observation of illuminated dots generating so-called Airy disks [77] and concentric rings around them, which appear due to diffraction on a circular aperture, here the microscope's objective. As for Abbe, it was experimentally detected how far apart two objects, in this case dots, need to be to distinguish them. The diffraction limit by Rayleigh is satisfied when the second dot is exactly in the first diffraction order of the first dot, leading to [78]

$$R_{\text{Rayleigh}} = \frac{0.61 \cdot \lambda}{NA}. \tag{3.1.4}$$

FWHM The third common criterion is based on the 'full width half maxium' (FWHM) of the intensity profile of an airy disk that appears when imaging a point-like object. It can be calculated as

$$R_{\text{FWHM}} = \frac{0.51 \cdot \lambda}{NA}. \tag{3.1.5}$$

The resulting FWHM can be seen as a lower limit for the resolution of the microscope. [79].

The criteria for the diffraction limit are based on different experiments leading to different values for the diffraction limit. Within this thesis, the Abbe diffraction limit, Eq. (3.1.3), will be used to discuss the resolution of optical microscopes [80].

Microscopy techniques for super-resolution imaging

As can be directly seen in the above criteria, achievable resolution strongly depends on the choice of imaging wavelength. Therefore, a straightforward approach for high spatial resolution imaging is the use of a short imaging wavelength, i.e., ultraviolet (UV) light. The short wavelength leads to possible resolutions of $\approx 100\,\text{nm}$, without the necessity of overcoming the diffraction limit [81, 82]. The main disadvantage of this technique is the lack of resonances in the UV regime for many samples, and thus no contrast in the images.
In contrast, resonant imaging with resolution beyond the diffraction limit of the imaging light can be achieved by various techniques based on fluorescence, such as stimulated emission depletion (STED) microscopy [83, 84], structured illumination microscopy (SIM) [85, 86], and stochastic optical reconstruction microscopy (STORM) [87, 88] to name only a few. These techniques are mainly used in cell biology and steady research in this field leads to a growing understanding in biology, e.g., cell functioning [89]. However, since they rely on fluorescence, these approaches are limited to naturally-fluorescent or functionalized samples. Additionally, fluorescence imaging is widely applicable only in the visible range [21].
In addition, nanotip-based approaches such as scattering-type scanning nearfield optical microscopy (s-SNOM) [90, 91] and photothermal-induced resonance (PTIR) microscopy [92, 93] have attracted wide attention. These methods provide deeply sub-wavelength imaging that no longer relies on fluorescence, but often suffer from the nanotip influencing the measurement [20].
An alternative approach to these established techniques is nonlinear-optical frequency mixing, such as sum-frequency generation (SFG) [22]. Here, the light at the resonant imaging wavelength is upconverted with a second, nonresonant light source at much shorter wavelength, providing resonant contrast given by the former, and high spatial resolution defined by the latter. Although the technique of frequency mixing has been used frequently in microscopy, the aspect of using it for gaining highly-resolved images beyond the diffraction limit of the imaging light has not been widely explored. In addition to a high spatial resolution, nonlinear-optical frequency mixing can be applied to both in vivo and in vitro applications. It provides label-free, far-field access, and a better signal-to-noise ratio by, e.g., not requiring fluorescence and thus resulting in less background [94–96].
Frequency-mixing relies on nonlinear optical effects, which will be explained in the following section, with emphasis on the description of the process of sum-frequency generation.

3.2 Introduction to nonlinear optics

As long as not stated otherwise, this section is based on the two textbooks *The Principles of Nonlinear Optics* by Yuen-Ron Shen [97] and *Nonlinear Optics* by Robert W. Boyd [98].

Every nonlinear optical process can be discussed as the combination of two (independent) processes [97]: The first process is the induction of a nonlinear response in a medium by incoming light, which can be described by the constitutive equation

$$\begin{aligned}\mathbf{P}(\mathbf{r},t) =& \overbrace{\varepsilon_0\Big[\chi^{(1)}\mathbf{E}(\mathbf{r},t)}^{\substack{linear\\ \text{optical effect}}} \overbrace{+\chi^{(2)}\mathbf{E}^2(\mathbf{r},t)+\chi^{(3)}\mathbf{E}^3(\mathbf{r},t)+...\Big]}^{\text{higher-order nonlinear optical effects}} \\ \equiv& \mathbf{P}^{(1)}(\mathbf{r},t)+\mathbf{P}^{(2)}(\mathbf{r},t)+\mathbf{P}^{(3)}(\mathbf{r},t)+...,\end{aligned} \tag{3.2.1}$$

expressing the induced polarization $\mathbf{P}$ in terms of the driving electric field $\mathbf{E}$, the free-space permittivity ε_0, the linear susceptibility $\chi^{(1)}$, and the nonlinear susceptibilities $\chi^{(2)}$ and $\chi^{(3)}$ of second- and third-order, respectively. To describe a linear optical effect, the first term of the equation above is sufficient, though the response of a medium is nonlinear in general and can only be regarded as linear for sufficiently weak fields [99]. The power series expansion holds true for strong fields, with the n^{th}-order nonlinear optical effect being proportional to the n^{th}-order nonlinear susceptibility, accordingly. For extremely strong fields, the perturbative description, Eq. (3.2.1), fails and a non-perturbative strong-field description is required [99].

The second process is the generation of new components of the electromagnetic field, which can be described by Maxwell's equations. These equations describe all electromagnetic processes by their electric and magnetic fields $\mathbf{E}(\mathbf{r},t)$ and $\mathbf{B}(\mathbf{r},t)$. They read

$$\nabla\times\mathbf{E} = -\frac{\partial\mathbf{B}}{\partial t} \tag{3.2.2a}$$

$$\nabla\times\mathbf{B} = \mu_0\left(\mathbf{J}+\varepsilon_0\frac{\partial\mathbf{E}}{\partial t}\right) \tag{3.2.2b}$$

$$\nabla\cdot\mathbf{E} = \frac{\rho}{\varepsilon_0} \tag{3.2.2c}$$

$$\nabla\cdot\mathbf{B} = 0, \tag{3.2.2d}$$

with the current density $\mathbf{J}(\mathbf{r},t)$ and the charge density $\rho(\mathbf{r},t)$. Their relation is described by the charge conservation law

$$\nabla\cdot\mathbf{J}+\frac{\partial\rho}{\partial t} = 0. \tag{3.2.3}$$

Oftentimes, the Maxwell's equations are given with the electric polarization $\mathbf{P}$ instead of the current and charge densities using Eq. (3.2.3) and

$$\mathbf{J} = \mathbf{J}_{\mathrm{dc}} + \frac{\partial \mathbf{P}}{\partial t}, \tag{3.2.4}$$

where $\mathbf{J}_{\mathrm{dc}}$ is the dc current density. Implementing both formulas into the Maxwell's equations, Eqs. (3.2.2b) and (3.2.2c) then change to

$$\nabla \times \mathbf{B} = \mu_0 \varepsilon_0 \frac{\partial}{\partial t} \left(\mathbf{E} + \frac{\mathbf{P}}{\varepsilon_0} \right) + \mu_0 \mathbf{J}_{\mathrm{dc}} \tag{3.2.5a}$$

$$\nabla \cdot \left(\mathbf{E} + \frac{\mathbf{P}}{\varepsilon_0} \right) = 0. \tag{3.2.5b}$$

As already stated in Eq. (3.2.1), the polarization can be described by a power expansion of the electric field. If $\mathbf{E}(\mathbf{r}, t)$ can be expressed by monochromatic waves, according to $\mathbf{E}(\mathbf{r}, t) = \sum_i E_0 e^{i(\mathbf{k}_i \cdot \mathbf{r} - \omega t)}$ the polarization can be described as a function of a wavevector $\mathbf{k}$, and frequency ω by

$$\mathbf{P}(\mathbf{k}, \omega) = \mathbf{P}^{(1)}(\mathbf{k}, \omega) + \mathbf{P}^{(2)}(\mathbf{k}, \omega) + \mathbf{P}^{(3)}(\mathbf{k}, \omega) + ... \tag{3.2.6}$$

where $\chi^{(n)}(\mathbf{r}, t)$ (compare Eq. (3.2.1)) turns into $\chi^{(n)}(\mathbf{k}, \omega)$ according to

$$\begin{aligned} \chi^{(n)}(\mathbf{k}, \omega) = \int_{\mathbb{R}} & \chi^{(n)}(\mathbf{r} - \mathbf{r}_1, t - t_1; ...; \mathbf{r} - \mathbf{r}_n, t - t_n) \\ & \times e^{-i[\mathbf{k}_i(\mathbf{r} - \mathbf{r}_1) - \omega_1(t - t_1) + ... + \mathbf{k}_n(\mathbf{r} - \mathbf{r}_n) - \omega_n(t - t_n)]} d\mathbf{r}_1 dt_1 ... d\mathbf{r}_n dt_n. \end{aligned} \tag{3.2.7}$$

In the electric dipole approximation, $\chi^{(n)}$ is independent of $\mathbf{r}$ and $\mathbf{k}$, leading to $\chi^{(n)}(t)$ and $\chi^{(n)}(\omega)$, respectively.
The nonlinear optical susceptibilities are characteristics of the material, and allow the description of all nonlinear optical effects using Maxwell's equations in Eqs. (3.2.2) and (3.2.5) [99].
In general, the lowest-order nonlinear susceptibility is the second-order susceptibility $\chi^{(2)}$. However, $\chi^{(2)}$ is only non-zero in materials with non-centrosymmetric crystal structure. For centrosymmetric crystals, the lowest nonlinear process is a third-order process described by $\chi^{(3)}$ and the second-order susceptibility vanishes. This notion will be revisited in one of the following paragraphs regarding inversion symmetry.

3.2.1 The second-order nonlinear susceptibility $\chi^{(2)}$

Within this thesis, only the second-order nonlinear susceptibility $\chi^{(2)}$ is relevant. Complete evaluation of $\chi^{(n)}$ can only be done with a quantum-mechanical cal-

culation. For more insight into the origin and features of $\chi^{(n)}$, simple models can be applied, such as the anharmonic oscillator model, as was done in, e.g., Refs. [97, 100, 101]. In this section, emphasis is put on important properties of $\chi^{(2)}$.

Due to the vectorial nature of the electric field, the second-order nonlinear susceptibility is a tensor:

$$\mathbf{P}_i^{(2)}\left(\omega_3 = \omega_1 + \omega_2\right) = \varepsilon_0 \sum_{jk} \chi_{ijk}^{(2)}\left(\omega_1, \omega_2\right) \mathbf{E}_j\left(\omega_1\right) \mathbf{E}_k\left(\omega_2\right) \tag{3.2.8}$$

with the indices i, j, k indicating the cartesian coordinates x, y, z. The symmetry of this tensor gives the selection rules for nonlinear processes, which will be discussed in the following.

Permutation symmetry

As shown in Ref. [98], the permutation of electric fields does not have an influence on the susceptibility tensor:

$$\chi_{ijk}^{(2)}\left(\omega_3, \omega_1, \omega_2\right) = \chi_{ikj}^{(2)}\left(\omega_3, \omega_2, \omega_1\right) \tag{3.2.9}$$

as long as the two frequencies ω_1 and ω_2 are interchanged accordingly. The order of the two fields $E_1\left(\omega_1\right)$ and $E_2\left(\omega_2\right)$ does not matter in any physical way. This characteristic is known as intrinsic permutation symmetry.

Structural symmetry

As stated above, the nonlinear susceptibility is a property of the respective medium and therefore should have a symmetry which expresses the medium's structural symmetry. If a medium remains unchanged when applying a certain symmetry operation S, the corresponding $\chi^{(2)}$ tensor should also stay invariant under this operation. The invariance of $\chi^{(2)}$ under a specific symmetry operation can then be described by

$$\left(\hat{i} \cdot S^{\dagger}\right) \cdot \chi^{(2)} : \left(S \cdot \hat{j}\right)\left(S \cdot \hat{k}\right) = \chi_{ijk}^{(2)}. \tag{3.2.10}$$

For each symmetry operation of the medium's symmetry class, such an equation exists. Due to relations between the different tensor elements of $\chi^{(2)}$, not all of these elements are independent, leading to only a few independent and non-vanishing

elements of $\chi^{(2)}$. A table summarizing the nonvanishing $\chi^{(2)}$-elements for crystals of different symmetry classes can be found in, e.g., Ref. [97].

Influence of Inversion symmetry

Second-order nonlinear processes scale with $\chi^{(2)}$, Eq. (3.2.1), and are mostly referred to as interface-specific techniques. This statement relies on the fact that $\chi^{(2)}$ vanishes for inversion-symmetric materials. Hence, no second-order nonlinear signal can be measured from the bulk of materials which are inversion symmetric, but only from their surfaces and interfaces. Out of the 32 crystal classes this is true for 11 [98]. For materials with broken inversion symmetry, a nonlinear signal can be obtained not only from the surfaces, but also from the bulk. In the following, a short proof for the vanishing of $\chi^{(2)}$ in inversion-symmetric materials shall be given.

As already stated in Eq. (3.2.1), the polarization of a second-order nonlinear process can be given as

$$P(t) = \varepsilon_0 \chi^{(2)} E^2(t) \tag{3.2.11}$$

with an electric field $E(t)$ applied.

For inversion-symmetric materials, the sign of the polarization must change if the sign of the applied electric field is changed. After this operation, Eq. (3.2.11) reads

$$\begin{aligned} -P(t) &= \varepsilon_0 \chi^{(2)} \left[-E(t)\right]^2 \\ &= \varepsilon_0 \chi^{(2)} E^2(t) \end{aligned} \tag{3.2.12}$$

Comparing this relation with Eq. (3.2.11) leads to the condition of $P(t) = -P(t)$, which can only be fulfilled if the polarization is vanishing. Hence, $\chi^{(2)}$ must be vanishing, too. Therefore

$$\chi^{(2)} = 0, \tag{3.2.13}$$

resulting in no signal generation for second-order nonlinear optical effects in materials with inversion symmetry.

3.2.2 Sum-frequency generation

A specific case of second-order nonlinear effects is sum-frequency generation (SFG), with $\chi^{(2)}(\omega_3 = \omega_1 + \omega_2, \omega_1, \omega_2)$, illustrated in Fig. 3.2(a). SFG was first observed experimentally by *Bass et al.* in 1962 using two ruby lasers overlapped on a triglycine

sulfate crystal [102]. Second-harmonic generation (SHG), i.e., mixing of two similar frequencies, had already been observed before, and it was assumed that nonlinear terms should also be sufficient to mix light of different frequencies. In general, SHG can be seen as a special case of SFG, where $\omega_1 = \omega_2$. SFG spectroscopy has been proven highly useful in studying, e.g., molecular systems, such as water interfaces [103, 104] or carbon monoxide [105], but also crystals [106].

To analytically describe the process of frequency-mixing, two optical fields $\mathbf{E}_1$ and $\mathbf{E}_2$ from two incoming lasers with frequencies ω_1 and ω_2 are considered. The mixed optical field is expressed by

$$\mathbf{E}(t) = E_1 e^{-i\omega_1 t} + E_2 e^{-i\omega_2 t} + c.c. \tag{3.2.14}$$

Following from Eq. (3.2.11), the second-order polarization $\mathbf{P}^{(2)}(t)$ reads

$$\begin{aligned}\mathbf{P}^{(2)}(t) = \varepsilon_0 \chi^{(2)} \Big[& E_1^2 e^{-2i\omega_1 t} + E_2^2 e^{-2i\omega_2 t} + 2E_1 E_2 e^{-i(\omega_1+\omega_2)t} \\ & + 2E_1 E_2^* e^{-i(\omega_1-\omega_2)t} + c.c. \Big] + 2\varepsilon_0 \chi^{(2)} \Big[E_1 E_1^* + E_2 E_2^* \Big].\end{aligned} \tag{3.2.15}$$

Eq. (3.2.15) shows that new frequency components of the polarization have appeared. Thus, new electromagnetic waves are generated at frequencies $\omega_1 + \omega_2$, $\omega_1 - \omega_2$, $2\omega_1$ and $2\omega_2$, namely sum-frequency generation (SFG), difference-frequency generation (DFG), and second-harmonic generation (SHG), respectively, as well as the appearance of optical rectification (OR) for $\omega = 0$. Using the notation $\tilde{\mathbf{P}}^{(2)}(t) = \sum_n \mathbf{P}(\omega_n) e^{-i\omega_n t}$, Eq. (3.2.15) can be split into the respective contributions for the different second-order nonlinear effects:

$$\begin{aligned}\mathbf{P}(2\omega_1) &= \varepsilon_0 \chi^{(2)} \mathbf{E}_1^2 \quad \text{(SHG)}, \\ \mathbf{P}(2\omega_2) &= \varepsilon_0 \chi^{(2)} \mathbf{E}_2^2 \quad \text{(SHG)}, \\ \mathbf{P}(\omega_1 + \omega_2) &= 2\varepsilon_0 \chi^{(2)} \mathbf{E}_1 \mathbf{E}_2 \quad \text{(SFG)}, \\ \mathbf{P}(\omega_1 - \omega_2) &= 2\varepsilon_0 \chi^{(2)} \mathbf{E}_1 \mathbf{E}_2^* \quad \text{(DFG)}, \\ \mathbf{P}(0) &= 2\varepsilon_0 \chi^{(2)} (E_1 E_1^* + E_2 E_2^*) \quad \text{(OR)}.\end{aligned} \tag{3.2.16}$$

In this thesis, only the effect of sum-frequency generation with $\omega_3 = \omega_1 + \omega_2$, Fig. 3.2(a), will be considered, according to

$$\mathbf{P}(\omega_1 + \omega_2) = 2\varepsilon_0 \chi^{(2)} \mathbf{E}_1 \mathbf{E}_2. \tag{3.2.17}$$

To obtain maximum efficiency in sum-frequency generation, phase matching between the IR and VIS laser pulses has to be provided. Phase-matching grants identical

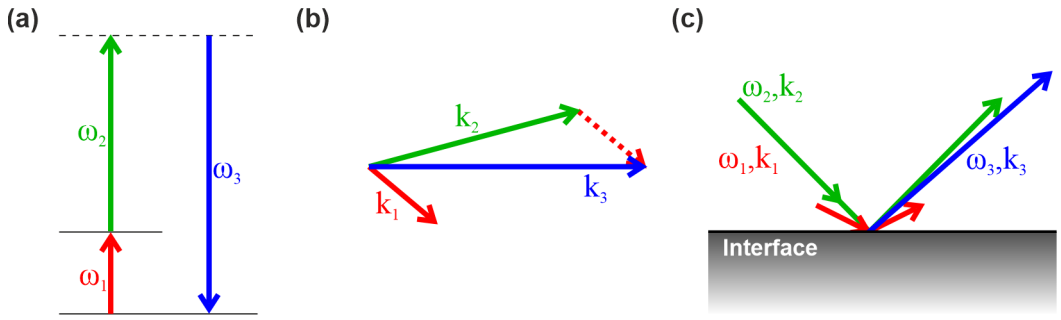

Figure 3.2. *Sum-frequency generation process.* (a) Energy-level diagram describing the SFG frequency mixing. (b) Vector addition of wavevectors. (c) SFG process under oblique incidence of an interface with $\omega_1 = \omega_{\mathrm{IR}}$, $\omega_2 = \omega_{\mathrm{VIS}}$ and $\omega_3 = \omega_{\mathrm{SFG}}$.

phase velocities of the SFG wave and the mixing field to constructively interfere while propagating through the nonlinear crystal. The phase matching condition to be fulfilled reads

$$\Delta\mathbf{k} = \mathbf{k}_1 + \mathbf{k}_2 - \mathbf{k}_3 = 0 \tag{3.2.18}$$

and is illustrated in Fig. 3.2(b). Here, $\mathbf{k}_{1,2}$ are the wavevectors of the incoming beams, and $\mathbf{k}_3$ is the wavevector of the resulting beam. Eq. (3.2.18) implies that the generated wave extracts the energy from the incident waves in the most efficient way, maintaining a fixed phase relation according to the nonlinear polarization. If no phase matching is achieved, the SFG wave's intensity is reduced, accordingly.

Figuratively, phase matching means that the individual atomic dipoles of the generated wave are properly in phase, emitting fields that add up coherently. The total radiated power then scales quadratically with the number of dipoles.

The wavevectors $\mathbf{k}_{1,2}$ follow the relation $k_i \equiv \omega_i n_i/c$, with the refractive index of the medium n_i for light with frequency ω_i. For phase matching, $\mathbf{k}_3$ has to fulfill $k_3 \equiv \omega_3 n_3/c$ [107]. Experimentally, however, $\mathbf{k}_3$ is oftentimes not exactly equal to $\omega_3 n_3/c$, leading to $\Delta k \neq 0$.

Apart from nonlinear-optical light generation in a nonlinear crystal with phase matching, SFG spectroscopy is often employed, with much lower SFG yield, to study surfaces and interfaces in a geometry as shown in Fig. 3.2(c) [108]. In this geometry, phase-matching as discussed above cannot be obtained. However, the geometry is beneficial for different reasons: oblique incidence of the excitation laser leads to accessibility of several $\chi^{(2)}$-components, and the non-colinearity of the beams results in geometric separability of the resulting SFG beam.

Considering sum-frequency generation using a visible and a mid-IR beam, the propagation direction of the generated sum-frequency beam is dominated by the propagation direction of the visible beam, due to momentum conservation.

$$\mathbf{k}_{\mathrm{SFG}} = \mathbf{k}_{\mathrm{IR}} + \mathbf{k}_{\mathrm{VIS}} \overset{\mathbf{k}_{\mathrm{VIS}} \gg \mathbf{k}_{\mathrm{IR}}}{\approx} \mathbf{k}_{\mathrm{VIS}} \tag{3.2.19}$$

The amplitude A of the generated SF wave can be expressed as [98]

$$A_3(L) = \frac{i\chi^{(2)}\omega_3^2 A_1 A_2}{k_3 c^2}\left(\frac{e^{i\Delta k L}-1}{i\Delta k}\right), \tag{3.2.20}$$

dependent on the path length in the nonlinear medium L, with the second-order nonlinear susceptibility $\chi^{(2)}$, the SFG frequency ω_3, the incident field amplitudes A_i, and the generated wavevector k_3.

To estimate the intensity of the generated wave, the magnitude of the Poynting vector averaged over time needs to be considered. Using Eq. (3.2.20), the intensity is given by [98]

$$I_3 = 2n_i\varepsilon_0 c|A_3|^2 = \frac{2\chi^{(2)2}\omega_3^2 I_1 I_2}{n_1 n_2 n_3 \varepsilon_0 c^2} L^2 \operatorname{sinc}^2\left(\frac{\Delta k L}{2}\right). \tag{3.2.21}$$

The term $\operatorname{sinc}^2(\Delta k L/2)$ is known as the phase mismatch factor. Fig. 3.3 illustrates the phase mismatch factor (a), as well as the intensity I_3 as a function of L for the cases of phase matching, quasi phase matching and no phase matching (b).

Now, the effective intensity of the sum-frequency generated beam can be given as a measure of the maximum intensity possible dependent on the phase mismatch Δk and the path length of the nonlinear medium:

$$I_3 = I_3^{\max} \operatorname{sinc}^2\left(\frac{\Delta k L}{2}\right). \tag{3.2.22}$$

In this equation, it is directly obvious that not fulfilling the phase matching condition completely leads to a strong decrease in SFG intensity, see Fig. 3.3(a). The oscillations in the graph are caused by a power back-flow from the generated wave back to the original waves, which can happen if the SFG wave becomes out of phase with polarization if $L > 1/\Delta k$ [98].

The phase matching condition was first experimentally observed by *Maker et al.* in 1962 [109], where they focused the laser beam of a ruby laser onto a quartz crystal, and measured the change in the SFG intensity while rotating the crystal, i.e., changing the path length L and the accessibility of different symmetry elements within $\chi^{(2)}$.

The resulting SFG intensity can be calculated via the polarization of the SFG field

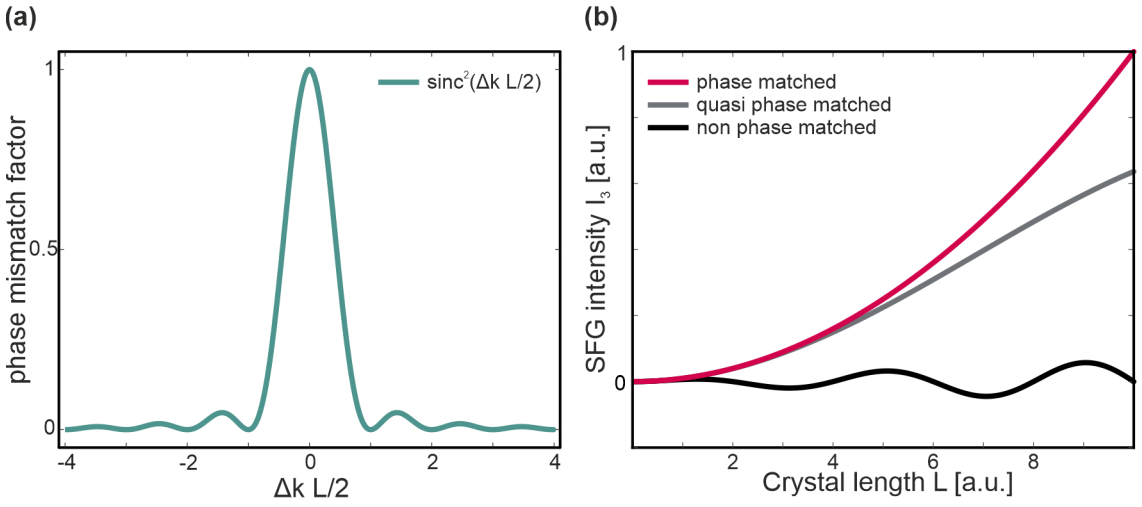

Figure 3.3. *Influence of wavevector mismatch on SFG intensity.* (a) For perfect phase matching, the intensity of the generated wave is maximal and decreases dramatically for phase mismatch, adapted from [107]. (b) SFG intensity plots for phase matching (red), quasi phase matching (gray) and no phase matching (black).

with

$$I^{\mathrm{SFG}} \propto \left|P_{\mathrm{x}}^{\mathrm{SFG}} + P_{\mathrm{y}}^{\mathrm{SFG}} + P_{\mathrm{z}}^{\mathrm{SFG}}\right|^2 / \Delta k^2, \tag{3.2.23}$$

where x, y and z denote the three dimensions in space. From Eq. (3.2.8), the relation between polarization and optical fields is already known. For complete description of the fields, the local field corrections $L_{1,2}$ need to be taken into account. The so-called Fresnel coefficients L (R) describe to what extent the light of the incoming beams is transmitted into (reflected by) the material depending on the beam frequency. A full list and derivation of the coefficients can be found in, e.g., Ref. [100]. The polarization is then described by the second-order nonlinear susceptibility $\chi^{(2)}$, the Fresnel coefficients $L_{1,2}$ and the electric fields $E_{1,2}$ according to

$$\mathbf{P}_{\mathrm{xyz}}^{\mathrm{SFG}} \propto \chi_{\mathrm{xyz}}^{(2)} \left(L_1 \mathbf{E}_1\right) \left(L_2 \mathbf{E}_2\right), \tag{3.2.24}$$

leading to the full description of the resulting SFG intensity

$$I^{\mathrm{SFG}} \propto \sum_{xyz} \left(L_{\mathrm{SFG}} \mathbf{P}_{xyz}^{\mathrm{SFG}}\right) / \Delta k^2. \tag{3.2.25}$$

Here, L_{SFG} describes the outgoing Fresnel coefficient for the generated light. In the experiments described in this thesis, only the exciting IR laser beam changes its frequency. Therefore, the frequency of the second upconverting laser beam is fixed

and the Fresnel coefficient L_2 is constant, accordingly. In the following calculations, this constant is set to $L_2 = 1$ for simplicity. Using the Eqs. (3.2.23) and (3.2.24), the resulting SFG intensity spectrum of an experiment can be estimated with three main contributors, i.e., the nonlinear susceptibility $\chi^{(2)}$, the Fresnel coefficient of the exciting laser L_1, and the phase matching condition Δk.

An example for an SFG measurement on 4H-SiC is shown in Fig. 3.4(a). The gray dots show data measured with the SFG microscope discussed throughout this thesis. In this measurement, the exciting laser is an IR laser with $E_1 = E_{\mathrm{IR}}$ and the upconversion laser is a visible laser with $E_2 = E_{\mathrm{VIS}}$. Taking the polarizations of the laser beams and the non-vanishing elements of $\chi^{(2)}$ into account, the formula for calculating the SFG intensity in this example reduces to

$$I_{\mathrm{PP}}^{\mathrm{SFG}} \propto |\chi_{\mathrm{xxz}}^{(2)} E_{\mathrm{x,VIS}} L_{\mathrm{zz}} E_{\mathrm{z,IR}}|^2 / \Delta k^2 \tag{3.2.26}$$

and is plotted a as green line on top of the data points in Fig. 3.4(a).

The plot shows nicely, that Eq. (3.2.26) fits to the measured data well enough to estimate the important features of the spectrum. Values for both the experimental data and the fit are normalized, the actual magnitudes differ and for a reasonable intensity comparison several other parameters like detector efficiency and transmittance of optics have to be taken into account. Fig. 3.4(b-d) break the formula down into their individual contributors: the nonlinear contribution of the second-order susceptibility (b) and the linear contributions of the Fresnel coefficient (c) and the phase matching coefficient (d).

The only non-vanishing element of the $\chi^{(2)}$-tensor contributing to the signal, $\chi_{\mathrm{xxz}}^{(2)}$, can be calculated by [110]

$$\chi_{\mathrm{xxz}}^{(2)} = \chi_{\mathrm{NR,xxz}}^{(2)} + \sum_q \frac{A_{q,\mathrm{xxz}}^{(2)}}{\omega_{\mathrm{IR}} - \omega_q + i\Gamma_q}. \tag{3.2.27}$$

Here, $\chi_{\mathrm{NR,xxz}}^{(2)}$ is the non-resonant contribution of the susceptibility, $A_{q,\mathrm{xxz}}$ is the resonance amplitude, ω_{IR} is the respective IR frequency, w_q are the resonant frequencies and Γ_q expresses the damping.
In the case shown, only the Fresnel coefficient L_{zz} contributes to the SFG intensity. Its expression reads

$$L_{\mathrm{zz}} = \frac{\varepsilon_\perp}{\varepsilon_\parallel} \frac{2k_{\mathrm{z}}^{\mathrm{i}}}{\varepsilon_\perp k_{\mathrm{z}}^{\mathrm{i}} + \varepsilon_{\mathrm{air}} k_{\mathrm{z}}^{\mathrm{t,e}}} \tag{3.2.28}$$

with the perpendicular (parallel) contribution of the dielectric function $\varepsilon_{\perp(\parallel)}$ and the

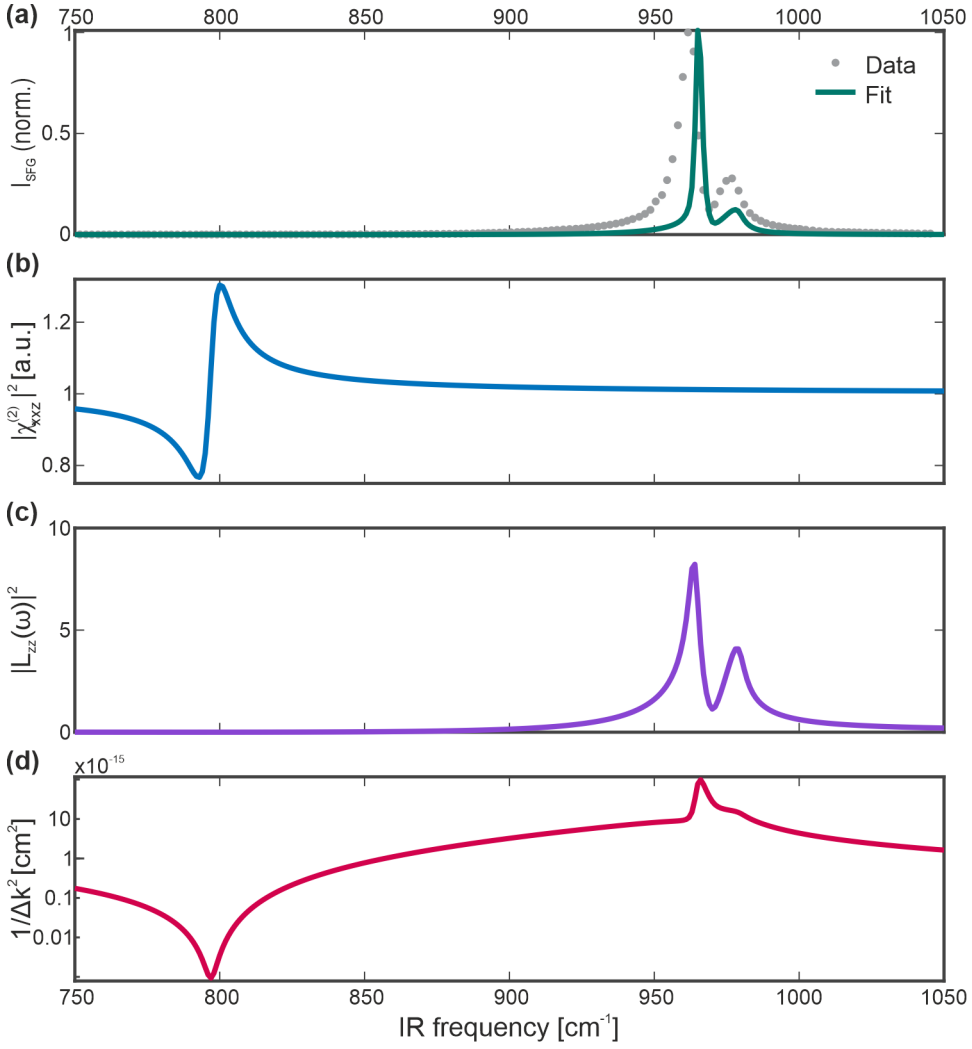

Figure 3.4. *Different contributions to the SFG intensity on the example of SiC.* (a) The total SFG intensity can be calculated (green line) to nicely fit experimental data (gray dots). The general contributors to the final shape of the spectrum are (b) the non-vanishing second-order nonlinear susceptibility component $\chi^{(2)}_{xxz}$, (c) the Fresnel element L_{zz} and (d) the phase-matching coefficient $1/\Delta k^2$ (with y-axis in log-scale).

z-field wavevector component k_z for incident (i) and transmitted extraordinary (t,e) waves.

It can be seen in Fig. 3.4, that for this configuration the main contribution for the SFG intensity spectrum comes from the Fresnel transmission coefficient. The first peak appears at the extraordinary LO frequency of SiC, where the substrate supports the transmittance of the IR beam best. Here, Eq. (3.2.28) becomes large because the first denominator $\varepsilon_{\parallel}$ is zero. The second peak arises at the root of the second denominator which is dependent on the ordinary LO frequency and k_z which shifts with the incidence angle of the excitation beam. The nonlinear susceptibility peak disappears in the intensity plot because its variation is orders of magnitude smaller than the variation in L_{zz} but mainly due to phase-matching. Panel (d) demonstrates the importance of phase matching, as, the dip at $\omega_{TO} = 797\,\mathrm{cm}^{-1}$ prevents the

observation of the TO resonance peak in the SFG spectrum although apparent in the $\chi^{(2)}$-contribution.
For different geometries, or other materials, the relative contributions to the SFG signal can vary significantly and peaks appear not only due to the Fresnel coefficients. Compare, e.g, the case for α-quartz in Ref. [100].

3.3 SFG microscopy

Sum-frequency generation microscopy relies on the mixing of two optical fields. Essential to this thesis is the mixing of fields on the sample surface. In SFG experiments, the sample is resonant to one frequency ω_1 and generates a sample response, which is upconverted with the second optical field at frequency ω_2. Usually, one uses a combination of an infrared and a visible laser. The infrared laser can probe vibrational resonances of the material, while the visible beam leads to an upconverted signal in the visible regime, which is easily detectable with established detectors like CCD cameras or PMTs.

After the previous discussion of the theory behind nonlinear optical processes in general, and sum-frequency generation in specific, the next section deals with the experimental implementation of the sum-frequency technique for optical microscopy. The scanning-focus method will be compared with a wide-field approach. SFG wide-field microscopy is then discussed in greater detail and advantages in comparison to the scanning-focus method are laid out, such as overcoming sample damage induced by tight focusing.

3.3.1 Scanning-focus vs. wide-field SFG microscopy

The first sum-frequency generation microscope was demonstrated in 1999 [111] using a wide-field illumination geometry. By now, two main techniques are in use, which are wide-field illumination and the scanning-focus technique [112]. Both techniques have many advantages, and can be used to address a variety of research questions.
In the scanning-focus approach, the two IR and VIS laser beams are focused tightly to µm-sized spot sizes on the sample surface. Due to the tight focus, lasers with high repition rate and a small fluence are favorable for this technique [23]. The laser beams are either scanned over the sample surface or the sample is mounted on a sample stage allowing for movement into all directions. The SFG signal is either picked up by a lens, and guided towards a detector [112], or alternatively can be also probed by a metallic tip [113].
In wide-field illumination, the laser beam illuminates the whole field of view, with an optional soft focus depending on the actual spot size. Due to the larger spot sizes, high power lasers with low repetition rates are the optimal choice for wide-field SFG microscopy [114].

In general, the low SFG intensity at sample surfaces and interfaces requires the

integration over several laser shots to detect sufficient signal [114]. Consequently, the scanning-focus geometry leads to long acquisition times compared to the wide-field geometry, despite the favorable use of high repetition lasers. Although acquisition times on the order of seconds per frame have been reported for the scanning-focus approach [25], common acquisition times are usually longer, in some cases reaching up to more than an hour for a single image [69]. Simultaneously, the tight focusing can easily lead to sample damage, which can be prevented by the wide-field setup [69, 114]. Regarding the resolution, scanning-focus approaches are able to collect images with a resolution close to the diffraction limit and below. The resolution is ultimately mainly dependent on the size of the foci, which can be extremely small due to the less powerful pulses mentioned before [23]. If a nanoscopic tip is used, the diffraction limit can be overcome, and resolutions on the order of the size of the tip, i.e. 50-100 nm, can be reached [113]. However, the tip usually is metal coated which can produce other nonlinear signals than the SFG signal from the sample, disturbing the measurements, and making the subsequent data analysis more complicated [115]. In contrast to a scanning-focus method, wide-field illuminated images possess, though ultimately limited by the diffraction limit, resolutions on the order of $\approx 1\,\mu m$ [116].

Both methods clearly show their advantages, in different ways, fitting to different research questions. After the successful implementation of a scanning-focus SFG microscope in the scope of a former thesis [69, 117], this work focuses on the method of wide-field SFG microscopy, which will be further discussed on the next pages.

3.3.2 Wide-field SFG microscopy

In this thesis, a wide-field SFG microscope is implemented using the light from a free-electron laser as an IR excitation source. Different possible implementations and geometries of such a microscope will be discussed in the following. Here, a distinction is made between oblique and normal incidence illumination by the visible laser. This choice leads to effects on the focal plane, as discussed below. Since only the visible upconversion beam is important for the focal plane, the discussion here leaves out the IR beam.

Wide-field focal plane

Oblique incidence microscopes have great advantages, such as applicability to opaque samples [114]. However, in general, wide-field imaging requires an objective to collect the image data. This becomes challenging for oblique incidence imaging, where it limits the ability to have the whole field of view (FoV) in focus, as depicted in Fig. 3.5(a). With an objective tilted with respect to the incident beam, only a small stripe of the FoV is in focus [111], where the size of the stripe is related to the angle of the incident light and the objective's NA.

These image distortions can be overcome by adding a relay imaging system and a

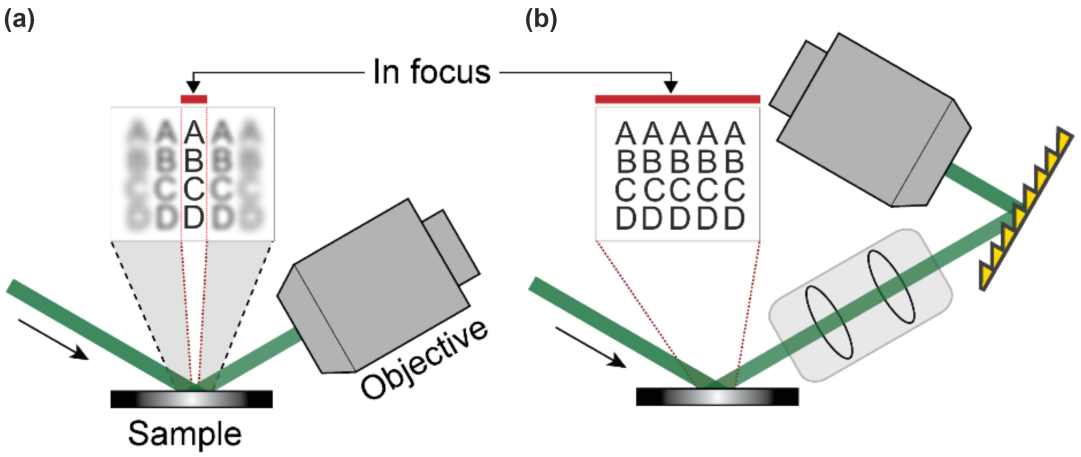

Figure 3.5. *Correction of image distortions from oblique-incidence imaging.* (a) Oblique wide-field imaging leads to FoV areas out of focus, generating a distorted image. (b) Image distortions can be overcome by adding a relay-lens system and a grating to correct the image focus. Reprinted with permission from [P2], © Optica Publishing Group.

grating to the setup, see Fig. 3.5(b). In this case, the relay lenses project the light from the sample onto a grating which compensates the prior image distortions [114, 118]. The light is then picked up by an objective at normal incidence towards the grating surface which generates a distortion-free image, with the whole FoV in focus.

A simpler geometry for a focal plane parallel to the sample surface can be achieved by illuminating the sample under normal incidence by the upconversion beam. This method brings the great advantage of an evenly-illuminated sample surface, with one focal plane for the whole image, but also faces some disadvantages which will be discussed in the following section.

Configurations for wide-field SFG microscopy

Several different configurations to set up a microscope exist, and can be modified to implement an SFG microscope. Three of these configurations are most important in the context of this thesis and are discussed in the following. In Fig. 3.6, sketches of these three techniques are displayed. The IR beam illumination is always under oblique incidence, and only the sample illumination by the visible beam is changed according to the three different techniques. First, a microscope using reflection illumination is discussed, where the visible laser beam illuminates the sample after passing through the objective. Second, microscopy using back illumination shall be explained, where the sample is illuminated from the backside by the visible laser. Last, a setup using Schwarzschild imaging based on a reflective objective is discussed, where the SFG light is collected by an objective consisting of mirrors instead of lenses.
Due to the large difference in IR and VIS frequencies, the SFG light direction can be approximated by the visible beam direction, as in Eq. (3.2.19). The working princi-

ples of all considered geometries are outlined.

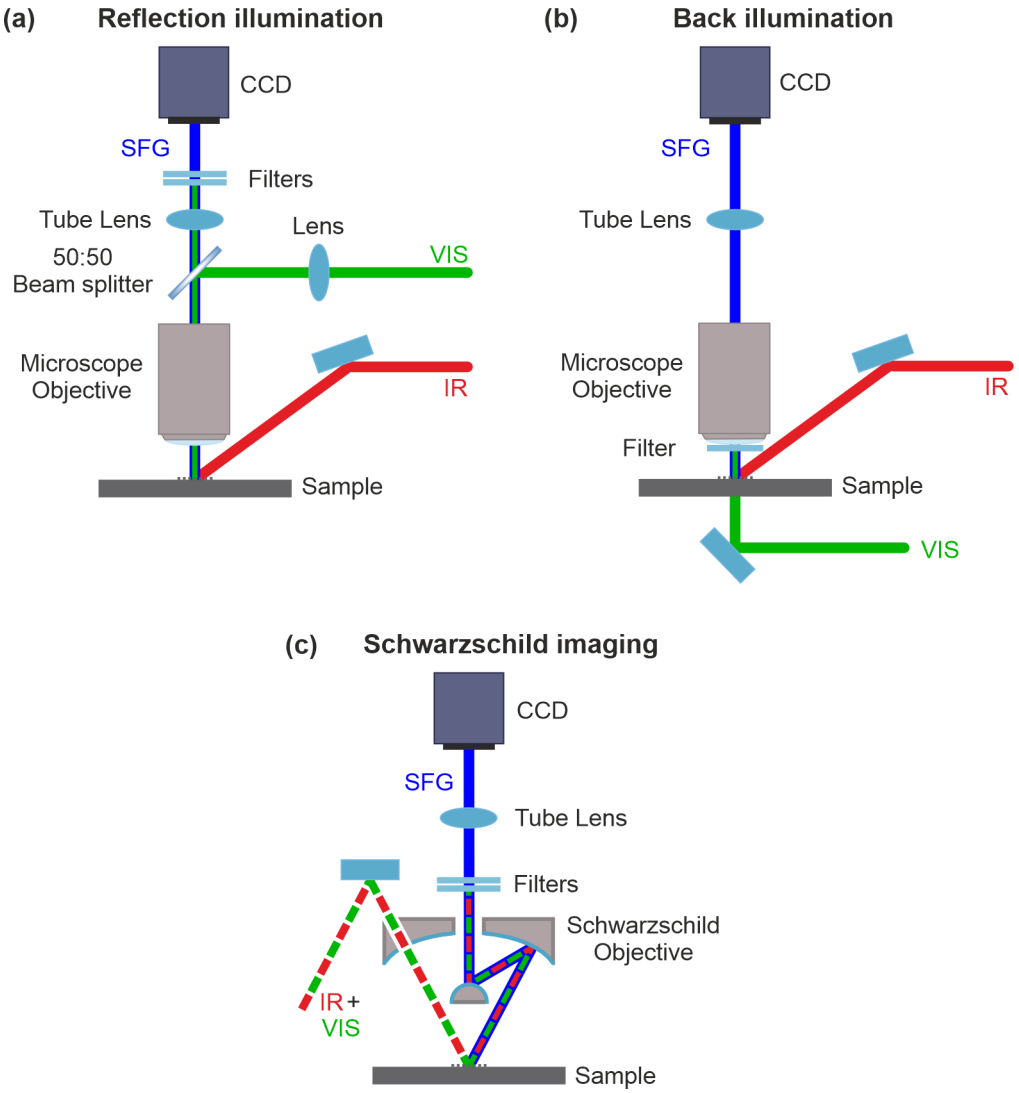

Figure 3.6. *Overview of different SFG microscopy configurations.* The visible laser beam is guided through the objective in (a) reflected illumination microscopy, while it illuminates the sample from the backside in (b) back-illumination microscopy. The technique of (c) Schwarzschild imaging makes use of a reflective objective made of two mirrors instead of a set of lenses. Adapted from [P2].

Reflection Illumination Fig. 3.6(a) illustrates an SFG microscope using reflection illumination, where the VIS is guided towards the sample by passing the objective. Here, the VIS beam is focused onto the back focal plane of the objective and is recollimated by the objective onto the sample to illuminate the whole FoV [119]. Therefore, a 50:50 beam splitter is required, to combine the VIS beam path with the microscope's beam path. Additional filters between beam splitter and camera are necessary to only transmit SFG light for detection with the camera. By illuminating the sample surface from the front, the technique can be used for transparent as well as opaque samples.

Back Illumination In SFG microscopy based on back illumination, the upconverting beam is illuminating the sample from the backside, under normal incidence. Therefore, this technique is only suitable for samples non-opaque for the visible spectral range. The visible laser beam is in one direct line with the objective, making an additional bandpass filter in front of the objective indispensable for avoiding laser-induced damage in the objective's optics. Any additional optics behind the objective such as the 50:50 beam splitter, as in the reflection configuration, are not nedded, providing easier alignment.

Schwarzschild Imaging In a microscope based on Schwarzschild imaging, a special reflective objective, a so-called Schwarzschild objective [120], is used. In comparison to a classical lens objective a Schwarzschild objective does not contain any lenses, but mirrors, to guide the light. As illustrated in Fig. 3.6(c), it contains two mirrors, the larger primary mirror at the shell of the objective and the smaller secondary mirror placed in the center of the objective. Due to the absence of lenses, a Schwarzschild objective comes with the great advantage of no chromatic aberrations. For the purpose of an SFG experiment, the main issue is the irradiation of the sample with the IR laser. Due to the lateral size of the reflective objective, IR illumination of the sample bypassing the objective has to take place at a very large angle of incidence. Thus, excitation of the sample becomes a complicated task. In the depicted case in Fig. 3.6(c), this challenge was overcome by a custom-made hole drilled into the objective [P2]. With this technique, the resonant laser beam can excite the sample under an arbitrary angle without causing critical damage to the objective as would occur for a lens objective. However, once implemented, the angle is fixed and cannot be changed without exchanging the objective. This approach overcomes the disadvantage of only illuminating the sample from the backside, as the upconversion laser can be guided through the hole as well. As with the other configurations, filters behind the objective are needed to block the VIS and also the IR beam.

All geometries show advantages, making them a valid method depending on the sample choice. While the geometry based on Schwarzschild imaging was implemented in a different setup [P2], the first two techniques will be set into this thesis' context in the section regarding the actual SFG microscopy setup, see Sec. 4.3.2.

4

Experimental Methods

In this chapter, the experimental tools and instrumentation for all the measurements will be explained. First, the working principle of a free-electron laser is discussed, followed by an overview of the FHI-FEL setup, see Sec. 4.1. Second, the table-top laser systems used for the sum-frequency generation are introduced and the synchronization between the pulse structure of the FEL and the table-top sources is explained, Sec. 4.2. Finally, the experimental setup that controls the temporal delay between infrared and visible pulses and the actual sum-frequency generation microscope are introduced and discussed step-by-step in Sec. 4.3.

Parts of this chapter have been published in [P1].

4.1 Infrared free-electron laser

The free-electron laser (FEL) of the Fritz Haber Institute is in operation since 2013 [121]. The FEL started with a single color beamline in the mid-infrared, with an extension to a second-color beamline in the far-infrared, where first lasing was achieved in June 2023. In the following, the general working principle, as discussed in Ref. [122, 123], as well as the setup and the main characteristics of the FHI-FEL will be introduced.

4.1.1 Working principle

In a free-electron laser, the kinetic energy of electrons accelerated to relativistic velocities is converted to photons by guiding the electron beam through an alternating magnetic field. Here, the electron beam does not only act as pump source for the radiation but also as a gain medium [123]. Roughly speaking, a free-electron laser consists of three main parts, namely an electron accelerator section, an undulator and an optical cavity. This simplified picture is sketched in Fig. 4.1.

The electrons are accelerated to a velocity close to the speed of light, and therefore need to be considered as relativistic particles. To achieve radiation in the mid-IR regime, electron energies in the range of tens of MeV are needed. After generation in an electron gun, the acceleration of the electrons is typically done by a linear accelerator (linac).

In a linac, the electrons are guided through radio frequency (RF) cavities, which

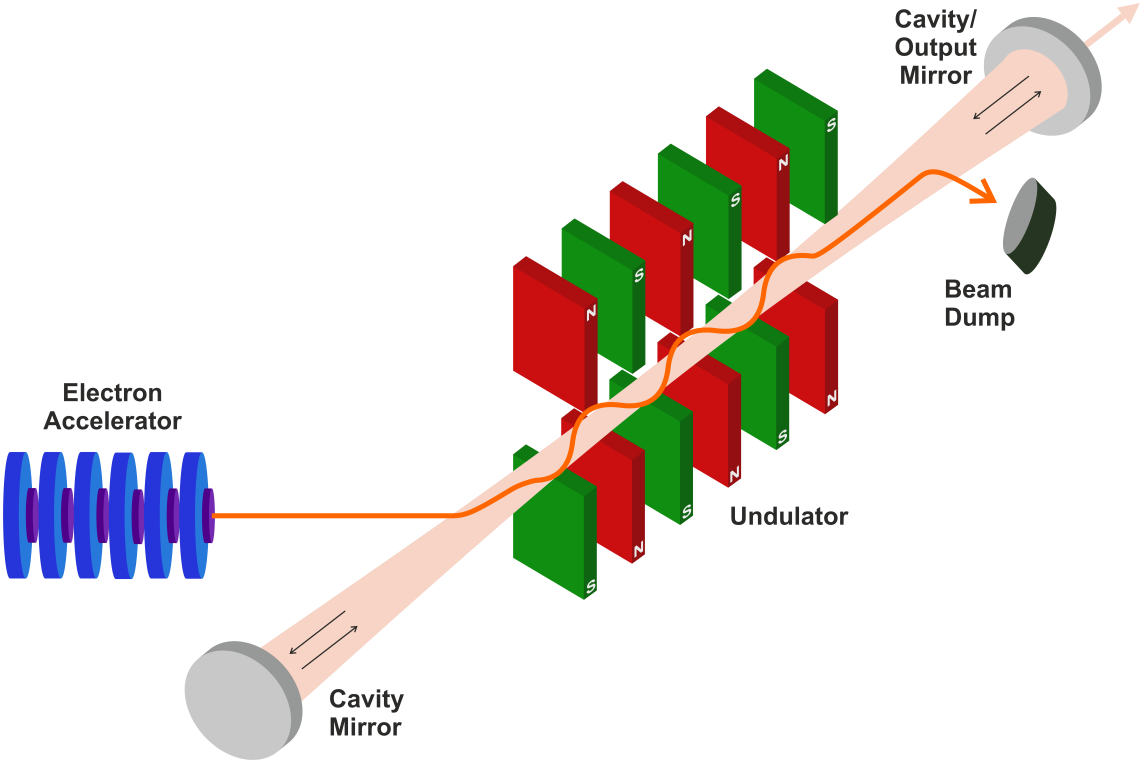

Figure 4.1. *Simplified sketch of a free-electron laser setup.* The electrons are generated and accelerated in a setup of electron gun and linear accelerator, then enter the undulator where they are guided onto a curved trajectory. Each turn results in electromagnetic radiation, i.e., photons. Within the cavity, the photons acquire a huge gain by passing the undulator several times before outcoupling. Adapted from [123].

are coupled to an AC voltage source and are charged alternately. Due to the charge difference between the cavity field and the electrons, the electrons are accelerated along their path through the cavities. The frequency of the AC voltage and the length of the cavities is adjusted such that switching of the voltage polarity happens after the electrons passed exactly one cavity. Using this technique, electron energies of tens of MeV can be reached [124].

After acceleration, the electrons are guided to the undulator by electron optics. The undulator consists of periodically-arranged magnet pairs with alternating polarities. Due to the magnetic field, the electrons experience a Lorentz force resulting in a sinusoidal motion with the same periodicity as the undulator magnets (λ_U). At each turning point of the electron beam's trajectory, each electron emits incoherent electromagnetic radiation, i.e., synchrotron radiation with a wavelength λ_L.
To obtain constructive interference of the synchrotron wave pulses, the so-called resonance condition must be satisfied. To derive this equation, a closer look at the electron movements in the undulator is helpful, see Fig. 4.2. In the moving frame of the electron, the synchrotron radiation is emitted in all directions, but from the lab frame the electrons move with nearly the speed of light along the undulator axis such that the radiation emerges almost entirely in forward direction, parallel to the electron beam.

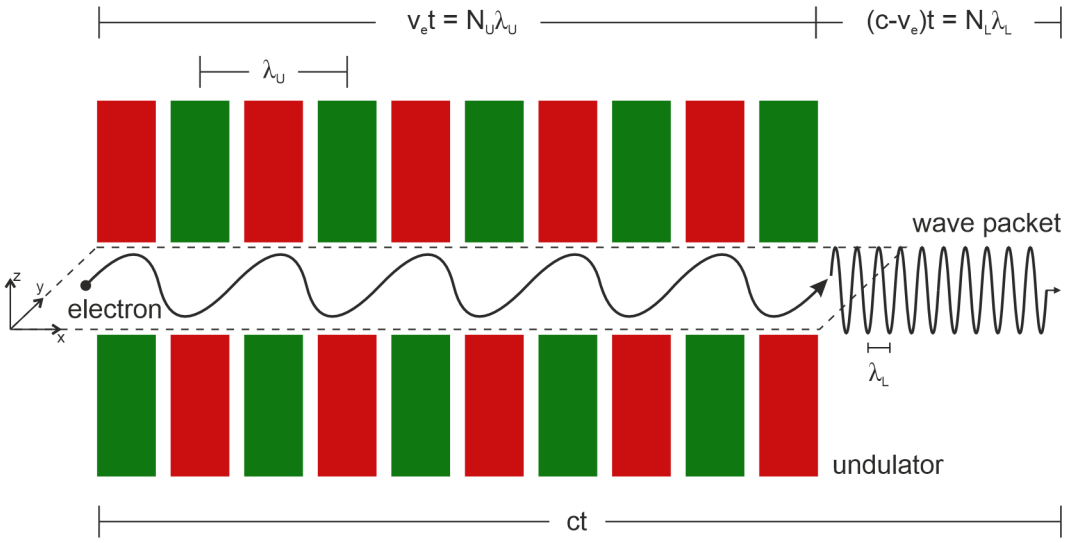

Figure 4.2. *Electron motion in the undulator.* Due to the different velocities of electrons and photons, the emitted wave packet has a spatial length of $(c - v_e)\,t$. Adapted from [122].

The relativistic velocity of a single electron is $v_e = \beta c$ at a fraction β of the speed of light c. The time the electron bunch needs to move through the undulator is $t = L_U/v_e$ with $L_U = N_U \lambda_U$ the length of the undulator, N_U the number of periods and λ_U the period length. By passing the undulator, an electron emits photons at every turn on its trajectory which are forming a wave packet. Because of the different velocities of electrons and light, the wave packet has a spatial length of $(c - v_e)\,t$, i.e., while the front of the wave packet emitted at the beginning of the undulator moved the distance ct, the back of the wave packet is approximately at the end of the undulator at $v_e t$. Similar to the undulator, the wave packet also contains N_U oscillations. Its wavelength λ_L can therefore be written as [122]

$$\lambda_L = \frac{(c - v_e)\,t}{N_U} = \frac{\lambda_U\,(1 - \beta)}{\beta} = \frac{\lambda_U}{2\gamma^2} \tag{4.1.1}$$

using the approximation of $\beta \approx 1$ for electrons very close to the speed of light and the Lorentz factor $\gamma = 1/\sqrt{(1 - \beta^2)}$.
This derivation has so far neglected the oscillatory motion of the electrons which increases the path length of the electrons trajectory significantly, depending on the magnetic field strength. As a consequence, the average electron velocity is reduced, and thus the wavelength of the emitted light increases. By taking this effect into account, the full resonance condition can be formulated as [122, 125]

$$\lambda_L = \frac{\lambda_U}{2\gamma^2}\left(1 + K^2\right), \qquad \text{with } K = \frac{eB_U\lambda_U}{2\pi m_e c}. \tag{4.1.2}$$

K is the so-called undulator parameter with the electron charge e, the magnetic field

B_U and the electron mass m_e.
The emitted wavelength of the synchrotron radiation can thus be controlled either by changing the Lorentz factor γ via the linac's electron energy, or by varying the undulator parameter K via the magnetic field strength, which can be done by adjusting the gap size between the pairs of magnets [122, 125]. After the undulator, the electron beam is guided to a beam dump.

It was mentioned before that the electron beam acts not only as a pump source, but also as the gain medium. To make use of the gain for lasing, the setup additionally requires a cavity, see Figs. 4.1 and 4.3. With an optical cavity, i.e., two concave mirrors, at both ends of the undulator, the emitted, incoherent radiation can be made coherent. Due to the cavity, the optical beam passes the undulator and the electron beams several times for a strongly increased gain and is finally outcoupled through a small hole in the second cavity mirror. For an efficient increase in gain, not only a cavity, but the process of microbunching [126], is important, see Fig. 4.3. The electron beam and the optical beam are propagating parallel to each other through the undulator, leading to the electrons' motions being either parallel or antiparallel to the electric field gradient of the optical wave. Close to resonance (Eq. (4.1.2)) optical and electron beam have similar frequencies, therefore the electrons lose energy if both beams are in phase. Thus, the faster electrons soon catch up with the slower electrons, forming electron microbunches in the electron beam. These microbunches are now in phase with the optical field, leading to radiative emission that adds up coherently with the optical field, which gets amplified by a positive gain.
However, if the electrons exactly fulfill the resonance condition, the net gain is zero, due to no phase advance. Therefore, to achieve positive gain of the optical beam, the electron energy must be set slightly higher than resonance, so that the electrons are able to lose energy to the photons. Once the energy loss is such that the electrons are at resonance, the laser intensity saturates at an intensity several orders of magnitude larger than without cavity.

For operation in user experiments, different wavelength regimes are required which can be pre-set by accelerating the electrons to a specific energy. The wavelength can then be finely tuned by varying the undulator gap size, and thus the magnetic field strength. To achieve best efficiency for a given wavelength regime, the effective cavity length L_C can be changed by moving one of the cavity mirrors to satisfy the condition

$$L_\mathrm{C} = L_0 - q\lambda, \tag{4.1.3}$$

with the nominal cavity length L_0, the output wavelength λ and the cavity detuning q. Here, q is a user-defined value usually in the range of $0 < q < 5$ which is kept constant during a wavelength scan to increase the accessible wavelength range. The cavity detuning also has great impact on the laser bandwidth, which decreases with increasing q, leading to a handle for improvement of the spectral resolution, which

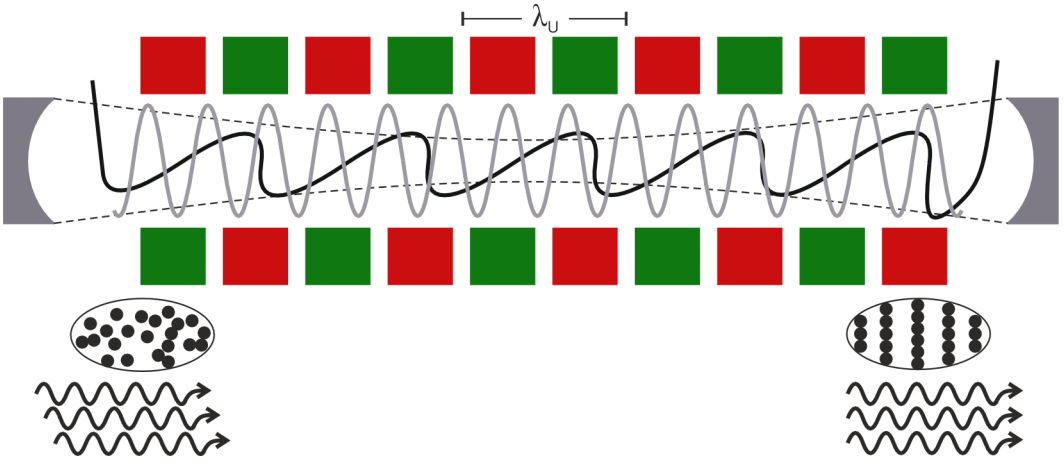

Figure 4.3. *Sketch of microbunching process.* When entering the undulator, the electrons have different phases. While going through the undulator, the electron beam interacts with the generated optical beam, such that electrons in phase with the optical beam are slowed down. The faster electrons soon catch up with slower electrons and lose energy themselves, thus forming electron bunches which are in phase generating coherent light emission. Based on [127].

is favorable for spectroscopic or microscopic wavelength scans [128].

4.1.2 FHI-FEL setup

After the discussion of the general working principle of free-electron lasers in the preceding section, the following section shall give an overview of the FHI-FEL facility and its important characteristics according to Refs. [121, 128, 129]. First, the preparation of the electron beam in the electron gun and the linacs are introduced before the electron beam is split into two arms for mid- and far-IR laser beam production, respectively. Secondly, the undulators and cavities of these two arms are discussed in greater detail. An overview over the whole setup is depicted in Fig. 4.4.

Electron gun and accelerators

To achieve laser radiation in the IR regime, electrons with energies of tens of MeV are needed. The accelerator system here offers electron energies from 15 to 50 MeV. Before the electrons can be accelerated, they are produced in a gridded thermionic electron gun made of tungsten from where they are accelerated to the anode by a potential difference of 38 kV. The electron gun is driven at the third sub-harmonic of an RF master oscillator (MO) at $f_{\mathrm{gun}} = f_{\mathrm{MO}}/3 \approx 1\,\mathrm{GHz}$ with $f_{\mathrm{MO}} = 2.998\,\mathrm{GHz}$. The RF MO works as a clock for all components of the FEL setup. After the gun, a 10 Hz macropulse structure is generated due to the necessity of the capacitors to recharge. The electron bunches inside a macropulse (10 µs) are on the order of hundreds of ps, which is too long for efficient acceleration in the linacs. Therefore, between the gun and the first linac, a 1 GHz buncher cavity compresses the electron bunches in time to a few ps. The electron accelerators are two S-band standing-wave

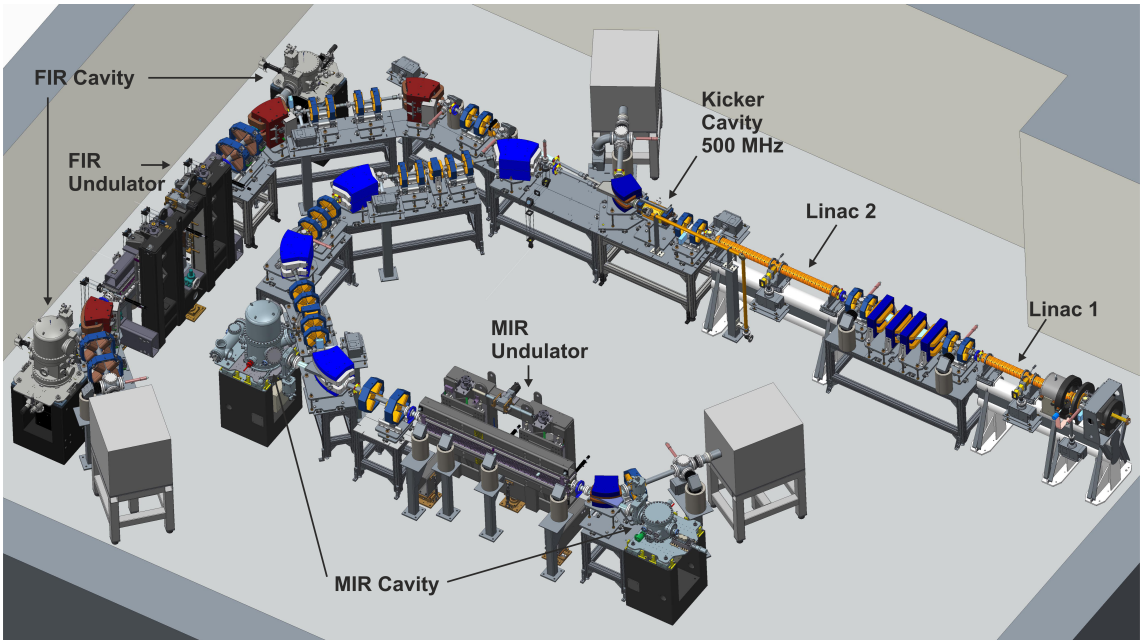

Figure 4.4. *Sketch of the FEL at the Fritz Haber Institute.*

$\pi/2$ copper linacs, both operating at f_{MO} and powered by microwave radiation with $P_{\mathrm{mw}} = 30\,\mathrm{MW}$. In the first linac, the electrons are accelerated to a constant energy of 20 MeV corresponding to a velocity of $v_{\mathrm{e}^-} = 0.9997\,c$, while the second linac de- or accelerates the electrons to their final energy of 15-50 MeV. Between the linacs, a chicane can be used to compress the electron bunch length down to a minimum of 1 ps rms. The electron bunches have a charge of approx. 200 pC at a repetition rate of 1 GHz. Thus, the FEL provides high-power macro-/micropulses. All important values are summarized in Tab. 4.1 below.
If desired, the electron gun can also be driven with other sub-harmonics of the RF MO frequency, leading to optional frequencies of 27.8 MHz and 55.5 MHz. For all experiments described in later chapters, the gun is driven with the 55.5 MHz sub-harmonic of the RF MO, corresponding to micropulses with a duty cycle of 18 ns.

Table 4.1. Specifications of the pulse preparation at the FHI FEL.

Parameter		*Value*
Electron energy	E_{kin}	15-50 MeV
Electron bunch charge		200 pC
Micropulse repetition rate		1 GHz / 55.5 MHz / 27.8 MHz
Micropulse length	τ_{micro}	1-5 ps
Macropulse repetition rate		10 Hz
Macropulse length	τ_{macro}	1-15 µs

Undulators and cavities

After acceleration in the linacs, the electrons are guided to the undulator. To date, only the mid-IR undulator is in use for experiments, but the far-IR undulator arm is set up and will be put into user operation shortly. After successful implementation, the FEL can be used in two-color operation, offering two optical beams simultaneously. The beams are divided by a 500 MHz kicker cavity which deflects the beam by either 0° into the mid-IR undulator arm or by −4° into the far-IR undulator arm [129].
The electron beam is guided through 90°-isochronous achromats to reach the undulators. The most important characteristics of the undulators and cavities are summarized in Tab. 4.2. Both the mid- and far-IR undulators are placed within cavities of 5.4 m length each. The mid-IR undulator (*STI Optronics, Inc.*) consists of NdFeB permanent magnets and has a total length of 2.0 m containing 50 periods with a length of 40 mm. For the minimum undulator gap size of 16.5 mm, a K parameter of 1.6 is reached; theoretically, a maximum wavelength of more than 50 µm can thus be reached. The successfully obtained maximum wavelength is about ≈ 45 µm. For the cavity, two concave gold mirrors are used as cavity end mirror and outcoupling mirror, respectively. The cavity end mirror is mounted on a stage to set the cavity length with 1 µm precision. Depending on the wavelength range, the outcoupling mirror can be one of five mirrors with a hole of 0.75, 1.00, 1.50, 2.50 or 3.50 mm diameter in the center, respectively, to obtain the best performance.
For the far-IR undulator, a wavelength range of $5\,\mu\text{m} \leqslant \lambda_\text{U} \leqslant 166\,\mu\text{m}$ is predicted. It also consists of NdFeB permanent magnets and has 40 periods with a period length of 110 mm adding up to a total length of 4.4 m. User experiments will be possible in the near future with the option of 2-color lasing, where both FEL arms are generating photons simultaneously for, e.g., FEL-only two-color pump-probe experiments.

Table 4.2. Specifications of the mid- and far-IR undulators and cavities.

Parameter		*mid-IR*	*far-IR*
Undulator length	L_U	2.0 m	4.4 m
Undulator period	λ_U	40 mm	110 mm
Number of periods	N_U	50	40
Cavity length	L_0	5.4 m	5.4 m

User operation details

Once the optical beam is outcoupled from the cavity, it is guided to the user stations through an evacuated beam line. Between the FEL bunker and the experiments, a diagnostic station is employed to monitor the FEL pulse energy and the spectral profile. To vary the FEL intensity, five wire-grid attenuators of different power transmission levels (50 %, 33 %, 14.5 %, 13 %, 12 %) can be placed into the beam line. Shortly before the user station, the FEL passes a focusing mirror creating a focal

point at the experiment table after 4 m. The FEL leaves the evacuated beam line through a KRS-5 window, which is transparent for mid-IR light from 0.6 µm to 40 µm. For on-site beam alignment, light of a visible laser diode generating an optical beam at $\lambda_{\text{align}} = 635$ nm can be flipped in that follows the exact same beam path as the FEL.

4.2 Table-top laser systems

For the visible laser beam, two laser systems are in use. Both laser systems produce green laser light by frequency-doubling of a near-IR laser beam. The green light is used for the sum-frequency generation microscope, while the original near-infrared beam is used to find the correct timing between the pulses of the table-top laser and the FEL.
The experimental setup of the microscope started with usage of a 55 MHz pulsed fiber oscillator (*Origami 10 HP, OneFive*) with $\lambda = 1054$ nm. To be prepared for future experiments on samples with a small field enhancement and thus only weak SFG signal, a new high-power laser (*Agilite 569 Burst*) was implemented to the setup as part of this thesis work, emitting 1064/532 nm light with the same pulse structure as created by the FEL.

4.2.1 Origami OneFive: 1054 nm

The 1054 nm light source, in the following referred to as OneFive, is a terbium-doped fiber oscillator (FO) offering high-power laser pulses on the order of 100 fs with ≈ 50 nJ pulse energy and a repetition rate of 55.5 MHz. The near-infrared light of 1054 nm has a maximum power of ≈ 3 W directly behind the output. The green light of 527 nm is generated by second-harmonic generation (SHG) in a BBO crystal behind the laser output with a maximum power of ≈ 1 W. A dichroic mirror, which is transmissive for the near-IR light and reflective for the visible light, separates the beams into two beams for individual or simultaneous usage.

Initial experiments testing the microscope using this laser were performed on SiC, a material with a large field enhancement. In the future, experimental focus might be put on materials with lower field enhancement or monolayer samples. Thus, a new customized, high-power table-top laser was purchased. The OneFive laser was used to determine the microscope's resolution, see Chapter 5. All later experiments, Chapters 6-9, are based on the new laser system, which is introduced in the following.

4.2.2 Agilite Burst: 1064 nm/532 nm

The *Agilite 569* burst laser system (hereafter referred to as burst laser) provides the experiment with 1064 nm and 532 nm pulsed laser beams. Both beams can be outcoupled individually for simultaneous application. The burst laser is a customized, high-power pulsed laser system with a macro-/micropulse structure similar to the FEL pulse structure. It consists of two main components: the seed oscillator (*M-PICO-LAB Nd:VAN [PR132], Montfort*) generates micropulses at 1064 nm with a duration of $\tau_{\mathrm{micro}} = 4\,\mathrm{ps}$ and the amplifier system (*Agilite 569-10, Continuum*) shapes the beam into macropulse structure with a repetition rate of 10 Hz and a pulse length of $\tau_{\mathrm{macro}} = 10\,\mu\mathrm{s}$ with subsequent amplification by flashlamp pumped laser heads. Through gain narrowing during the amplification, the amplifier micropulses have a duration of $\approx 11\,\mathrm{ps}$. In the amplifier system, the beam shape is adjusted such that the output beam has a flat-top profile instead of a Gaussian shape. This characteristic is beneficial for homogeneous illumination of the microscope's FoV.
A full sketch of the beam paths in the seeder and the amplifier system can be found in the Appendix A.1. Here, the system and the operating mode shall only be introduced briefly.

The seed laser crystal is pumped by an external laser diode which is located in the laser controller and fiber-coupled to the laser head. The pump light is focused onto the laser crystal, resulting in an amplification sufficient for lasing in the cavity. The cavity is a linear cavity with two end mirrors and has a total length of 2.7 m resulting in pulsed laser light of $f = 55.518\,\mathrm{MHz}$. The output coupler mirror transmits a few percent of the laser light generating the output beam. The second end mirror of the cavity is a SeSAM (semiconductor saturable absorber mirror) [130], which absorbs a small part of the laser light. With higher intensities, the absorption saturates leading to higher reflection and stabilized mode-locked lasing. The output beam has a power of $\approx 200\,\mathrm{mW}$.
A subsequent Faraday isolator protects the seeder from any back-reflected signal. For macropulse shaping, a part of the beam gets deflected to its first order by an acousto-optical modulator (AOM). The deflected beam is amplified in a double-pass 5 mm Nd:YAG flashlamp based amplifier. After the double-pass, the polarization is rotated by a Faraday-isolator from p- to s-polarization and the laser light is guided to the dual 6 mm amplifier while passing a telescope to slightly widen the beam. After the 6 mm amplifier, a Pockels cell is used for sharpening the square macropulse edges. The beam is magnified to fit the dual 9 mm amplifier where the laser beam is amplified to its final 670 mJ per macropulse. For frequency-doubling, the beam passes a removable potassium titanyl phosphate (KTP) SHG crystal resulting in 320 mJ per macropulse visible light. Behind the KTP crystal, a near-IR transmissive and visible reflective dichroic mirror separates the two beams for individual usage. After outcoupling to the optical table, both laser beams can be attenuated as needed by a $\lambda/2$-waveplate and a polarization beam splitter.

The burst laser can be operated with an internal or an external trigger. For align-

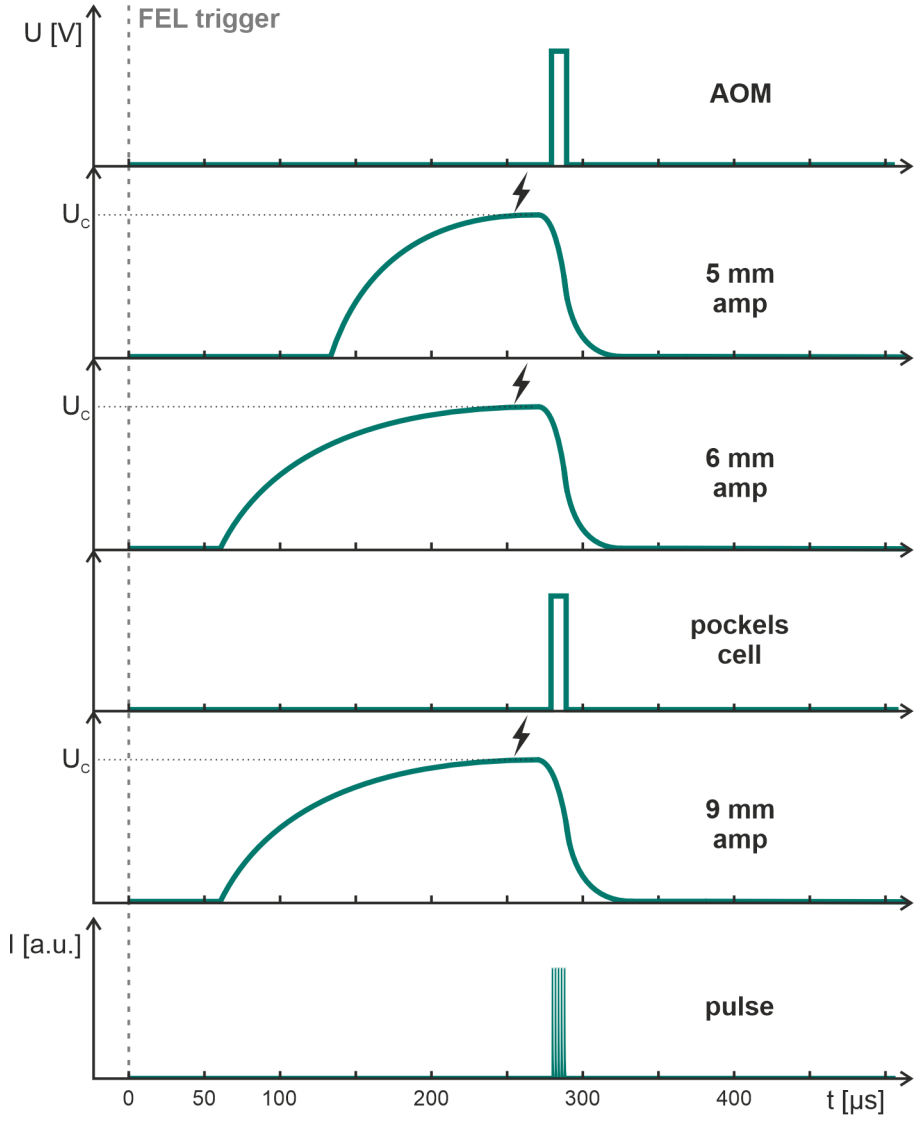

Figure 4.5. *Conceptual sketch of the amplification process timings.* After the FEL trigger, the capacitors of the amplifiers are charged to power the flashlamps, when reaching the critical voltage U_C. AOM and Pockels cell are engaged slightly later to shape the 55.5 MHz pulses into square-shape macropulses. The plots are arranged in order of appearance in the setup.

ment processes, the internal trigger mode is used, whereas for experiments in the SFG microscope the FEL trigger is used as an external trigger. With the trigger, the time course of pulse shaping and amplification is controlled. A conceptual sketch of the different timings is illustrated in Fig. 4.5. The timing curves are plotted in the order of appearance in the setup (top to bottom), which is not identical with the order of temporal control. Due to the necessity of charging, the amplifiers start working at an earlier time than AOM and Pockels cell. The concrete timing values are given in the Appendix A.1. With respect to the trigger signal, the 9 mm- and 6 mm-amplifiers are electrically engaged to charge the capacitors. The smaller 5 mm capacitor is engaged tens of microseconds later to start the charging process as well. The required time scale for optimal output has been tested experimentally by vary-

ing the set times and simultaneous power detection of the output beam. It matches such that the capacitor reaches the critical voltage U_C for optimal discharge, i.e., it discharges a maximum amount exactly when the laser pulse enters the respective amplifier (see U_C and flash in Fig. 4.5). Thus, shifting the charging of the capacitors leads to lower output power. This is, e.g., used for laser alignment processes.
For pulse shaping, the AOM and the pockels cell are required. Here, a larger delay with respect to the trigger is set, matching the maximum charge state of the respective capacitors. By switching to the first order, the AOM picks out a short sequence of the 55.5 MHz micropulses, thus generating a macropulse structured beam. To suppress any occuring amplified spontaneous emission (ASE) signal and sharpen the pulse edges the ASE suppressor triggers the pockels cell simultaneously to the AOM. In this schematic, the AOM modulation voltage is simplified to a rectangular curve while in actual use a specified voltage curve is required due to the time-dependent gain in the amplifier crystals. This effect arises since the crystals are optically pumped by flash lamps only once just before the start of the macropulse. Any gain throughout the macropulse continuously reduces the population inversion and thus the gain for the remaining macropulse, see Fig. 4.6(b)
For optimal experimental conditions, a square-shaped macropulse is required which is achieved by an AOM voltage curve with increasing voltage over time. Fig. 4.6 illustrates the two operation modes for regular pulse shaping (a-c), where the AOM voltage switches between a minimum and maximum value, and for square pulse shaping (d-f) as used in this laser system. By driving the AOM with an increasing voltage curve instead of a constant voltage, the pulse shape can be controlled.

In theory, the AOM voltage curve is designed in a way to achieve a perfect square-shaped pulse. In lab conditions, though, the finite number of curve points limit the actual pulse shape quality. An image of the experimentally achieved pulse shape is shown in Fig. 4.7 for the macropulse structure (top) and a zoom into the micropulse structure (bottom).

4.2.3 Synchronization

For the sum-frequency generation experiments, it is indispensable to have temporal overlap of the FEL and table-top laser pulses not just on the macropulse level, but also for the 11 ps micropulses. The method to achieve the overlap on the optical table is described in Sec. 4.3.1. As a step beforehand, both laser systems are synchronized electronically to have a stabilized pulse timing with respect to each other [131]. The synchronization between the FEL and the OneFive laser was developed by Riko Kiessling as part of his PhD thesis [117] and is described there in great detail.

An electronic phase-locking technique has been utilized where the frequency of the FEL master oscillator f_{MO} is used and coupled to the lab by a stabilized fiber link. The 54^{th} harmonic of the OneFive's output is compared to the FEL master oscillator phase, in order to manipulate the fiber oscillator cavity such that synchronized

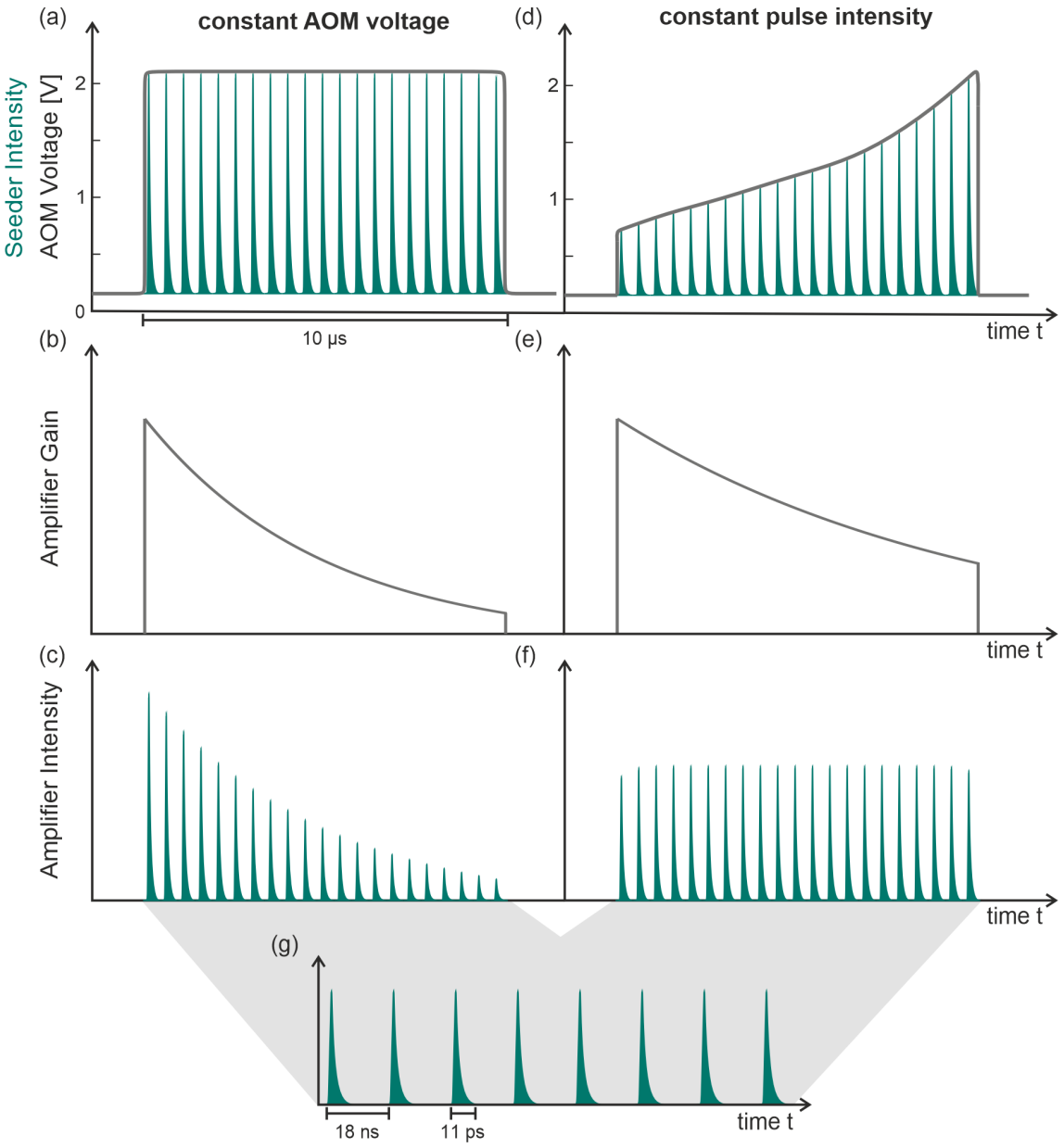

Figure 4.6. *Macropulse shape generation of burst laser output.* (a)-(c) Pulse generation with an AOM switching between min and max and (d)-(f) pulse shape of an AOM driven with a voltage curve increasing over time. This procedure has the advantage of equal intensity distribution thoughout the whole macropulse. The 10 Hz macropulse is periodically repeated after 100 ms and has a length of 10 µs containing a (g) 55 MHz micropulse structure. Each micropulse has a length of $\approx$ 11 ps with a duty cycle of 18 ns.

operation at 55.5 MHz is achieved. Between the synchronized laser pulses, there may be a time difference up to 18 ns, which has to be compensated for experimental use. A first rough temporal overlap is achieved by using an electronic phase shifter on the FO signal to vary its phase and therefore shift the pulses in time. How this is achieved experimentally and a description of the fine tuning of the temporal overlap will be subject of the following section.

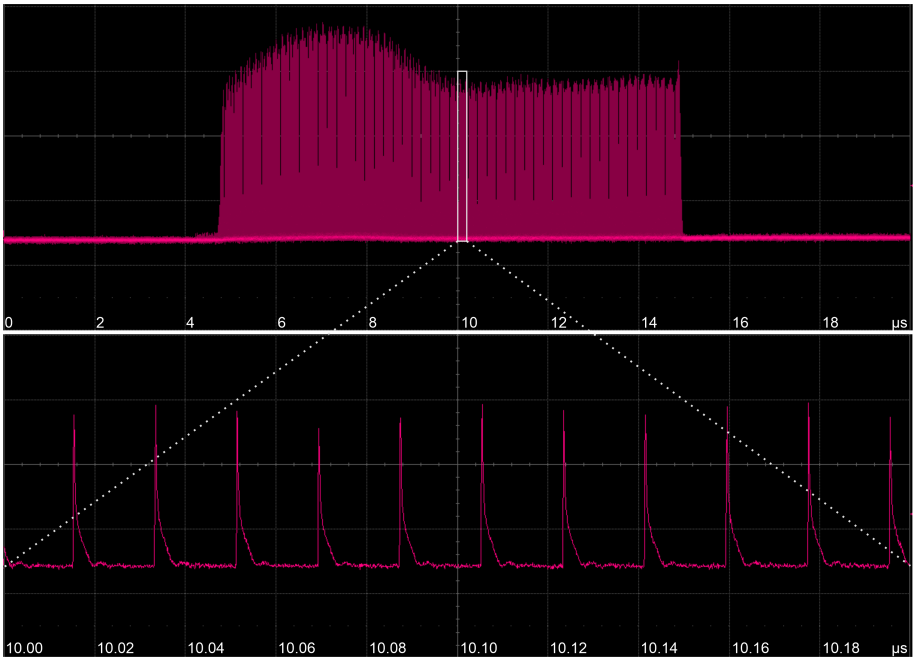

Figure 4.7. *Oscilloscope images of the IR macropulse and micropulses.* Top: IR macropulse of the Burst laser with a pulse length of 10 µs and 10 Hz repetition rate. Bottom: Zoom into the micropulse structure within one macropulse with a pulse length of 11 ps and 55.5 MHz repetition rate.

4.3 Experimental setup

After successful synchronization of the two laser pulse trains with respect to each other, they are guided to the experimental setup. First, overlap in time of the FEL and the near-IR table-top laser with picosecond precision has to be reached using the timing tool. After that, the actual experiment takes place in the SFG microscope using the visible output of the table-top laser. A full overview of the table-top laser setup, the timing tool and the SFG microscope is depicted in Fig. 4.8.

4.3.1 Temporal overlap

The timing tool setup is used to provide overlap of the two laser pulses not only in space but also in time. It was built by Riko Kiessling as part of his PhD thesis [117] where it was also used for FEL characterization measurements. To achieve temporal overlap, a rough alignment is reached by shifting the Burst timing, followed by fine-tuning based on SFG signal, as explained in the following. First, both lasers are focused on a detector (*VIGO PEM-10.6-2x2*) to display the micropulses on an oscilloscope. The FEL IR beam is focused using an off-axis parabolic mirror while the table-top near-IR beam is focused by a lens. The timing of the Burst laser can be shifted electronically with respect to the FEL to obtain a first rough temporal overlap. The accuracy here is about ±0.5 ns. The detector is reached via a flip-in mirror in the beampath (indicated by dashed lines in Fig. 4.8), without which the

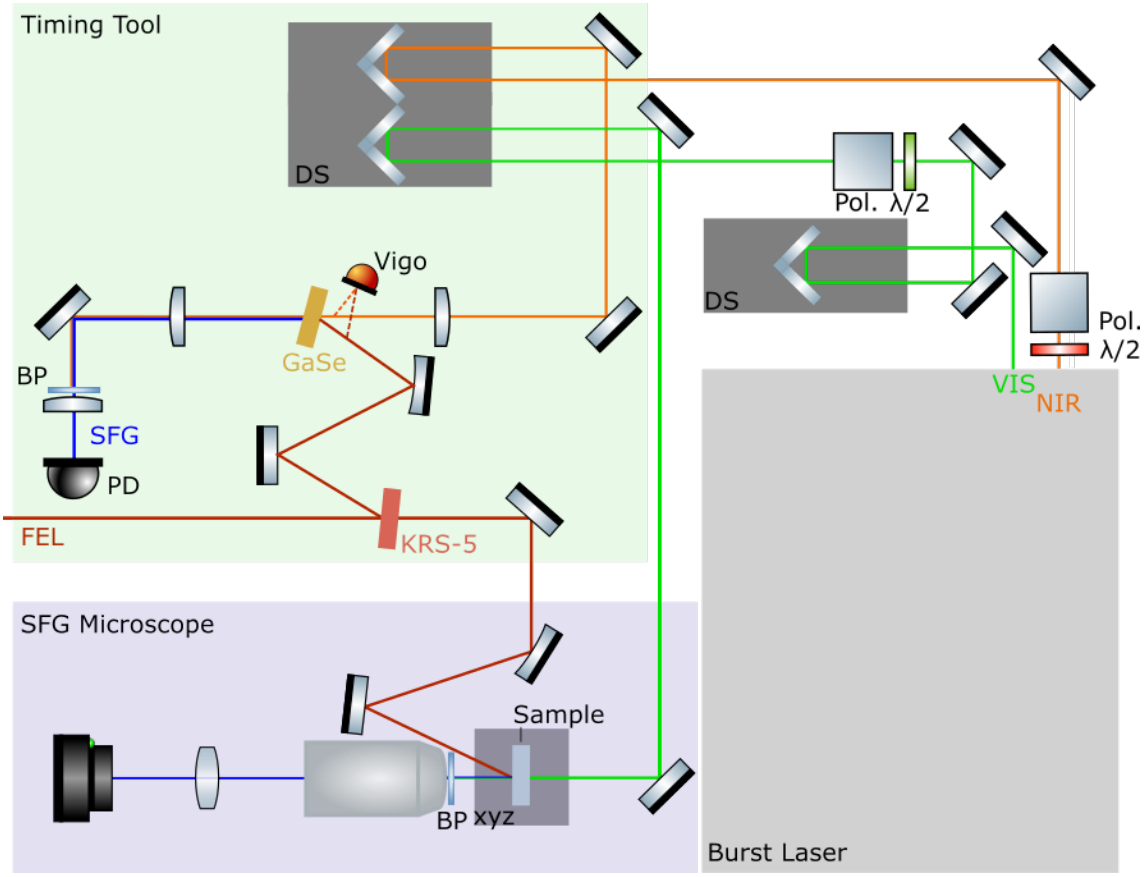

Figure 4.8. *Setup of the experiment.* The setup consists of the burst laser with attenuation by a combination of a waveplate and a polarization beam splitter, the timing tool (green background) and the SFG microscope (violet background). PD = photo diode, DS = delay stage, BP = band-pass filter, $\lambda/2 = \lambda/2$ waveplate, Pol. = polarizer, xyz = combination of three linear stages for 3D sample positioning. SFG microscope as in [P1]. Symbols for optical components partially adapted from Ref. [132].

beams are guided to a phase-matched GaSe crystal [117]. As shown in Fig. 4.8, the table-top near-IR beam path uses a delay stage to shorten or lengthen the beam path within a range of 1 ns. To finely tune the temporal overlap, a scan over the whole range of the delay stage is performed. At the right stage position, a photodiode behind the GaSe crystal detects an SFG signal generated in the crystal which is largest for overlapping pulses.

In the microscope, temporal overlap between the IR-FEL and the visible output of the table-top laser is required to generate SFG signal. To benefit from the timing tool information, the table-top near-IR and visible beam paths are required to have the same pathlengths from the outcoupling point of the table-top laser to the GaSe crystal in the timing tool and to the sample in the SFG microscope, respectively. In order to achieve this, a second delay stage is used for the visible beam path to synchronize with the near-IR beam path. Similar to the timing tool, the optimal stage position is found by scanning over the whole range of the delay stage. At temporal overlap between IR-FEL and VIS, SFG signal is generated on the sample

surface and can be detected with the SFG microscope. Once the best stage position is found, it can remain in this setting and needs only to be finely adjusted before a measurement. In addition, the visible laser is also guided through the same delay stage as the near-IR laser, to avoid temporal detuning when finding time zero with the GaSe crystal, see Fig. 4.8.

4.3.2 SFG microscope

The microscope setup brings together the IR-FEL and the visible output of the table-top laser. The two laser beams are combined on the sample surface to create the SFG signal which will be collected and detected by the microscope.

During the setup of the microscope, two different configurations have been implemented with different functionality and performance. A first configuration was implemented using reflection illumination, but had the drawback of lacking simple alignment, and causing optical damage to the objective. A second configuration was then implemented using back illumination, which is working very well in comparison to the reflection-illumination setup and is now used as the technique of the current setup. For the sake of completeness, both configurations will be discussed below. For better comparison, Fig. 4.9 shows both setups as was already done in Sec. 3.3.2, Fig. 3.6.

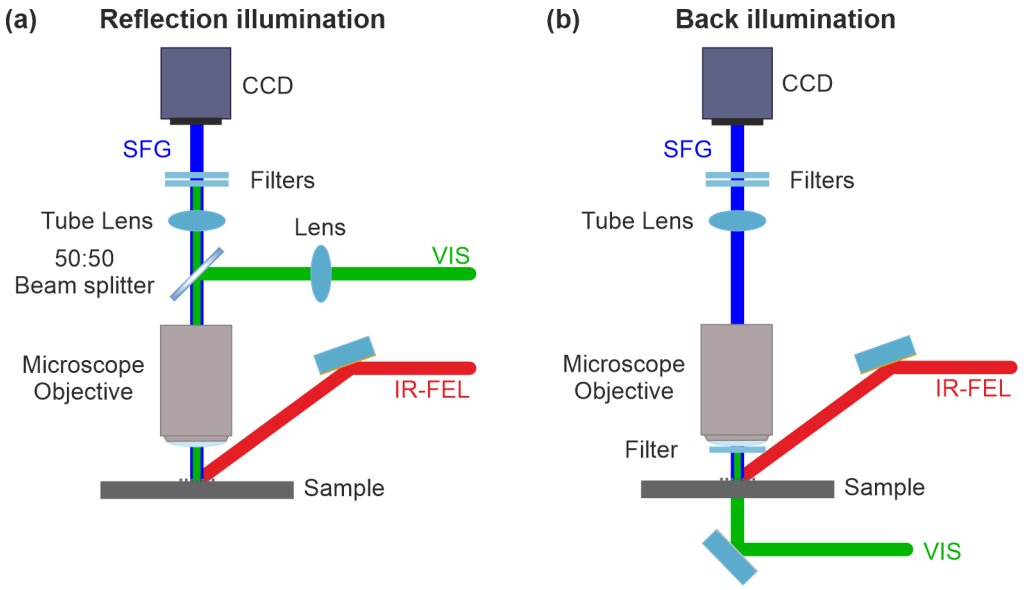

Figure 4.9. *Microscope setups.* SFG microscope setups in reflection (a) and back-illumination (b) configuration. The figures are similar to Fig. 3.6 and shown again for easier following of the discussion.

The two setups vary in the way the VIS is guided to the sample, but the main components of the SFG microscope are equal for both. In general, the microscope consists of an objective, a tube lens, a camera and filters. As depicted, the IR illuminates the sample under oblique incidence with an incidence angle of 50° with respect to the

surface normal. IR excitation under normal incidence is not possible since neither the objective nor the sample are transparent for the IR. However, oblique incidence is beneficial for the accessibility of more $\chi^{(2)}$ components, see Sec. 3.2.2. To be able to shine in the IR-FEL under 50°, a long working distance objective (*Mitutoyo M Plan Apo 50x, NA = 0.55*) with a specified working distance of $d_w = 13\,\text{mm}$ is used. The SFG signal generated on the sample surface is imaged with the objective and a 200 mm tube lens[4] onto a highly sensitive, electron-multiplied CCD camera (*PI-MAX 4, Teledyne Princeton Instruments*). To only detect SFG light with the camera, bandpass filters (*tunable bandpass 547/15, Semrock*) are used to block the upconversion laser beam. Additionally, the camera is gated to the macropulse timing to only detect photons when there is FEL light. Every image is generated by averaging the SFG signal of 100 FEL macropulses, corresponding to an acquisition time of 10 s per image.

Reflection Illumination

In the reflection-illumination setup, the visible upconverting beam is guided through the objective towards the sample. This is realized by a 50:50 beam splitter in the microscope beam path between the objective and the tube lens for incoupling of the visible laser. The VIS was focused by a 100 mm lens to the back focal plane of the objective to prevent a hard focus on the sample by the objective but instead illuminate the whole FoV. With both lasers overlapped in time and space, the SF signal is generated and guided through the objective and tube lens onto the CCD camera.
While this technique owns the great advantage of possible measurements on opaque samples due to the front illumination, it also carries two major disadvantages. First, the process of alignment in this configuration is hard to implement. Due to the VIS going through several optics and the additional beamsplitter, the required optical alignment is much more difficult to achieve than in other configurations. Visible beam reflections from the optics' surfaces cause the detection of multiple images randomly stacked upon each other with slightly different focus positions for each. A perfectly aligned image barely gets rid of these sub-images but combines all these in one place (Fig. 4.10(a)). In this case, the main image's focus position acts as the major focus but is blurred out by the underlying images not in the correct focal plane. Second, the microscope's objective was damaged by the VIS laser beam. This is attributed to an intermediate focal point of the VIS inside the objective, induced by the several optical components inside the objective. The tight focus led to a burn spot on one of the objective elements. The burn spot caused a large area of the field of view to be fully covered by scattered light, see Fig. 4.10(b).

These problems led to the decision to change the microscope setup to a back-illumination configuration. By this, a simpler alignment process of the visible laser

[4] As mentioned in Sec. 3.1.1, Eq. (3.1.1), the magnification provided by the objective can only be reached in combination with a specific tube lens, here $f = 200\,nm$.

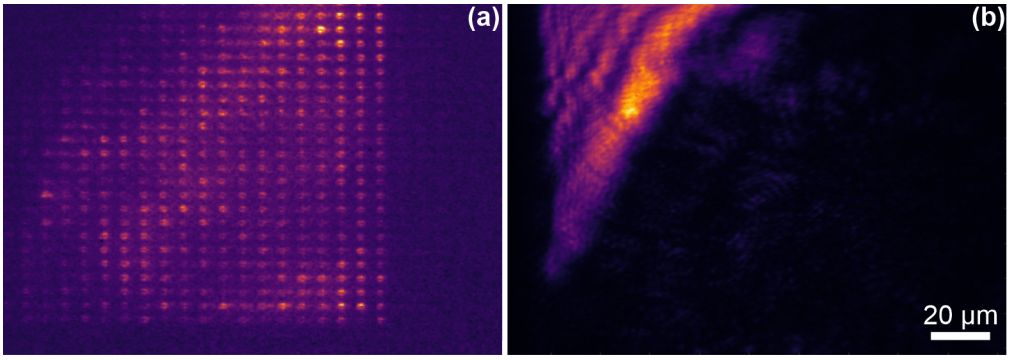

Figure 4.10. *Microscope images using reflection illumination.* a) Image of a microresonator array in focus position. b) Scattering light from a burn spot inside the objective.

is achieved as it is not necessary to guide it through all the imaging optics of the microscope. Additionally, the VIS can be blocked from entering the objective by an additional filter preventing laser induced damage in the objective.

Back Illumination

The back illumination setup is the final version of the SFG microscope used for the experiments described in this thesis [P1]. While the illumination by the FEL is unchanged, the VIS illuminates the sample from the backside under normal incidence. With this change in the setup, both problems with the reflection illumination setup can be eliminated. However, to prevent damage in the objective, the VIS has to be kept from entering the objective. Thus, an additional bandpass filter (*single-band bandpass 500/24, Semrock*) between sample and objective was installed. The filter may cause additional reflections of the upconverting light leading to temporally shifted side peaks of the SFG signal. Thus, care must be taken when evaluating time-dependent SFG signals. In comparison to the reflection illumination geometry, these additional reflections are a minor problem since they are generated by only one filter instead of a whole set of optical components inside the microscope.

The microscope enables the imaging of a field of view (FoV) of approx. 275 µm × 275 µm. Both lasers illuminate the whole FoV. The IR-FEL is mildly focused and has a beam diameter of approx. 500 µm on the sample surface. The VIS has a beam diameter of roughly 9 mm at the sample position, leading to a significant amount of scattered light. The amount of scattered light could be reduced by focusing. However, it was decided to not focus the VIS to maintain the flat-top beam profile for homogeneous illumination of the FoV. The scattered light is blocked by the filter and additional black aluminum foil around the whole microscope setup.

5

Infrared Super-Resolution Wide-Field Microscopy using Sum-Frequency Generation

This chapter discusses the first experiments with the home-built sum-frequency generation microscope. In Sec. 5.1, the spatial resolution of the microscope is derived and possible error sources are discussed. In addition, sub-diffractional imaging of localized modes is introduced. Sec. 5.2 introduces the term spectro-microscopy and shows various examples of using this technique.

Parts of this chapter have been published in Ref. [P1].

5.1 High-resolution SFG microscopy of localized surface phonon polaritons

By frequency mixing two laser beams with drastically different wavelengths, the SFG microscope developed during this thesis offers a resolution below the diffraction limit of the resonant IR wavelength. This difference in resolution to the diffraction limit becomes larger, the shorter the upconversion wavelength is chosen. But even for two near-degenerate beams, the detected wavelength is a factor two smaller than the imaging wavelength. In the specific case of the microscope discussed here, the wavelength of the upconversion beam is roughly twenty times smaller than the resonant wavelength.

5.1.1 IR sub-diffractional resolution

The first step was to determine the microscope's spatial resolution. To do so, a sample of 4H-SiC micropillar (MP) arrays on a 4H-SiC substrate was used (in the following referred to as SiC sparse sample). SiC was chosen as an advantageous test material due to several reasons: SiC inherently has a broken inversion symmetry, thus SFG signal can be created not only at the surface but also in the bulk. It shows sharp spectral resonances, and a small phonon damping. In combination with the fabrication of microresonators, localized SPhPs are supported, leading to a large field enhancement and thus enhanced SFG signal [56, 69, 133]. By fabricating resonators at the size of the expected resolution, the sample is ideal to test the microscope and

determine its spatial resolution.
The MP[5] were fabricated into the sample by a standard electron-beam lithography (EBL) process [P1]. All arrays were designed with a period of $p = 5\,\mu m$ and a height of $h = 1\,\mu m$, with two different diameters of $d = 1$ and $2\,\mu m$. The actual diameters and periods of the fabricated sample were measured using scanning electron microscopy (SEM), see Fig. 5.1 for an SEM image of the sample.
As shown in the SEM image in Fig. 5.1(a), different array sizes were fabricated ranging from 1 MP to a 10×10 MPs array. As a result of the fabrication process, the pillars are wider at the bottom than on the top. Thus, the dedicated $d = 1\,\mu m$ pillars' diameters are in the range of $0.9\,\mu m \lesssim d_1 \lesssim 1.1\,\mu m$ (b) and the $d = 2\,\mu m$ pillars have diameters of $1.9\,\mu m \lesssim d_2 \lesssim 2.1\,\mu m$ (c). The actual period of the pillars is about 4.5 µm.

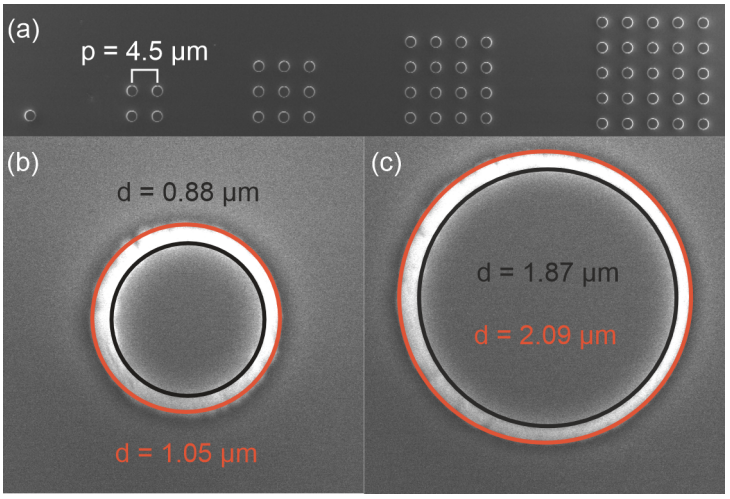

Figure 5.1. *SEM images of micropillar arrays.* (a) Example arrays from 1 MP to 5×5 MPs with a period $p = 4.5\,\mu m$. (b) Single MP with $0.88\,\mu m < d_1 < 1.05\,\mu m$, fabricated with $d_{1,\text{design}} = 1\,\mu m$. (c) Single resonator with $1.87\,\mu m < d_2 < 2.09\,\mu m$, fabricated with $d_{2,\text{design}} = 2\,\mu m$. All MPs have a height of $h = 1\,\mu m$.

For the derivation of the spatial resolution, images of the monopole resonances (see Sec. 2.3) of the individual micropillars with $d \approx 1\,\mu m$ are analyzed, a representative SFG image is shown in Fig. 5.2(a). In this image, all micropillars appear nicely resolved individually, so that line profiles through the pillar rows and columns of the arrays can be examined, Fig. 5.2(b,c). Each line profile was fit with a double error function

$$I_{SFG}(x) = \sum_{i=1}^{n} a_i \cdot \left[erf\left(\frac{x + \mu_i + c_i}{\sigma_i \cdot \sqrt{2}}\right) \cdot erf\left(\frac{x + \mu_i - c_i}{\sigma_i \cdot \sqrt{2}}\right) + 1 \right] + b, \qquad (5.1.1)$$

where a_i is the amplitude, b is a vertical offset and c_i are the half widths for each

[5] All SiC resonator samples discussed within this thesis were fabricated by collaborators at Vanderbilt University.

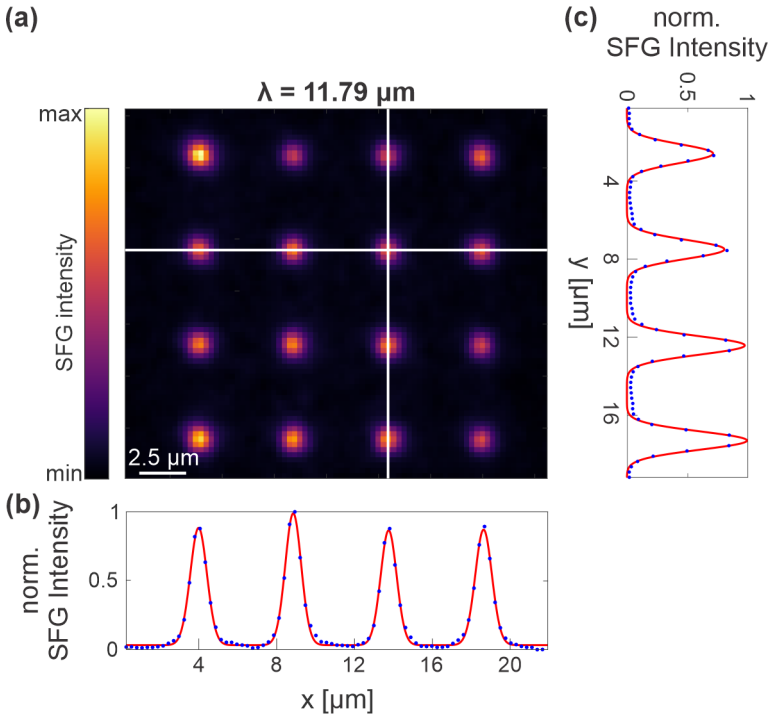

Figure 5.2. *SFG microscopy of SiC MPs.* (a) SFG microscope image of a 4x4 MP array ($d \approx 1$ µm) recorded at the IR wavelength of the monopole resonance. (b,c) Double error function fits to the micropillar line profiles in horizontal and vertical direction indicated by white lines in (a). The blue dots show the data, the red solid line is the fit curve. Reprinted from [P1].

MP. The parameters μ_i are the center positions of the pillars and σ_i the corresponding broadening parameters. n is the number of pillars in one row or column. All parameters are illustrated in Fig. 5.3 for clarification.

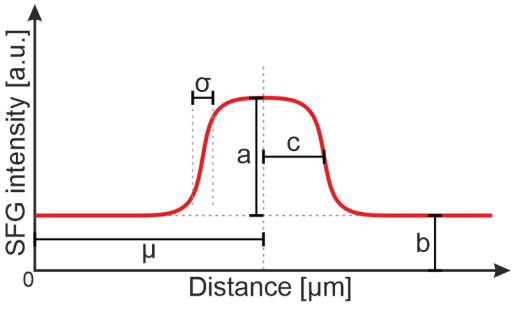

Figure 5.3. *Illustration of the parameters in the fit function.* The red line illustrates a double error function fit with the parameters for the amplitude a, the vertical offset b, the half width c, the center position μ and the broadening σ.

Using the broadening σ_i, the microscope's spatial resolution R_i is calculated according to $R_i = 2.9 \cdot \sigma_i$. The factor 2.9 has its origin in the Gaussian approximation of the paraxial point-spread function, also referred to as Airy disk[6] [134, 135]. In total, 285 micropillars were imaged leading to 285 values for σ, which were examined for horizontal and vertical resolution, respectively. In Fig. 5.4, these values are plotted

[6] A detailed derivation of the relationship between the Airy radius and the Gaussian standard deviation can be found in Ref. [134].

in a histogram, where it is nicely visible that they resemble a Gaussian distribution. The red line represents a Gaussian fit over the data whose center position gives the spatial resolution of $(1.35 \pm 0.13)\,\mu m$ in the horizontal and $(1.39 \pm 0.13)\,\mu m$ in the vertical direction.

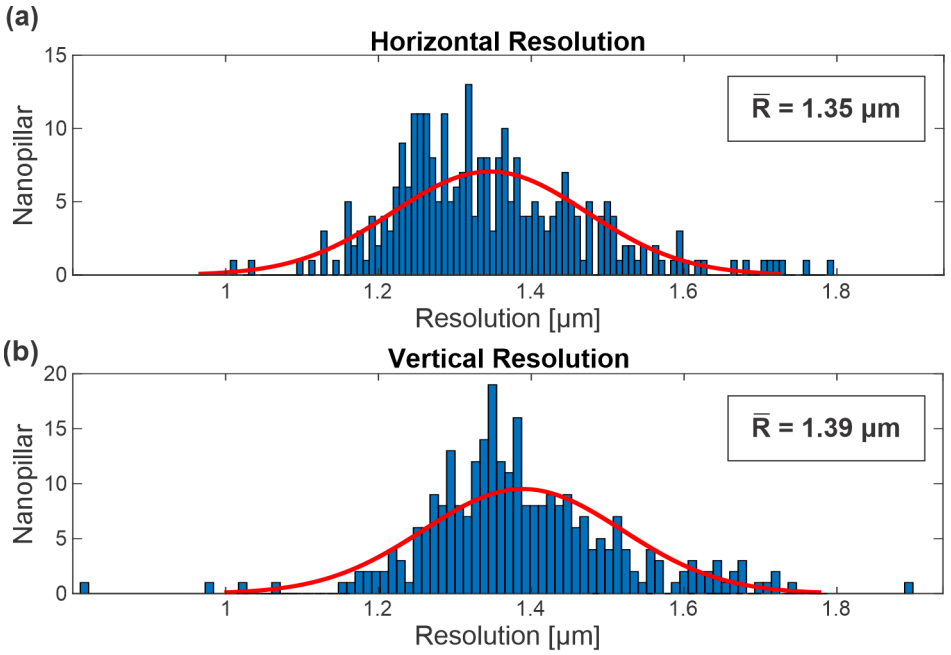

Figure 5.4. *Histogram plots for horizontal and vertical resolution.* Histogram plots for the horizontal (a) and vertical (b) spatial resolution, respectively. The red line indicates a fit of a Gaussian distribution. The mean horizontal resolution is $\overline{R}_{\mathrm{hor}} = 1.35\,\mu m$ and the mean vertical resolution is $\overline{R}_{\mathrm{ver}} = 1.39\,\mu m$. Reprinted from [P1].

The Abbe limit for an imaging wavelength of $10 - 12\,\mu m$ for an equivalent IR microscope is $R_{\mathrm{Abbe}} \approx 10\,\mu m$, according to Eq. (3.1.3). As derived here, the SFG microscope offers a resolution of $R = 1.4\,\mu m$ which is comparable to $\lambda_{\mathrm{IR}}/9$, thus providing a microscope with deeply sub-diffractional resolution for the mid- to far-infrared regime. With shifting the IR-FEL wavelength further into the infrared after complete integration of the far-IR upgrade in the FEL setup, the resolution could in principle reach $\lambda_{\mathrm{IR}}/100$. However, the need for spectral separability of SFG and VIS beams by a longpass filter in front of the objective will set a long-wavelength limit in the current microscope setup. For the current FEL operating out to $50\,\mu m$, the maximum expected relative resolution is $\approx \lambda_{\mathrm{IR}}/35$.

Resolution-limiting factors

According to Eq. (3.1.3), with an SFG wavelength of $\lambda_{\mathrm{SFG}} = 500\,nm$, the maximum possible resolution can be calculated to be $R_{\mathrm{Abbe}}\,(500\,nm) \approx 455\,nm$, which is roughly one-third of the measured microscope's resolution. This difference can be explained by the following possible limiting factors:

- As visualized in Fig. 5.4, the achieved resolution calculated from multiple pil-

lars is comparatively broad. The resolutions have been extracted from images of the MP patches which have not all been recorded during the same scan. The field of view (FoV) does not allow to image all patches at the same time, but only a smaller group of patches. Before every scan for which the sample was moved, the **focus position** was adjusted, whose accuracy strongly depends on visual judgment. Therefore it is highly likely that the focus positions of the individual pillars were not entirely optimal for every image.

- The micropillars have a height of 1 µm, with varying diameters of ≈ 0.9 µm to ≈ 1.1 µm, as shown in Fig. 5.1(b). Thus, the volume of the monopolar mode detected in the process of determining the spatial resolution changes over the pillar height. Due to this trapezoidal shape there might be a blurring of the signal, corresponding to the **depth of field**.

- With the SFG microscope, not the MPs themselves, but rather the nonlinear SPhP's nonlinear signal inside them is imaged. The mode volume of the localized SPhPs is finite and on the order of the size of the MPs. Therefore, the extracted value represents a **convolution between the spatial extent of the mode and the resolution** of the microscope.

- **Mechanical noise** on the optics in the microscope and the sample mount cannot be excluded. Shaking of the sample out of the focal plane or vibrations on optics leading to blurry images thus may have an effect on the achieved spatial resolution.

Hence, the measured resolution of $R \approx 1.4$ µm is an upper limit of the microscope's spatial resolution.

5.1.2 Sub-diffractional imaging of monopole and dipole mode

Turning to samples of MPs with diameters of $d \approx 2$ µm, see Fig. 5.1(c), the spatial resolution is smaller than the physical size of the micropillars. This, it is possible to study the mode profiles of the localized SPhP modes introduced in Sec. 2.3. In Fig. 5.5(a,b), SFG images at two different IR wavelengths are shown. The images were taken at the exact same sample position, and show a line of four MPs with diameters of 2 µm. The white circles indicate the physical pillar size. In Fig. 5.5(a) a single peak of SFG intensity for each MP can be observed, while in Fig. 5.5(b) two peaks are resolved. The different behavior is represented in the line profiles, Fig. 5.5(c), corresponding to the white lines in Fig. 5.5(a,b). From these highly resolved images, the IR resonances in Fig. 5.5(a,b) can clearly be assigned to the monopole and dipole mode, respectively [56]. The images are in good agreement with simulations of the electric field distribution of SPhPs in SiC MPs, see Fig. 5.5(d), showing that the monopole mode has the largest field intensity on the top of the

micropillars while it occurs at the sides of the MP for the dipole mode [44, 59].

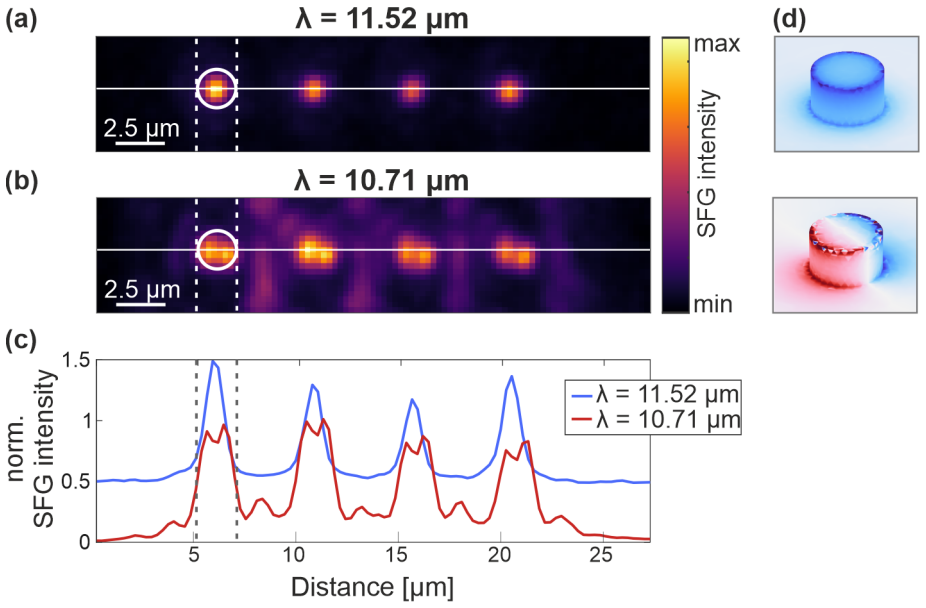

Figure 5.5. *Observation of monopole and dipole modes of SiC micropillars.* SFG images of micropillars resonant with the (a) monopole and (b) dipole mode. The physical pillar size is indicated by the white circle. (c) Line cuts along the white lines in (a) and (b) are plotted, showing the ability to resolve the structured electric fields of the dipole mode on top of the micropillar in comparison to the monopole mode. Reprinted from [P1]. (d) Simulation of monopole (top) and dipole (bottom) mode electric fields. Reprinted from [P3].

5.2 Spectro-microscopy

The SFG microscope is able to resolve individual microstructures on samples with IR sub-diffractional spatial resolution. The microscopy technique itself as well as the spatial resolution have a variety of advantages, which will be discussed in the following section.

The information coming from microscopy is captured in the images. By changing the FEL wavelength, the image changes accordingly, and a short video clip shows the transformation during a wavelength scan. The big advantage here are the innumerable features which can be found in only one image, while the disadvantage certainly is the purely visual information lacking certain values for comparison. In spectroscopy, it is the other way round. A spectrum represents all the properties of the measured region but it does not contain spatial information that allows for a comparison between different sample positions.
Data analysis of a series of microscopic images provides the opportunity for both microscopic images as raw data and spectra from wavelength scans of the FEL. By integrating over a whole image, all information can be transformed into one total SFG intensity value. Using this procedure for every image of an IR wavelength scan, a spectrum can be generated. Hence, the technique offers not only microscopic but

also spectroscopic insight of the sample, thus offering spectro-microscopy. As will be discussed in a later paragraph, this technique can be used not only by averaging over the whole image, but also to extract a spectrum for specific regions of interest, such as individual subdiffractional microstructures.

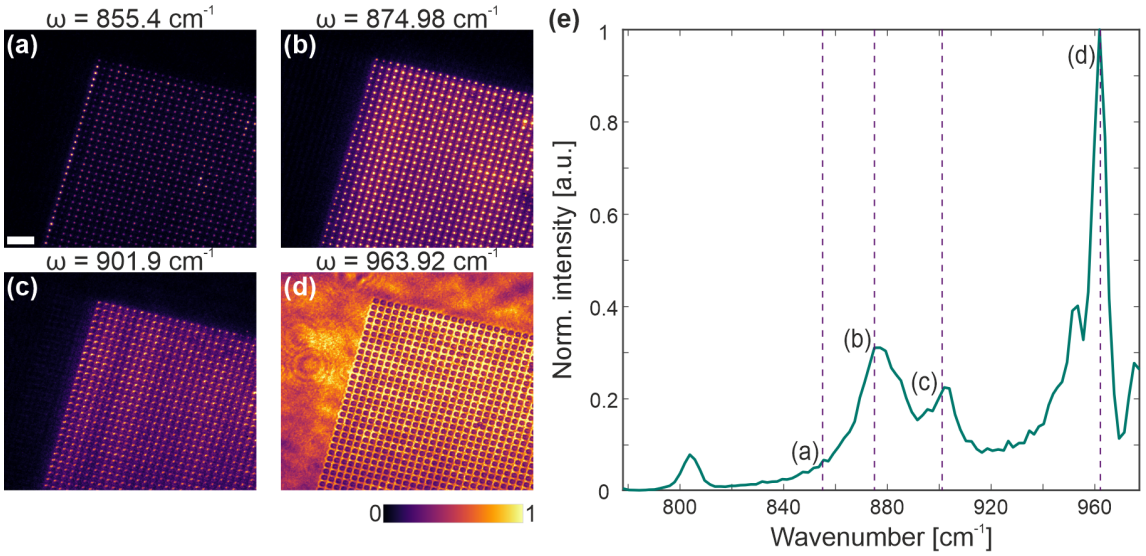

Figure 5.6. *Spectro-Microscopy.* (a-d) SFG images of the upper left corner of a 1x1 mm^2 4H-SiC micropillar patch and (e) the corresponding spectrum obtained by integrating the intensity of each image. The images (a-d) show data with different frequency-dependent behavior containing spatial information which is not apparent in the spectrum. The scale bar in (a) has a length of 30 µm.

An example of a wavenumber scan for SiC MP patches is shown in Fig. 5.6. The images (a) to (d) show the SFG intensity generated on the sample surface for different wavenumbers taken from one spectral scan of the FEL. In (e), the spectrum of the whole scan area is plotted, showing several peaks. The microscope images show very different intensity distributions at the different FEL wavelengths. Images and spectrum together give comprehensive information about the optical response of the sample.

The true power of this technique is that it can be used not only to generate spectra of the whole FoV but also for selected regions, i.e., in principle down to a single pixel.

Spectral plots for individual microstructures

Because every single pillar can be resolved, due to the microscope's high spatial resolution, it is possible to obtain spectra for distinct pillars or individual areas and to further analyze their behavior in dependence of the IR wavelength. Specifically, the technique allows for the creation of a spectrum for each and every pixel, hence also for every single micropillar. An example is displayed in Fig. 5.7. Panel (a) shows an SFG image of one-dimensional (1D) chains of micropillars of increasing length, where each individual pillar can be distinguished. In Fig. 5.7(b), spectra for

three of these pillars are shown as example, indicated by the red, orange and yellow circles in (a). Obviously, the spectra of the pillars look very different, indicative of the response of each microstructure being modified by neighboring resonators. The effect of such a collective response will be discussed in detail in Chapter 7.

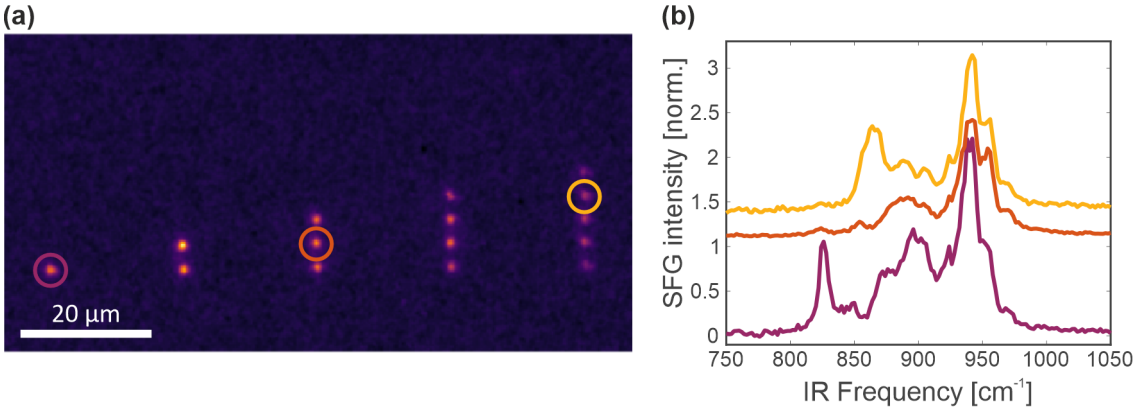

Figure 5.7. *Spectra of micropillars in 1D chains.* (a) SFG microscope image of 1D pillar chains with a length of one to five micropillars. (b) Spectral plots over the whole SiC Reststrahlen band for three selected pillars of different chains in (a), see red, orange and yellow circles.

Not only the response of individual pillars can be converted into frequency spectra, but additionally distinct regions of the sample, as shown in Fig. 5.8. The image in (a) shows the SFG intensity signal for a 10×10 MP patch at $\omega_{\mathrm{IR}} = 906\,\mathrm{cm}^{-1}$, where the blue rectangle indicates the area which was integrated to extract a spectrum shown in (b). The blue spectrum shows peaks for the monopole ($\omega_{\mathrm{M}} \approx 840\,\mathrm{cm}^{-1}$) and dipole modes ($\omega_{\mathrm{TD1}} \approx 906\,\mathrm{cm}^{-1}$ and $\omega_{\mathrm{TD2}} \approx 945\,\mathrm{cm}^{-1}$), as well as the LO peak ($\omega_{\mathrm{LO}} \approx 964\,\mathrm{cm}^{-1}$), as expected. Additionally, the spectrum shows a small shoulder at $\omega_{\mathrm{IR}} \approx 830\,\mathrm{cm}^{-1}$, that is slightly redshifted from the monopolar mode, which cannot be assigned to one of the resonances mentioned before. Figure 5.8(c) shows the same MP patch at a different FEL frequency, $\omega_{\mathrm{IR}} = 830\,\mathrm{cm}^{-1}$, where the dominant signal occurs at the pillar column on the left-hand edge of the MP patch. The corresponding spectrum shows a clear peak for the edge column in contrast to the shoulder observed in the spectrum for the whole pillar patch. Therefore, the analysis method and the high spatial resolution are very beneficial for further studies of nanophotonic modes in this context. The appearance of such an edge feature will be visited again in Chapter 8.

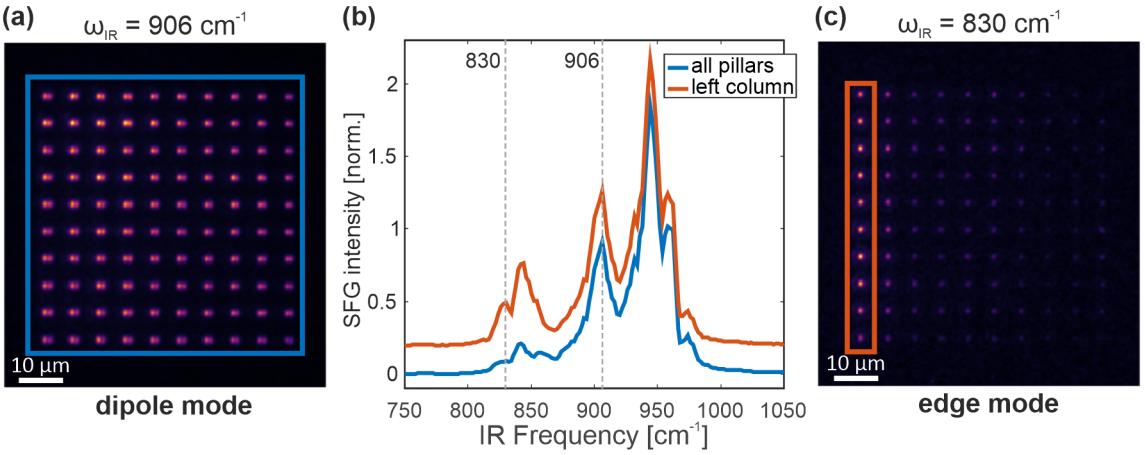

Figure 5.8. *SFG spectro-microscopy of selected sample areas.* (a,c) SFG Microscope images of the same 10x10 MP patch for different IR frequencies, chosen to match a dipole mode and an edge mode, respectively. (b) Spectra of the whole pillar patch (blue) and only the left edge pillars (orange).

6

Observation of Propagating Phonon Polaritons with SFG Microscopy

After the first brief discussion of localized modes in the previous chapter, the observation of propagating polaritons with SFG microscopy will be introduced here. Sec. 6.1 gives an overview of current methods used to detect propagating waves along surfaces and motivates the use of an SFG microscope for detection and imaging. In Sec. 6.2, the underlying theory is discussed and it is clarified why the observation of propagating polaritons is possible with the SFG wide-field microscope. The experimental results achieved for AlN are discussed in Sec. 6.3 as well as the influence of the laser polarizations. Last, Sec. 6.4 touches future experimental questions.

6.1 Motivation

In the previous chapter, the detection of localized modes within micropillar arrays was discussed. The detection of propagating polaritons is also a common procedure, e.g., in tip-based microscopy like s-SNOM [136, 137] or by spectroscopic approaches like prism coupling [46, 138, 139]. Knowledge about and thus resulting controllability of propagating surface polaritons opens the door for a variety of nanophotonic devices [16, 17].

Near-field techniques like s-SNOM are an established tool to examine propagating waves with high spatial resolution and thereby offering sub-diffractional information [136, 140]. In combination with a tunable laser, not only spatial, but also spectral information can be provided. However, s-SNOM requires raster-scanning a nanotip across a sample area of interest leading to long acquisition times. Therefore, typically only a few selected frequencies are chosen for imaging. Also, the metallic nanotip in close proximity to the sample may lead to perturbations of the polaritonic response [20].
In constrast, far-field techniques such as prism coupling or thermal emission spectroscopy [62, 63] provide full spectral information. In these techniques, however, the information of the sample is spatially averaged over a large IR spot size, and thus requires spatially homogeneous samples.

In this chapter, it will be shown that SFG microscopy can be used as a far-field technique to detect propagating polaritons. Far-field optical microscopy avoids any tip influences and can detect the propagating wave by interferometric imaging, as will

be explained shortly. In contrast to spectroscopic far-field approaches, it maintains the spectral information of each image pixel. Additionally, the acquisition times for image recording is reduced significantly, due to the wide-field imaging instead of scanning-laser approaches. At first glance, the replacement of tip-based scanning techniques by far-field detection might lead to a loss in spatial resolution. The wide-field SFG microscope introduced here brings together the far-field detection with maintaining high spatial resolution due to frequency mixing. Thus, this technique promises both high spatial resolution, due to the SFG microscopy technique, and highly resolved spectral information, from the tunable IR-FEL.

However, it is not directly obvious why the SFG microscope, as an intensity-based technique, would provide polariton phase information associated with their propagation. Therefore, the underlying theory will be further discussed in the following.

6.2 Theory

The electric field of a wave propagating along the x direction on the sample surface can be expressed by

$$E_1(x,t) = A_1 e^{i(\omega t - k_1 x)} \tag{6.2.1}$$

with the amplitude A_1, propagating with a frequency ω and a wavevector k_1. Damping of the propagating waves will be neglected in this discussion. As discussed in detail in Sec. 3.2.2, the SFG microscope detects sum-frequency intensity, $I = |E|^2$. Although the electric field of a propagating wave is changing with time and location, the field intensity stays constant, $I_1 = A_1^2$. Therefore, microscope images taken of this propagating wave only result in a constant signal with no detectable wave pattern, see Fig. 6.1(a). Here, the gray line shows the propagating wave in terms of the real part of a complex electric field amplitude as a function of the location x and the green line shows its intensity. The density plot on top of Fig. 6.1(a) gives an impression of the image that would be detected with the microscope in the case of a propagating wave following Eq. (6.2.1).

If a second wave is taken into consideration, with a similar form as in Eq. (6.2.1), i.e., with the same frequency ω and a different wavevector, e.g., $k_2 = -0.5k_1$ leading to

$$E_2(x,t) = A_2 e^{i(\omega t + 0.5 k_2 x)}, \tag{6.2.2}$$

the total electric field amplitude is described by $E_{tot} = E_1 + E_2$. In Fig. 6.1(b), such a case is considered. Next to the wave plotted above for E_1 (gray), the second propagating wave E_2 is depicted as a black line. As can be seen in the plot, the

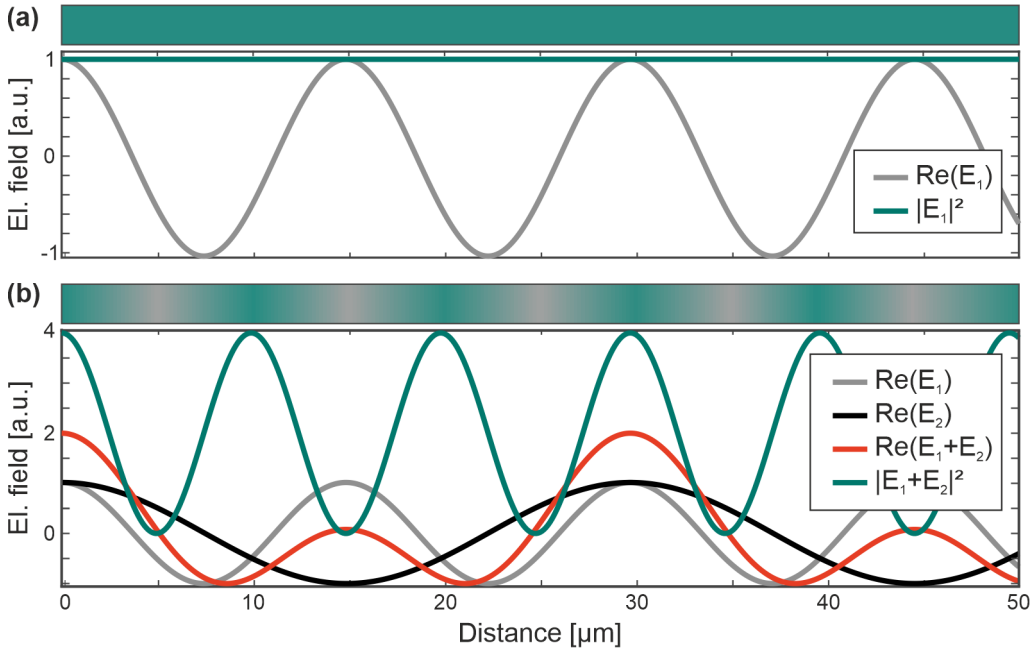

Figure 6.1. *Observation of propagating waves through spatial interference.* (a) The spatially varying electric field amplitude of a single propagating wave (gray) has a constant field intensity (green), showing no characteristics of a propagating wave in a microscopic image. The sketch above the plot mimics a corresponding microscopic image. (b) The addition of a second propagating wave (black) leads to a modulated total electric field (red), where the subsequent absolute value of both fields leads to a standing wave pattern, observable in a microscope.

total electric field (red line) still strongly varies over x, but in contrast to the single wave cases the intensity of the total wave is no longer a constant but $|E_{\mathrm{tot}}|^2 = |A_1 + A_2|^2 \cos^2(1.5kx)$. The corresponding plot is shown in green, where a clear standing wave behavior is visible and the shaded area illustrates the wave pattern with maxima and minima as expected in an SFG image.

This shows that the interference of two waves of different momenta are needed to image a propagating wave. In the case of the SFG microscope, the propagating SPhPs ($E_{\mathrm{P}} = A_{\mathrm{P}} e^{i(k_{\mathrm{P}}x - \omega_{\mathrm{P}}t)}$) interfere with the incoming IR-FEL beam ($E_{\mathrm{pt}} = A_{\mathrm{pt}} e^{i(k_{\mathrm{pt}}x - \omega_{\mathrm{pt}}t)}$). Since k_{pt} is simply determined by the experimental geometry, information about the propagating surface wave can be extracted from the interference pattern.

For the propagating SPhPs, damping needs to be considered. These propagation losses can be included using a complex-valued wavevector

$$k_{\mathrm{P}} = \Re(k_{\mathrm{P}}) + i\Im(k_{\mathrm{P}}) = \frac{2\pi}{\lambda_{\mathrm{P}}} + i\gamma_{\mathrm{P}}, \tag{6.2.3}$$

with the polariton wavelength λ_{P} and the damping constant γ_{P}. Thus, the real part of the wavevector gives rise to the periodicity of the wave and the imaginary part contains the information about the damping.

All the plots above are for the time $t = 0$, but as stated in Eqs. (6.2.1) and (6.2.2)

the two waves are time dependent. Both the launched propagating wave and the incoming IR wave itself are based on the same frequency ω leading to no direct time dependence according to

$$\begin{aligned} |E_{\mathrm{tot}}(x,t)|^2 &= \left|e^{i(k_{\mathrm{P}}x-\omega t)} + e^{i(k_{\mathrm{pt}}x-\omega t)}\right|^2 \\ &= \left|e^{-i\omega t}\left(e^{ik_{\mathrm{P}}x} + e^{1k_{\mathrm{pt}}x}\right)\right|^2 = \underbrace{\left|e^{-i\omega t}\right|^2}_{=1}\left|e^{ik_{\mathrm{P}}x} + e^{ik_{\mathrm{pt}}x}\right|^2 \\ &= \left|e^{ik_{\mathrm{P}}x} + e^{ik_{\mathrm{pt}}x}\right|^2. \end{aligned} \tag{6.2.4}$$

Interference is only possible due to a fixed phase relationship, as the polariton wave emerges by launching SPhPs only from one specific place. Thus, imaging of propagating waves is possible, despite the intrinsic time average of the intensity detection.

6.3 Propagating polaritons on an AlN substrate

For the experimental observation of propagating polaritons, a sample system of AlN and MoO_3 was used. Both materials have been the subject of recent studies, and show interesting properties for applications in the mid- to far-infrared regime [141, 142]. AlN has attracted broad attention, e.g., due to its applicability to second- and third-order nonlinearity [143–145], and, owing to its large bandgap, its usage as light-emitting material for UV light generation [141, 146, 147]. MoO_3 on the other hand is a van der Waals biaxial crystal which received significant attention due to its ability to support in-plane hyperbolic polaritons [148], and opened a new field of twist optics using twisted bilayers or trilayers [149, 150]. Recent studies show the possibility of chemical switching of polaritons in MoO_3 [151], in addition to the material's charge storage properties [152]. It is envisioned to show great potential in, e.g., thermal emission manipulation [153], hyperlensing and -focusing [154], or control of dipole-dipole interactions [155].
Interestingly, both materials show an in-plane anisotropic optical response leading to different characteristics of the propagating waves, according to the orientation of the sample. For anisotropic crystals, the wave equation has two different solutions for ordinary (perpendicular to the optical axis) and extraordinary (parallel to the optical axis) waves [156]. This behavior emerges from different TO and LO phonon frequencies with respect to the propagation direction. For AlN, two mostly overlapping Reststrahlen bands arise with frequencies $\omega_{\mathrm{TO},\perp(\parallel)} = 667.2\,\mathrm{cm}^{-1}$ $(608.5\,\mathrm{cm}^{-1})$ and $\omega_{\mathrm{LO},\perp(\parallel)} = 909.6\,\mathrm{cm}^{-1}$ $(888.9\,\mathrm{cm}^{-1})$ [157]. Due to the directionality of the phonon resonances, a distinction is made between the parallel and perpendicular dielectric functions [156]:

$$\begin{aligned}\varepsilon_{\perp}(\omega) &= \varepsilon_{\perp}^{\infty}\left(1+\frac{\omega_{\mathrm{LO},\perp}^2-\omega_{\mathrm{TO},\perp}^2}{\omega_{\mathrm{TO},\perp}^2-\omega^2-i\omega\gamma_{\mathrm{TO},\perp}}\right),\\ \varepsilon_{\parallel}(\omega) &= \varepsilon_{\parallel}^{\infty}\left(1+\frac{\omega_{\mathrm{LO},\parallel}^2-\omega_{\mathrm{TO},\parallel}^2}{\omega_{\mathrm{TO},\parallel}^2-\omega^2-i\omega\gamma_{\mathrm{TO},\parallel}}\right),\end{aligned} \tag{6.3.1}$$

with the corresponding high frequency dielectric constants $\varepsilon_{\perp/\parallel}^{\infty}$ and damping constants $\gamma_{\mathrm{TO},\perp/\parallel}$. $\varepsilon_{\perp}$ and $\varepsilon_{\parallel}$ are used to calculate the corresponding SPhP dispersions as will be analyzed in further detail in Sec. 6.3.1. MoO_3 is a biaxial anisotropic crystal with three Reststrahlen bands covering a broad frequency range from $\omega \approx 500-1030\,\mathrm{cm}^{-1}$ [142]. In the following, the general observation of propagating polaritons on the AlN substrate launched by MoO_3 flakes is dicussed.

To image propagating polaritons with the SFG microscope, MoO_3 flakes were placed on top of an AlN substrate (0.4 mm thick, m-cut). The MoO_3 flakes have widths in the range of $15-20\,\mu\mathrm{m}$, lengths in the range of 40-65 µm and a thickness of $\approx 200\,\mathrm{nm}$. They are observed to act as launchers for propagating polaritons on the AlN surface. Images were recorded over the AlN Reststrahlen band region. An example image for $\omega \approx 817\,\mathrm{cm}^{-1}$ is shown in Fig. 6.2(a).

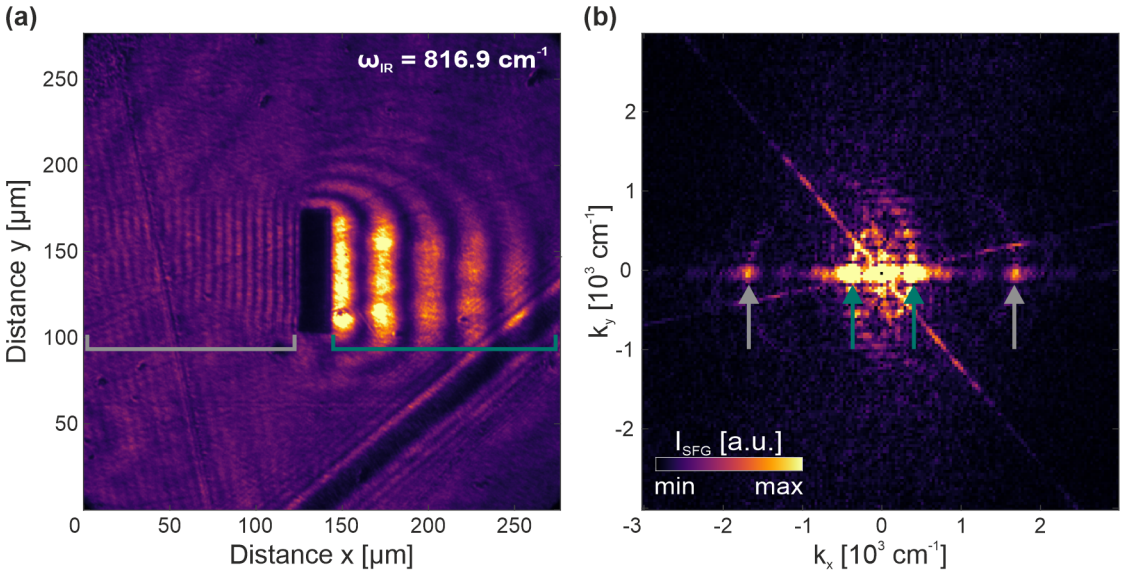

Figure 6.2. *SFG image and corresponding 2D-FFT of propagating polariton waves.* (a) SFG image of propagating polaritons on an AlN substrate launched by an MoO_3 flake (dark rectangular area). Interference patterns with different periodicities are visible on the two sides of the flake. (b) Corresponding 2D-FFT plot of (a).

As can be very well seen, propagating waves are observed on both sides of the MoO_3 launcher, with decreasing amplitude at larger distances from the launcher. The wavevectors and thus the periodicities for the forward and backward propagating waves are different, with a larger fringe spacing on the right side of the launcher and a smaller fringe spacing on the left side of the launcher. Fringes are visible over the

whole range of the FoV, i.e., more than 100 µm in both directions. Fresnel fringes coming from defects on the substrate (tilted lines in the image) are also weakly visible. In Fig. 6.2(b), the corresponding two-dimensional fast-Fourier transformation (2D-FFT) of the microscope image is shown. The most important information is located on the horizontal broad line in the center of the image. The arrows in the 2D-FFT image indicate the location of the propagating wave information for the forward (green) and backward (gray) propagating waves, with respect to the propagation direction of the incident laser beam incoming from the left side of the image. The slight trend towards an ellipsoidal shape of the signal with the crossing points not being located in a straight line above each other is conditioned on the anisotropic character of the AlN substrate.[7] The two tilted lines in the 2D-FFT emerge from the aforementioned Fresnel fringes in the microscope image.[8]

As already mentioned, the spacings between the wavefronts are different for the forward and backward propagating waves leading to the two different momentum values in the 2D-FFT plot, Fig. 6.2(b). This behavior can be explained with the direction of the incoming IR light. As illustrated in Fig. 6.3(a), the IR beam illuminates the sample under an incidence angle α, leading to the launching process off the MoO_3 flake edge. The wavevectors of the propagating waves have the same absolute value but different directions, as the wave on the left side of the flake propagates into $-x$ direction while the wave on the right side propagates into $+x$ direction. The standing wave imaged with the microscope arises due to interference with the illuminating IR light through the x-component of its momentum $k_{\mathrm{pt}} = \sin(\alpha)\,\mathbf{k}_{\mathrm{IR}}$:

$$\begin{aligned} |E_{\mathrm{tot}}|^2 &= \left|e^{\pm i k_{\mathrm{P}} x} + e^{i k_{\mathrm{pt}} x}\right|^2 \\ &= 2\left(1 + \cos\left[\left(\pm k_{\mathrm{P}} - k_{\mathrm{pt}}\right) x\right]\right) \\ &= 2(1 + \cos[\underbrace{\left(k_{\mathrm{pt}} \mp k_{\mathrm{P}}\right)}_{=k_{\mathrm{int}}^{\pm}} x]). \end{aligned} \tag{6.3.2}$$

In the case of the wave traveling into the $+x$ direction, the wavevectors point towards the same direction, leading to an interference pattern with $k_{\mathrm{int}}^{+} = k_{\mathrm{pt}} - k_{\mathrm{P}}$. For the wave propagating into the other direction, the wavevectors point to different directions, thus a standing wave with spatial frequency $k_{\mathrm{int}}^{-} = k_{\mathrm{pt}} + k_{\mathrm{P}}$ is observed. Both cases are plotted in Fig. 6.3(b).

This observation matches very well with state-of-the-art publications, where propagating waves of surface phonon polaritons have been measured using tip-based near-field microscopy [48, 137, 158, 159]. Thus, the observation of propagating SPhP waves is not in itself a novel finding, however, they have never been reported using any wide-field imaging approach. The pronounced advantage here lies in the abil-

[7] With increasing frequency the ellipsoidal shape becomes clearer and the crossing points position themselves in the direction of the optical axis. Further details will be stated in Sec. 6.3.1, however, no further experiments discussing the anisotropy have been carried out yet.

[8] The Fresnel fringes lead to streaks in the 2D-FFT rather than spots for periodic waves like the polaritons due to their non-periodic Bessel-like behavior, i.e., no constant periodicity.

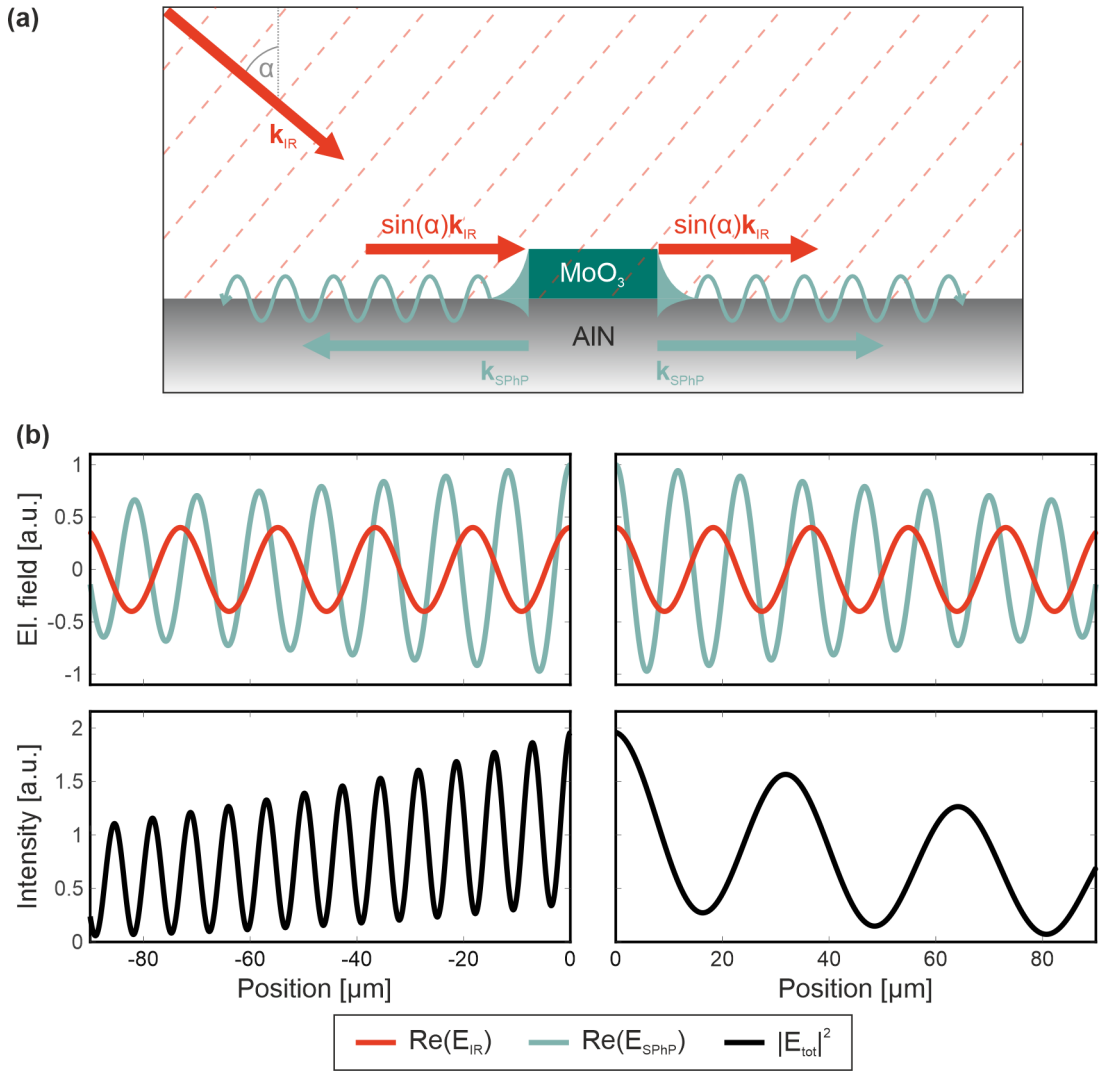

Figure 6.3. *Launching process and interference picture of incoming light and propagating SPhPs.* (a) The IR-FEL beam illuminates the sample under an angle α leading to the launching of propagating surface waves into forward and backward direction with respect to the incoming light. (b) The propagating wave and the incoming IR wave interfere and thus create a standing wave with lower ($+x$ direction) and higher ($-x$ direction) wavenumber leading to different interference patterns, see Eq. (6.3.2).

ity of spectral scanning, i.e., recording images for a variety of frequencies in very short time compared to tip-based techniques. Therefore, the frequency-dependent behavior of propagating waves can be analyzed in great detail.

By changing the IR frequency, the periodicity of the interference patterns and thus the associated 2D-FFT changes. This is visualised in Fig. 6.4 by dispersion plots for real space (a) and momentum space (b). Both plots have been created by stacking horizontal line cuts through the real space and momentum space images, respectively, for every frequency. Hence, both plots show the IR frequency dependence (y direction) of the spatial and momentum behavior of the polariton, respectively. Fig. 6.4(a) shows very nicely the frequency-induced change in periodicity of the in-

terference patterns for both sides of the flake. The two dashed white lines point out the boundaries of the MoO_3 flake. Based on Eq. (6.3.2), the periodicity P can be written as

$$P^{\pm} = \frac{2\pi}{k_{\mathrm{pt}} \mp k_{\mathrm{P}}}, \tag{6.3.3}$$

with P^{+} the periodicity for propagation in forward direction and P^{-} the periodicity of a wave propagating in backward direction, respectively. The changing momenta of the launched waves can also be identified in the dispersion plot in Fig. 6.4(b). The strong SFG signal of the propagating wave into forward direction leads to a pronounced dispersion curve in the plot. Less obvious but still distinguishable is the dispersion curve for the backward propagating wave with higher momentum. The blue dashed (dotted) line shows the calculated dispersion. It was obtained by calculating the polariton dispersion (blue solid line) with the dielectric function of AlN [157] and adding (substracting) the photon momentum k_{pt}. The gray dashed line illustrates the light line. As can be seen nicely, the experimental data matches very well with the expected dispersions.

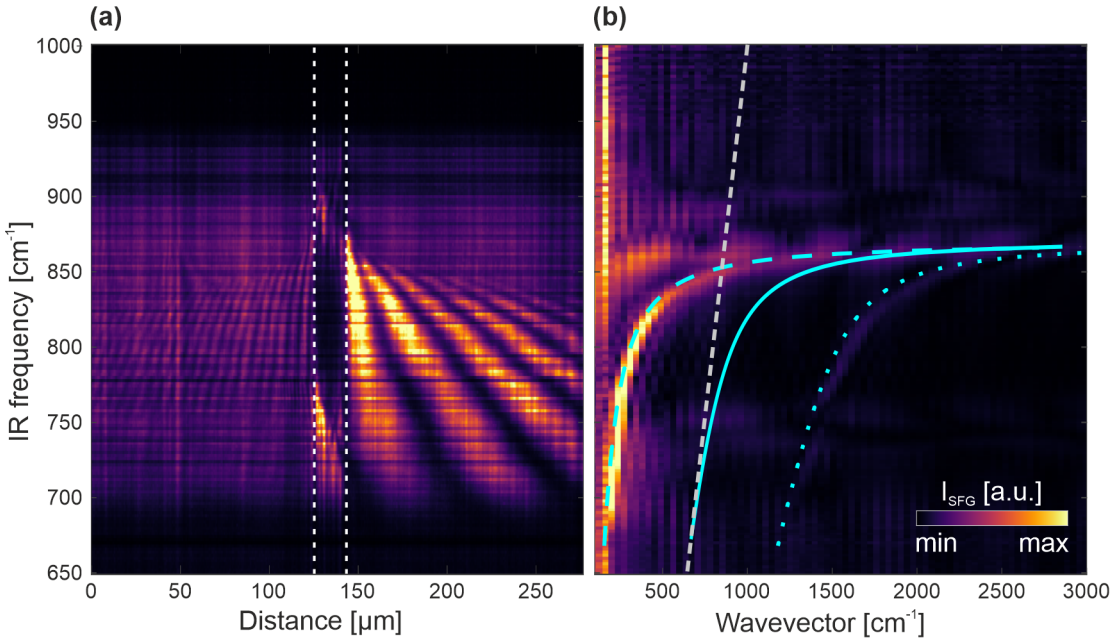

Figure 6.4. *Dispersion plots for real space and momentum space.* (a) Real space dispersion plot of propagating waves showing the decreasing periodicity of interference fringes for an increase in the IR frequency. The white dashed lines indicate the boundaries of the MoO_3 flake. (b) Momentum space dispersion plot from 2D-FFT showing dispersion curves for the two propagating waves in forward and backward direction, respectively. The blue dotted (dashed) lines represent the calculated dispersions for forward (backward) propagation. The blue solid line represents the dispersion curve for the propagating wave itself with k_{SPhP} and the dashed gray line the corresponding light line.

6.3.1 Polariton propagation anisotropy

So far, the in-plane anisotropy of the m-cut AlN was not considered. For this crystal cut, the optical axis (also referred to as c-axis) of the AlN substrate is in-plane. Thus, sample rotation leads to different resonance responses. In the following, differences in the optical response for the cases c‖x and c‖y are discussed.

Fig. 6.5(a,b) shows SFG images of propagating waves launched by MoO_3 flakes with their long edge oriented perpendicular (a) and parallel (b, with an offset of 7°) to the optical axis (white dashed line). In the case of perpendicular orientation of the flake, the wavevector of the propagating waves is parallel to the optical axis, referred to as an extraordinary wavevector $\mathbf{k}_\mathrm{e}$. A propagating wave launched off a flake with its propagation direction perpendicular to the optical axis can be described by the ordinary wavevector $\mathbf{k}_\mathrm{o}$. The dispersion of SPhPs can be calculated using the dielectric function with its components parallel to the optical axis $\varepsilon_\parallel$ and perpendicular to the optical axis $\varepsilon_\perp$, Eq. (6.3.1), following [160]

$$k_\mathrm{e} = \frac{\omega}{c}\sqrt{\frac{\varepsilon_\parallel\varepsilon_\perp - \varepsilon_\perp}{\varepsilon_\parallel\varepsilon_\perp - 1}}, \quad k_\mathrm{o} = \frac{\omega}{c}\sqrt{\frac{\varepsilon_\perp}{\varepsilon_\perp + 1}}, \tag{6.3.4}$$

describing the propagation along and perpendicular to the c-axis. The panels (c) and (d) in Fig. 6.5 show the corresponding dispersion plots for scans over the whole AlN Reststrahlen band. The gray dashed (dotted) lines represent the light lines, and the blue dashed (dotted) lines illustrate the calculation of $\Re(\mathbf{k}_\mathrm{e})$ and $\Re(\mathbf{k}_\mathrm{o})$ for co- and counter-propagating polaritons, respectively. For better visibility of the dispersion for the counter-propagating wave, the high-wavevector regions of the images is multiplied by 3.

It can be seen, that the calculation fits the measured data nicely. A change in orientation of the optical axis leads to a change in the polariton dispersion, i.e., the cut-off frequency $\omega_\mathrm{s,e}$ is $\sim 17\,\mathrm{cm}^{-1}$ red-shifted with respect to $\omega_\mathrm{s,o}$. A line-cut through the dispersions for c‖x and c‖y at $\omega_\mathrm{IR} = 820\,\mathrm{cm}^{-1}$ is depicted in Fig. 6.5(e) to stress the difference in k_e and k_o. For a better comparison, the SFG signal of the counter-propagating wave is multiplied by 10. The plots highlight the shift in momentum for the rotation of the sample, and, hence, the propagation direction with respect to the optical axis. Here, a shift of $\Delta k_\mathrm{fw} \approx 135\,\mathrm{cm}^{-1}$ for the forward propagation and a shift of $\Delta k_\mathrm{bw} \approx 170\,\mathrm{cm}^{-1}$ for the backward propagation arises. These values are in good agreement with the theoretical prediction of $\Delta k \approx 143\,\mathrm{cm}^{-1}$, with small differences attributed to noise and limited momentum resolution.

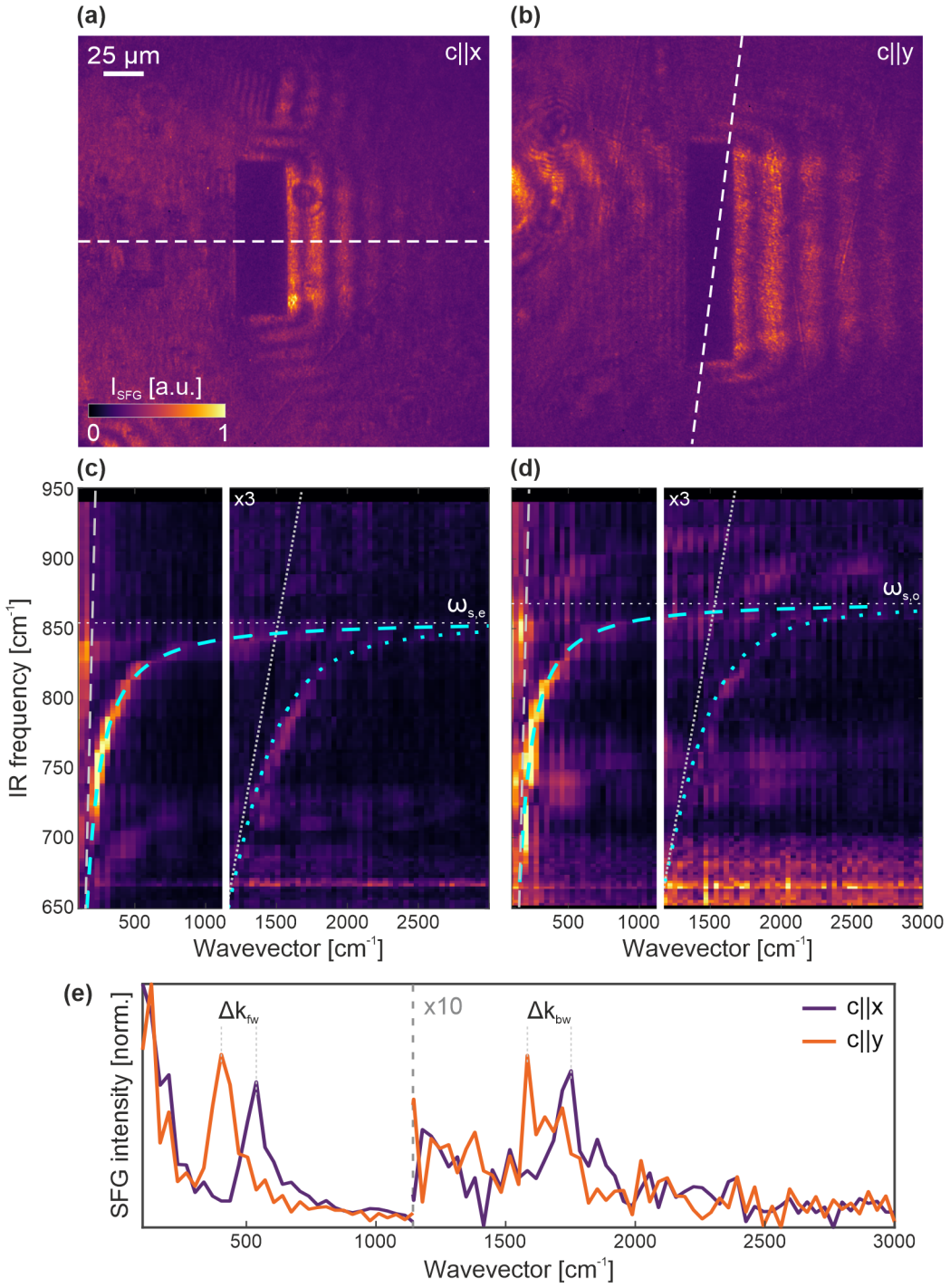

Figure 6.5. *Dispersion plot comparison for different orientations of the optical axis of the AlN substrate with respect to the polariton propagation direction.* SFG images of propagating waves at $\omega_{\mathrm{IR}} = 826\,\mathrm{cm}^{-1}$ launched by flakes oriented perpendicular (a) and parallel (b) to the optical axis (white dashed lines). (c,d) Corresponding dispersion plots, intensity in right parts of panels is multiplied by 3. The gray dashed/dotted lines show the light lines and the blue dashed/dotted curves depict a fit using $\mathbf{k}_{\mathrm{e}}$ for a wavevector with propagation direction parallel to the optical axis (a) and $\mathbf{k}_{\mathrm{o}}$ for a wavevector with a propagation direction perpendicular to the optical axis (b). The white dashed lines in (c,d) denote the cut-off frequencies $\omega_{\mathrm{s,e}}$ and $\omega_{\mathrm{s,o}}$, respectively. At $\omega_{\mathrm{IR}} = 670\,\mathrm{cm}^{-1}$, a CO_2 absorption line is visible due to normalization of the data for each frequency. (e) Line cut through (c) (purple) and (d) (orange) at $\omega_{\mathrm{IR}} = 820\,\mathrm{cm}^{-1}$ with a distinct momentum shift between k_{e} and k_{o} for forward and backward propagating polariton.

6.3.2 Directional launching with light polarization

Until now, the polarizations of the IR and VIS beams have not been discussed. As will be shown in the following, the laser polarization is important for the launching efficiency and direction. The polarizations considered are p-polarized light (parallel to the plane of incidence) and s-polarized light (perpendicular to the plane of incidence, from German: 'senkrecht'). The top images in Fig. 6.6 illustrate both configurations on the example of the IR beam.

IR polarization

Phonon polaritons are excited by the IR light, hence it is reasonable to assume an influence of the polarization on the excitation of propagating waves. The intensity detected by the SFG microscope is related to the incident IR electric field $\mathbf{E}_{\mathrm{IR}}$, Eq. (3.2.24). For p- and s-polarization, respectively, it reads

$$\mathbf{E}_{\mathrm{IR,P}} = \begin{pmatrix} E_{\mathrm{x,IR}} \\ 0 \\ E_{\mathrm{z,IR}} \end{pmatrix}, \qquad \mathbf{E}_{\mathrm{IR,S}} = \begin{pmatrix} 0 \\ E_{\mathrm{y,IR}} \\ 0 \end{pmatrix}. \tag{6.3.5}$$

The IR polarization is also illustrated in the top panels of Fig. 6.6(a,d), depicted as black arrows. The other panels show SFG images recorded with the two IR polarizations for different sample orientations (flake with long edge oriented vertical or horizontal).

It is evident that polaritons are launched for specific combinations of polarization and orientation. For p-polarization, propagating waves are observed along the x direction when the long edge of the MoO_3 flake is along the y direction (b), but no propagating wave is detected when the flake is rotated by 90° (c). For s-polarization the opposite behavior appears: propagating waves arise for an MoO_3 flake with its long edge along x (f) while an image with a flake along y does not show any features (e). Apparently, the interferometric detection works more effectively for polarization and propagation pointing into the same direction, i.e., in horizontal direction for p-polarization and in vertical direction for s-polarization. In addition, launching from the long edge of the MoO_3 flakes is observed much more efficient than launching from the short edge.

The absence of propagating waves in the SFG image (e) can be explained by the interference of the polarized IR light with the propagating wave. Fig. 6.7 illustrates the polariton field exemplarily for polariton propagation in x direction. This field has vector components in x and z direction. As Eq. (6.3.5) shows, only the p-polarized IR-beam has vector components in the same directions. The s-polarized beam only has a vector component in y direction and hence cannot interfere with the polariton field. This explanation does not hold for the case of (c), where the polariton field

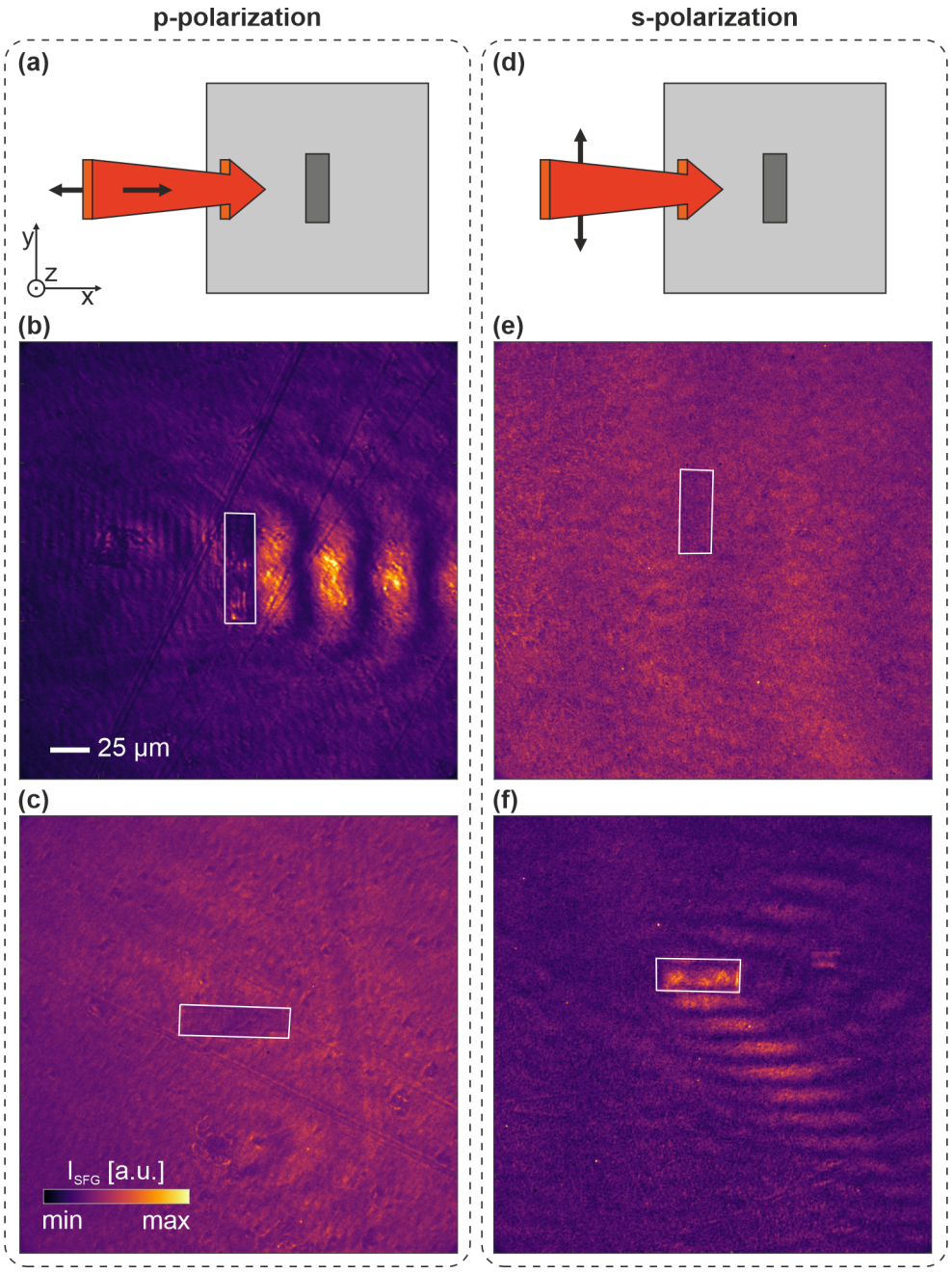

Figure 6.6. *Influence of IR polarization on propagating waves.* (a) IR excitation in p-polarization (parallel to the plane of incidence) launches propagating polaritons for an MoO_3 flake with the long edge along y (b) with a wavevector in polarization direction. No modes are launched for a flake rotated by 90° (c). (d) IR excitation in s-polarization (perpendicular to the plane of incidence): no modes appear for a flake with long edge along y (e), but for a flake with long edge along x (f). All images at $\omega_{IR} = 777\,\mathrm{cm}^{-1}$. White lines illustrate the positions of the MoO_3 flakes.

launched from the long edge has y and z components. However, the SFG microscope does only detect the in-plane field components of the polariton, since the out-of-plane components of $\chi^{(2)}$ vanish. Thus, any launched polariton wave cannot be detected with the SFG microscope in this configuration.

Additionally, it is striking that only the long edge of the flake launches polariton

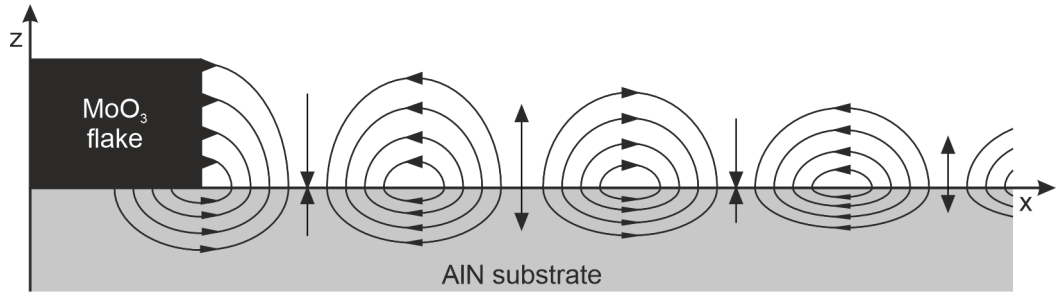

Figure 6.7. *Sketch of a polariton field for propagation in x direction.* The polariton field is launched by the MoO_3 flake and propagates in x direction with a maximum field intensity at the launcher.

waves and no signal from short-edge launching can be detected. The reason might be the anisotropy of MoO_3, which has not been discussed so far. A possible explanation could be that the orientation of the optical axis is beneficial only for launching off one edge, here the long edge. Further studies are needed to prove this hypothesis.

VIS polarization

The evolution of the propagating waves is not affected by the polarization of the visible beam, which is plausible since the modes are launched by the IR laser, while the VIS beam only acts as the upconversion beam for the SFG process. In Fig. 6.8, two images are shown, recorded with the IR in p- and the VIS in s- and p-polarization, respectively. Undoubtedly, the SFG intensity for the mixed polarization (IR-p, VIS-s) scan is increased compared to the homogeneous polarization (IR-p, VIS-p) scan. This behavior can also be observed for a different IR polarization: if the IR beam excites the sample with s-polarization, the best signal is achieved for a visible beam in p-polarization.

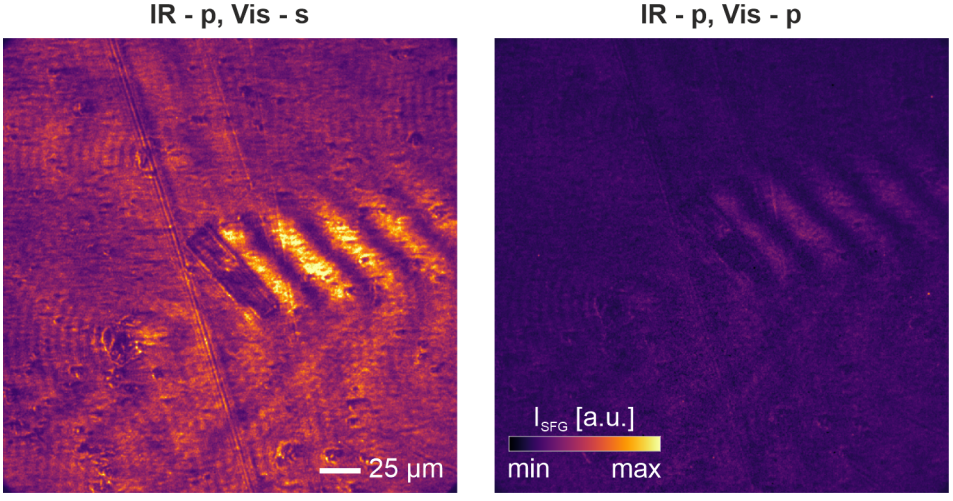

Figure 6.8. *Influence of VIS polarization on SFG images.* SFG images at $\omega_{IR} = 807\,cm^{-1}$ with the visible beam in s-polarization (left) and p-polarization (right). The excitation of modes is not affected by the polarization of the visible beam as it only acts as an upconversion beam. However, the intensity of the SFG signal is clearly increased for IR-p, VIS-s.

The electric fields $\mathbf{E}_{\mathrm{VIS}}$ for p- and s-polarization can be expressed by the corresponding vector components $E^{\mathrm{p}}_{\mathrm{VIS,x}}$ and $E^{\mathrm{s}}_{\mathrm{VIS,y}}$, respectively. For AlN, the SFG intensities for visible p- and s-polarization, respectively, and the IR in p-polarization read (see Sec. 3.2.2, Eq. (3.2.26))

$$I^{\mathrm{SFG}}_{\mathrm{PP}} \propto |\chi^{(2)}_{\mathrm{xxx}} E_{\mathrm{x,VIS}} L_{\mathrm{xx}} E_{\mathrm{x,IR}}|^2 \tag{6.3.6a}$$

$$I^{\mathrm{SFG}}_{\mathrm{SP}} \propto |\chi^{(2)}_{\mathrm{yyx}} E_{\mathrm{y,VIS}} L_{\mathrm{xx}} E_{\mathrm{x,IR}}|^2 \tag{6.3.6b}$$

with L_{xx} the Fresnel coefficient and considering only the non-vanishing tensor elements of the nonlinear susceptibility $\chi^{(2)}$. Assuming that $|E^{\mathrm{p}}_{\mathrm{VIS,x}}| = |E^{\mathrm{s}}_{\mathrm{VIS,y}}|$, the only difference between the two equations is given by the tensor elements $\chi^{(2)}_{\mathrm{xxx}}$ and $\chi^{(2)}_{\mathrm{yyx}}$ leading to the different intensities in the SFG images. Notably, in the given geometry and for the symmetry of the $\chi^{(2)}$ tensor, the SFG microscopes solely probes the in-plane field components of the polariton. Thus, the SFG microscope measures the in-plane field $E_{\mathrm{x,y}}$ of the polariton in contrast to s-SNOM, which always measures the out-of-plane field E_{z} only.

6.4 Outlook

The SFG microscope is an ideal tool for measuring propagating polaritons with a high spatial resolution and full spectral information. Launching efficiency and propagation direction can be influenced by changing the lasers' polarizations in a combination with rotating the sample. However, during the data analysis not all questions could be answered, yet, and many more were not even addressed yet. This section provides an outlook on so far unaddressed phenomena observed with the SFG imaging focusing on the propagating polaritons excited by s-polarized light and on the optical response inside the MoO_3 flake.

6.4.1 Optical response for s-polarized IR light

When the flake is turned by 90°, the propagating waves do not propagate in the x direction, but in the y direction, as illustrated in Fig. 6.9(a). While Sec. 6.3.2 and Fig. 6.6 already discussed the influence of polarization on the propagation direction, here the polariton dispersion shall be of interest. The exciting IR beam has no k_y component, hence no difference in the up- and downward fringes is expected. The imaged waves should directly correspond to the propagating SPhPs, leading to the same propagation fringes for upward and downward propagating SPhPs. To corroborate this hypothesis, the frequency dependence is plotted in a dispersion plot, see Fig. 6.9(b). Notably, in contrast to Fig. 6.4, vertical cuts through the 2D-FFT plots were extracted.

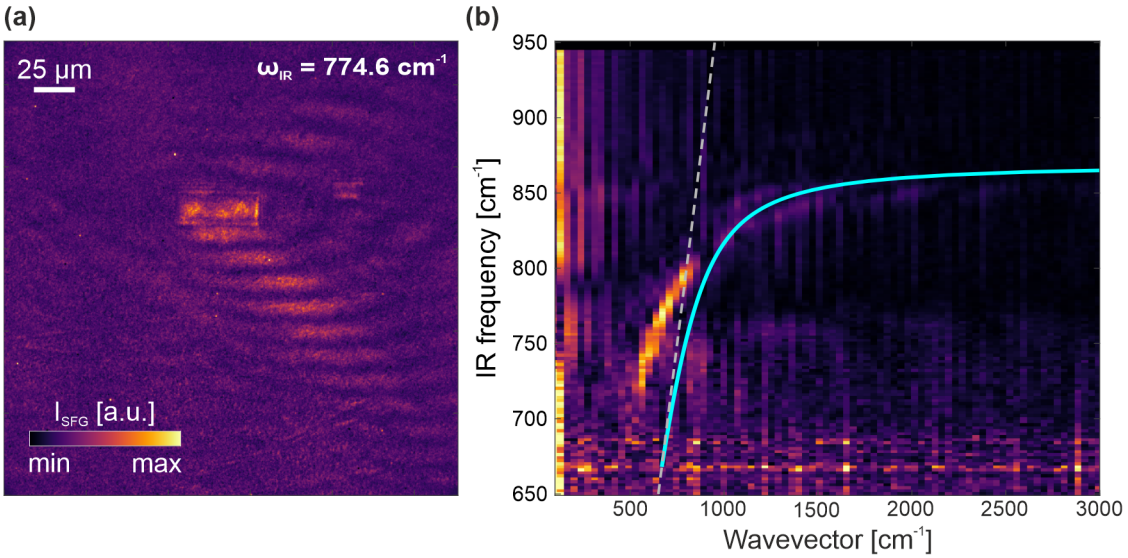

Figure 6.9. *Propagation and dispersion plot for launching perpendicular to the incident IR laser.* (a) SFG image of propagating waves from a horizontally oriented MoO_3 launcher. (b) Dispersion plot for the corresponding scan. Without the influence of a $k_{IR,y}$ component, the imaged waves propagating up and down, respectively, correspond directly to the propagating SPhP waves, hence one dispersion curve fits both modes. The blue solid line illustrates the calculated $\mathbf{k}_{\mathrm{SPhP}}$ and the gray dashed line the corresponding light line.

In contrast to Fig. 6.4(b), the two polariton dispersions for upward and downward propagation nearly overlap, in good agreement with the similar fringe spacing of the propagating waves in (a). Here, the bright dispersion represents the downward propagating wave and the slightly shifted less intense dispersion represents the upward propagating wave. The blue solid and gray dashed lines represent the calculations for k_{SPhP} and the vacuum light line k_{pt}, respectively. For higher frequencies, the calculations and data fit nicely, however, for lower frequencies an offset occurs. At this stage of the data analysis, this offset it attributed to the AlN anisotropy and has to be investigated further.
In addition, a consistent offset between the polariton wave fronts and the direction of energy flow is observed for all of the data. The magnitude of this offset varies for different geometries and MoO_3 flake orientations with respect to the AlN optical axis. In Fig. 6.9, this offset is particularly pronounced. So far, no consistent physical mechanism to explain this observation could be identified, but is assumed to be linked to the anisotropy of AlN and the twist between AlN and MoO_3.

6.4.2 MoO_3 response to IR excitation

So far, no data analysis on the images of the MoO_3 flake itself has been discussed. As shown in Fig. 6.10, the spectroscopic flake response is highly dependent on the IR frequency. Exemplary SFG images in (a) show the transition from homogeneous, bright SFG signal across the whole flake (left) to strongly suppressed signal (middle), and a standing wave pattern inside the flake (right). The influence of the underlying

AlN substrate has not been analyzed yet.
A comparison of the SFG intensity spectra of both the AlN substrate (purple) and the MoO_3 flake (orange) is plotted in Fig. 6.10(b). It can be clearly seen that the two spectra differ tremendously. The images in (a) correspond to the frequencies marked by the dashed lines. Additionally, panel (c) shows a spectro-spatial dispersion plot along the y-axis of the flake. The signal was integrated along the x-axis of the flake and is plotted as a function of the IR frequency. The standing-wave pattern as in (a,right) can also be found in the right-hand side of the dispersion plot.

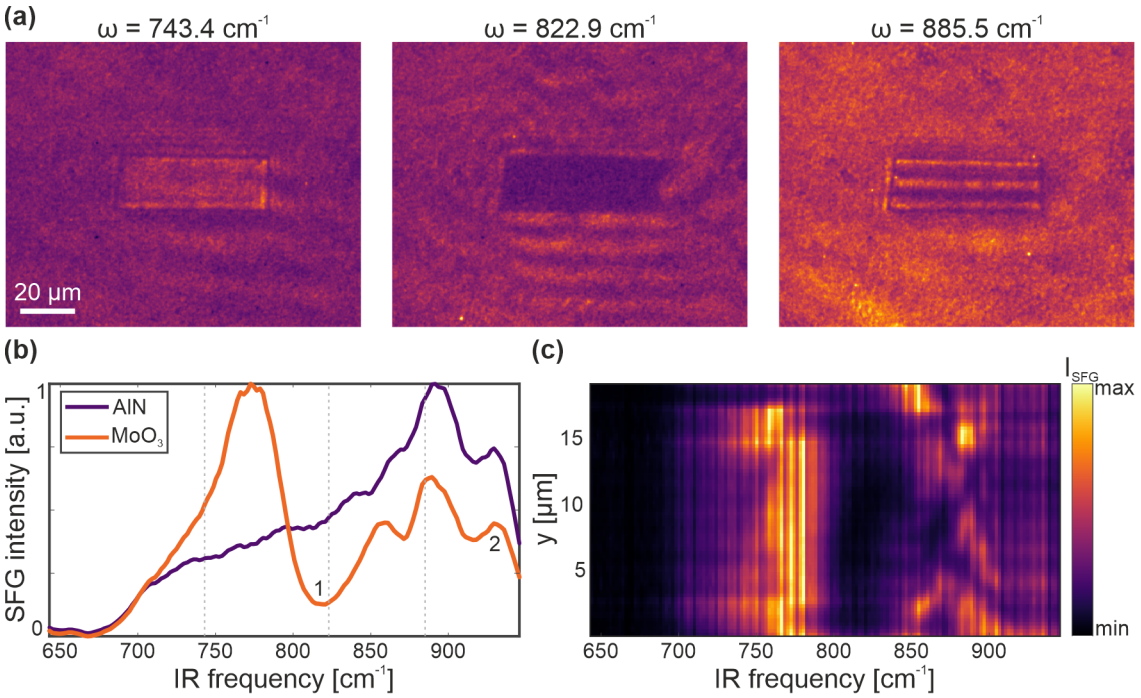

Figure 6.10. *Frequency dependent behavior of MoO_3 flake.* (a) SFG images for different IR wavenumbers. (b) SFG intensity spectra for AlN substrate (purple) and MoO_3 flake (orange). Dashed lines give spectral positions of SFG images in (a). (c) Spatio-spectral dispersion plot for MoO_3 flake along y-axis. Colorscale valid for (a) and (c).

A detailed evaluation of the data is a next step, taking into account the different polariton resonances for the AlN substrate and the MoO_3 flake, respectively, including the anisotropic characteristics of the materials. As an example, the features 1 and 2 (Fig. 6.10(b)) are in good agreement with the TO and LO frequencies, $\omega_{TO} = 821\,cm^{-1}$ and $\omega_{LO} = 963\,cm^{-1}$ [142], of the MoO_3 Reststrahlen band along the [001] crystal direction. However, this analysis is well beyond the scope of this thesis.

7

Collective Behavior of SiC Phonon Polariton Resonators

This chapter discusses the collective behavior of phonon polariton resonators in 1D arrays. Differences in the optical response for different illumination directions are discussed, proving the importance of phase relationships. The dependence of the collective response on the array period is discussed as well as the coupling-dependent splitting into two modes of the monopolar resonance. The chapter concludes with an outlook regarding the coupling between different 1D arrays in addition to resonator coupling inside one array.

In Secs. 2.3 and 2.4, localized phonon polariton modes in cylindrical pillar-like resonators have been discussed in greater detail. By taking the step from a single resonator to an array, not only the localized modes but also strong coupling to propagating modes may become important, arriving at a more accurate picture of strong coupling in these systems. In this chapter, the build up of collective modes, starting from a single pillar and adding additional neighboring pillars one-by-one to form a one-dimensional (1D) array is discussed. Measurements on 4H-SiC arrays with periods of $p_1 = 8\,\mu\text{m}$ and $p_2 = 6.5\,\mu\text{m}$ are compared, while the pillar diameter was kept constant at $d = 2\,\mu\text{m}$ for all measurements. An example SEM image of pillar 1D arrays with a period of $8\,\mu\text{m}$ is shown in Fig. 7.1(a) with the corresponding SFG images for each array in Fig. 7.1(b). For a comprehensive investigation, measurements were performed for 1D arrays oriented perpendicular and parallel to the illumination direction of the FEL.

7.1 Collective Modes in 1D micropillar arrays

Localized resonances inside the pillar can couple to a propagating polariton on the substrate surface, as the single resonator can essentially act like a dipole antenna. If a second pillar is placed close by, these propagating modes will couple both pillars [57]. This effect will reoccur as more pillars are added. Complementary, free-space coupling between the dipoles of each pillar, similar to that observed in molecules [161], may also act as a coupling mechanism. A pronounced difference between these two coupling mechanisms is the distance dependence between neighboring pillars. While

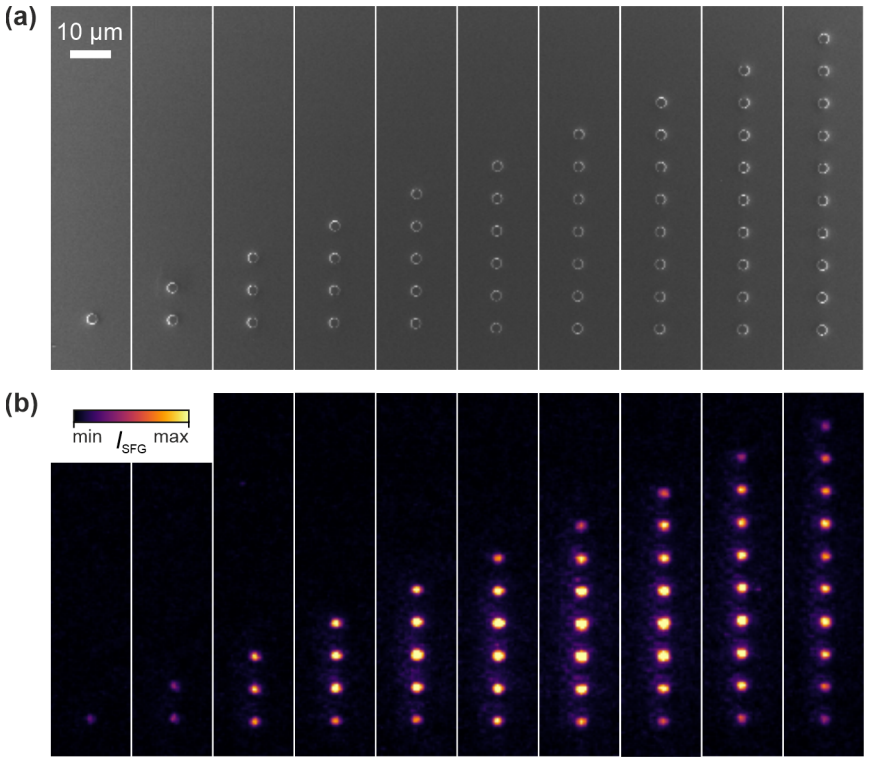

Figure 7.1. *4H-SiC Micropillars.* (a) SEM images for 1D pillar arrays with period $p = 8\,\mu\text{m}$. The scale bar is 10 µm. (b) SFG images of the pillars in (a) at $\omega_{IR} \approx 875\,\text{cm}^{-1}$.

polariton coupling strength would be oscillatory with distance, due to the propagating nature of the polariton, the dipolar coupling strength would simply decay with distance. Additionally, comparing in-phase and out-of-phase excitation of the neighboring pillars by different illumination geometries may help to clarify the mechanism. In Fig. 7.1(b), the intensity distributions of 1D arrays with increasing number of pillars are shown for $p = 8\,\mu\text{m}$ for in-phase excitation through perpendicular illumination at $\omega_{IR} = 875\,\text{cm}^{-1}$. One immediate observation is the steep increase in overall intensity, as more pillars are added.

In Sec. 5.2, the possibility of analyzing SFG spectra for individual pillars has been introduced. Hence, also the optical response of the individual 1D arrays can be compared, see Fig. 7.2 for perpendicular (a) and parallel (b) illumination. The spectra show the array response across the whole SiC Reststrahlen band for pillars arrays with a period $p = 8\,\mu\text{m}$. The LO resonance at $\omega_{IR} = 964\,\text{cm}^{-1}$ and the dipolar resonance at $\omega_{IR} \approx 910\,\text{cm}^{-1}$ remain mostly unchanged for both illumination directions, as well as for different amounts of pillars per array. In the lower frequency regime, weak signal can be observed for the monopolar modes in parallel illumination direction. The signal remains mainly unchanged as the number of pillars in the array increases. However, for the case of perpendicular illumination, two peaks appear for monopolar modes at $\omega_{IR} \approx 850\,\text{cm}^{-1}$ and $\omega_{IR} \approx 875\,\text{cm}^{-1}$ whose intensities increase steeply when adding more pillars. This intensity behavior is an indication of collective behavior. The interpretation fits previous work on 2D arrays, where the pillars

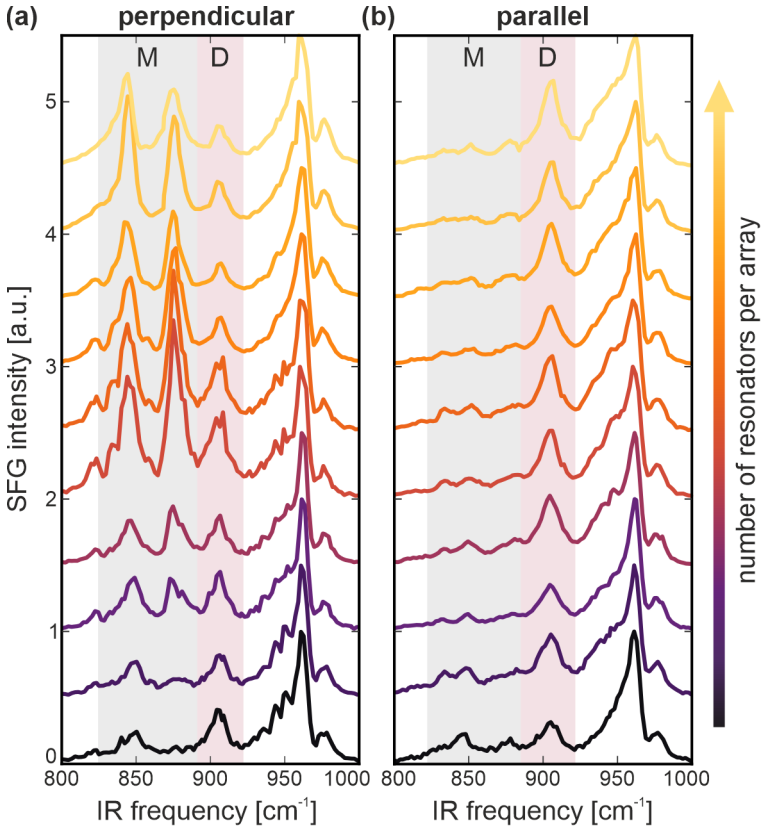

Figure 7.2. *SFG spectra for individual 1D micropillar arrays.* SFG spectra for 1 to 10 pillars per array with perpendicular illumination (a) and parallel illumination (b) on arrays with a period $p = 8\,\mu m$. Each spectrum is normalized to the LO resonance. Monopolar region highlighted in gray, dipolar region highlighted in red.

show a collective behavior for the monopolar modes while the dipolar modes rather refer to localized modes only inside the pillars [59].
The two monopolar peaks in the spectra in Fig. 7.2(a) correspond to a coupling-induced splitting of the monopolar mode of a single pillar. The spectrum for a single pillar (bottom line, black) only shows a single monopole peak as there is no second pillar in vicinity to couple with. By adding more pillars to the array, the second monopolar peak forms, increasing in intensity for more pillars. Additionally, a slight red-shift is apparent in the monopolar modes, supporting the theory of coupling between the pillars.
The comparison of the illumination directions reveals the importance of the relative phase of the individual pillar's excitation. For perpendicular illumination, all pillars in a line experience the same phase as the wave fronts of the IR excitation are parallel to the 1D array in this case. In parallel illumination, the pillars experience a phase shift with respect to each other. This phase shift prevents efficient coupling and the built up of a collective response in this geometry, Fig. 7.2(b). A second hint on the influence of the phase is given by comparing the intensites of the individual pillars in an array, shown in Fig. 7.3.

The intensity distribution along the individual pillars in an array is plotted for five to

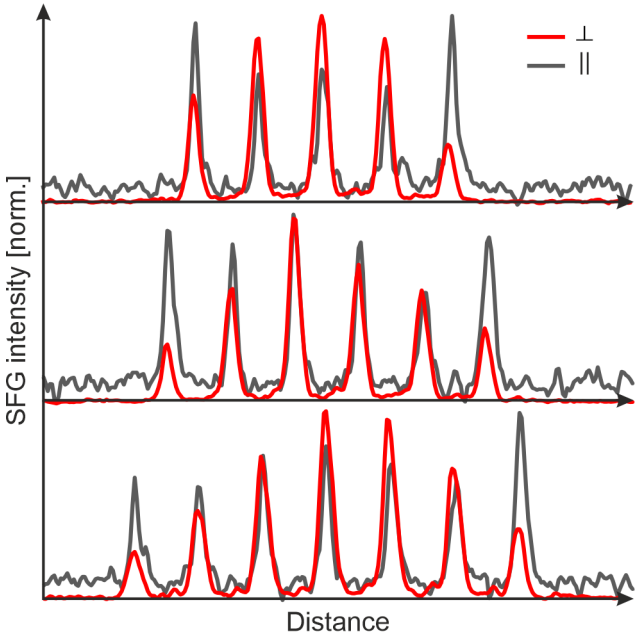

Figure 7.3. *Modal behavior and intensities of individual pillars.* Line cuts along the pillar arrays for perpendicular (red) and parallel (gray) illumination. They show a random intensity distribution along the pillars for the parallel case. For perpendicular illumination, the highest intensity is located in the center of the array with decreasing intensity to the sides.

seven pillars per array for perpendicular (red) and parallel (gray) illumination. The distribution is extracted from line cuts in SFG images at $\omega_{\mathrm{IR}} = 875\,\mathrm{cm}^{-1}$. The intensity distribution under parallel illumination gives a random picture without clear structure. The perpendicular case, however, reveals a structured intensity distribution with the highest intensity located at the array center and decreasing intensity towards the array edges. Thus, these distributions also indicate a collective behavior of the pillars provided that the pillars experience the same excitation phase.

In the picture of polariton-supported coupling, a phase shift can be induced not only by changing the illumination direction, but also by a change of the period in the pillar array. Coupling is expected to work more effectively, if the period matches the polariton wavelength. For the example of the first monopolar mode (M1) at $\omega_{\mathrm{IR}} = 850\,\mathrm{cm}^{-1}$, a launched polariton on a SiC substrate has a wavelength of $\lambda_{\mathrm{P}} \approx 11.4\,\mu\mathrm{m}$. The greater the mismatch between the wavelength and the period, the less effective the coupling should be, and thus, the intensity of the collective mode. Measurements on pillar arrays with a period of $p = 6.5\,\mu\mathrm{m}$ show qualitatively similar results as for $p = 8\,\mu\mathrm{m}$, however, as expected, with different intensity evolution. A direct comparison of modal intensities is provided in Fig. 7.4.

Comparisons are made between the two monopolar modes M1 (open symbols) and M2 (filled symbols), the two periods $p_1 = 8\,\mu\mathrm{m}$ (circles) and $p_2 = 6.5\,\mu\mathrm{m}$ (squares) and perpendicular (orange, red) and parallel (purple) illumination. For perpendicular illumination, the mode intensities increase with increasing number of pillars per array while no change is observed for parallel illumination as expected after previous

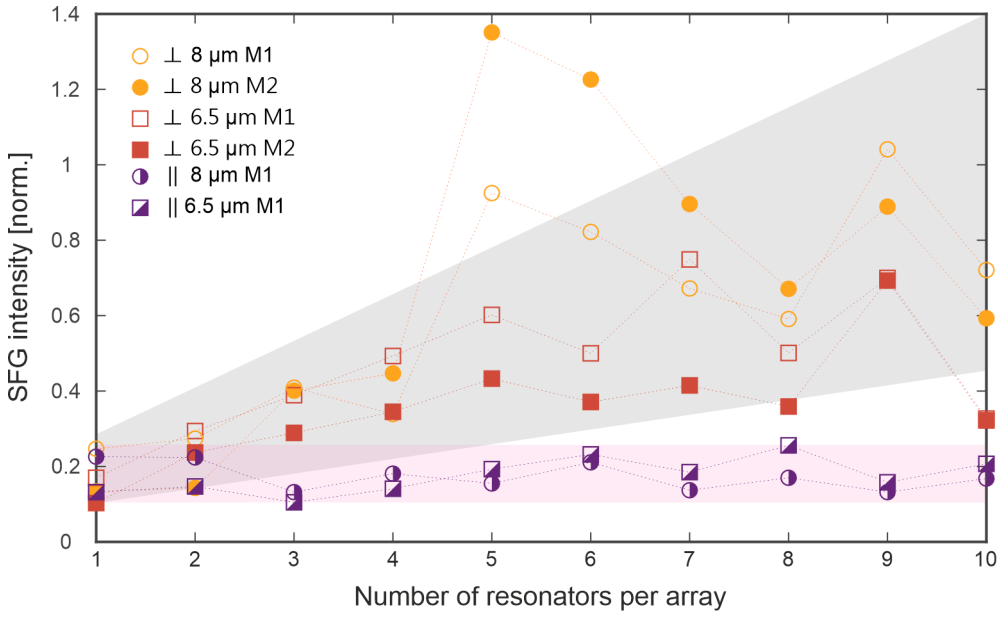

Figure 7.4. *Intensities of monopolar modes for different array diameters.* SFG intensities of monopolar modes M1 (open) and M2 (filled) as a function of the number of pillars per 1D array, with two different periods (circle ≙ 8 µm and square ≙ 6.5 µm) for perpendicular cases (orange and red) and parallel illumination (purple). The gray and pink areas are a guide to the eye to illustrate the trend for perpendicular and parallel illumination, respectively.

discussion. For parallel illumination, only the M1 mode is plotted as an example. The overall trends are illustrated by the gray and pink areas for perpendicular and parallel illumination, respectively. The intensities M1 and M2 show a similar behavior, and increase or decrease uniformly. As expected, the mode intensity of the arrays with a smaller period is equal to or less than the intensities of the arrays with a period closer to the propagating polariton wavelength.

7.2 Discussion and Outlook

Multiple strong indicators of a gradual build up of a collective response from individual pillars in 1D arrays were observed. Clearly, the illumination direction and the spacing between the pillars of a 1D array has high impact on the collective behavior of pillar arrays. Further data analysis may give rise to a more detailed picture of collective modes.

Coupling between individual pillars in an array is sensitive to the distance between the pillars. The discussion above focused on 1D arrays with a spacing of 100 μm between the arrays. When this spacing is reduced, also coupling between the 1D arrays is expected which may modify their response.

Fig. 7.5(a) shows a dispersion plot of the detected SFG signal for the pillar arrays with $p = 6.5\,\mu\text{m}$. The dispersion plot directly reports on the formation of modes and their intensity in dependence of the number of pillars per array. A second

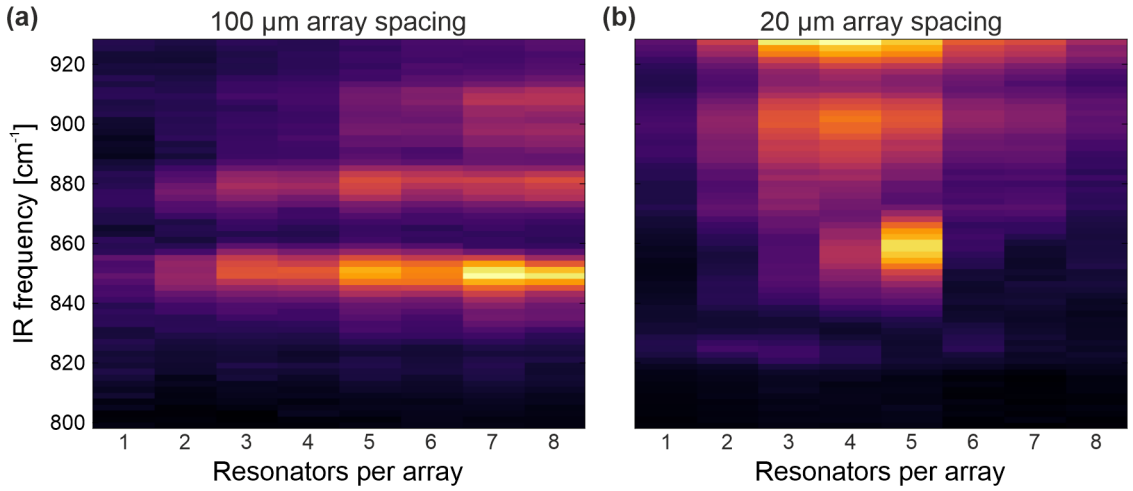

Figure 7.5. *Dispersion plots for pillar arrays with different spacings.* Dispersion plots for 1 to 8 pillars in a 1D array with $p = 6.5\,\mu m$ and 100 µm array spacing (a) and 20 µm array spacing (b).

dispersion plot is shown in Fig. 7.5(b) for a spacing of 20 µm between the 1D arrays. Obviously, the optical response is notably different from the optical response for a larger spacing. Hence, the optical response can be affected by the vicinity of another 1D array. By further decreasing the spacing, a 2D array is formed which represents one form of a metasurface [162]. Metasurfaces, in turn, are the perfect playground for observation and analysis of hybridization of modes and, for the specific case of phonon polariton pillars as the building blocks, the appearance of strong coupling. These physics will be explored in the upcoming chapter.

8

Spectroscopic and Interferometric Sum-Frequency Imaging of Strongly Coupled Phonon Polaritons in SiC Metasurfaces

This chapter discusses the hybridization of localized and propagating surface polaritons in metasurfaces of SiC micropillars which is motivated in Sec. 8.1. With SFG spectro-microscopy, the dispersion of the hybridized polaritons can be measured simultaneously in two complementary ways. Sec. 8.2 discusses the results based on angle-dependent resonant imaging of the sample and Sec. 8.3 discusses interferometry data on edge-launched propagating polaritons. Furthermore, it is shown that the hybridized polaritons are in the strong coupling regime. This is followed by discussing the observation of a polaritonic edge state in Sec. 8.4 and concluded by an outlook in Sec. 8.5.

The results of this chapter have been published on arXiv [P3] and the content here draws strongly from this publication.

8.1 Motivation

The last chapter already touched on the appearance of coupling between localized resonances and propagating polaritons in sub-wavelength structures such as periodic lattices of sub-wavelength structures like pillars or rods [163, 164]. This way, new polaritonic properties can be achieved [56, 165]. The hybridization of localized and propagating polaritons in such metasurfaces enables strong coupling [57, 62, 166, 167], sensing of molecules [60, 61], and directional thermal emission [62, 63, 133], or topologically protected edge states [64]. The properties of such polaritonic structures strongly depend on the excitation wavelength, because of the steep material dispersion induced by the underlying phonon resonances. For a full experimental characterization, one therefore needs tools that combine spectral information across a broad range of frequencies with spatial information from sub-diffractional to mesoscopic length scales.

As already discussed in Sec. 6.1, SFG spectro-microscopy combines the advantages of high spatial resolution, as in point-scanning techniques like s-SNOM, and the broad spectral range, as in nano-Fourier transform infrared (nano-FTIR) spectroscopy [62, 136]. Due to the ability of imaging propagating surface polaritons and localized

resonances in sub-diffractional microstructures while recording spectra at the same time, SFG spectro-microscopy is an ideal tool for detecting the dispersion of hybridized polaritons. It enables the simultaneous measurement of the dispersion in two complementary ways: by spectral imaging as in prism coupling [66, 168, 169] or thermal emission spectroscopy [62, 63] and by spatial interferometry as in s-SNOM [136, 137].

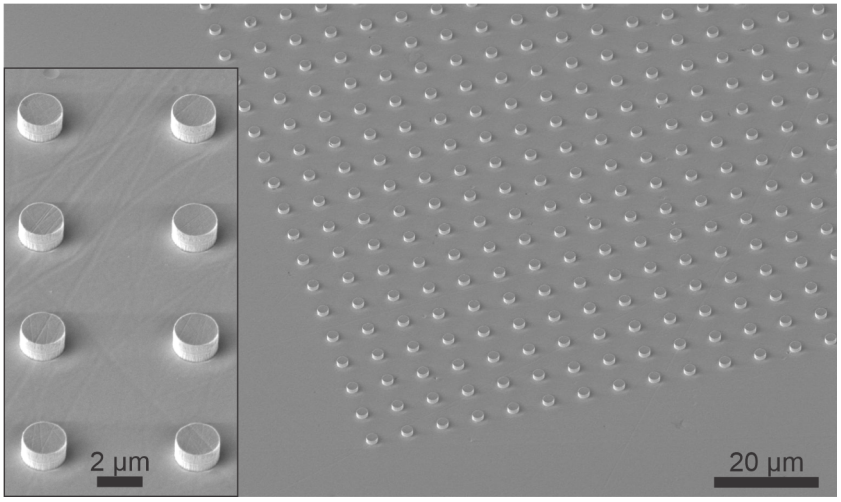

Figure 8.1. *SEM image of SiC micropillar array.* Micropillar array with periodicity $P = 7.3\,\mu m$ and diameter $D = 2.5\,\mu m$. Inset shows a zoom into pillars of the same array.

Measurements were performed using a 4H-SiC pillar array on a 4H-SiC substrate which is illustrated in Fig. 8.1. The pillars form a periodic lattice of $1 \times 1\,mm^2$ total size with periodicity $P = 7.3\,\mu m$ and a pillar diameter of $D = 2.5\,\mu m$. The sample enables the excitation of both propagating polaritons along the substrate surface, as well as highly confined localized modes within the pillars [57, 59].

The coupling of these propagating polaritons and two types of localized modes (monopole and dipole with coupling strengths g_1 and g_2, respectively) leads to hybridized polaritons, with a dispersion differing tremendously from the uncoupled, individual localized mode frequencies ω_M and ω_D and the dispersion of the propagating surface polariton ω_{SPhP} (Fig. 8.2) [62]. As shown in the numerical simulation in Fig. 8.2(b), due to the coupling the two crossing points of the SPhP dispersion (yellow dashed line) with the monopole (blue) and dipole mode (red), respectively, turn into avoided crossings in the hybridized polariton dispersion. This leads to three new branches with different dispersions (black solid lines). Direct coupling between monopole and dipole mode can be neglected because of insignificant spectral overlap. The hybridization can be modeled with a three-coupled oscillator model using the coupling matrix

$$\mathcal{M} = \begin{pmatrix} \omega_{\mathrm{SPhP}} & g_1 & g_2 \\ g_1 & \omega_{\mathrm{M}} & 0 \\ g_2 & 0 & \omega_{\mathrm{D}} \end{pmatrix}, \tag{8.1.1}$$

where the eigenvalues give the three hybridized polariton branches. As can be seen in Fig. 8.2(b), the avoided crossing and hence the coupling of the propagating polariton and the monopole mode is much stronger than the coupling with the dipole mode. This is because the SPhP near-fields match the out-of-plane polarization of the monopole mode, while the dipole mode fields are mostly in-plane [see Fig. 8.2(a)]. The coupling parameters $g_1 = 22\,\mathrm{cm}^{-1}$ and $g_2 = 5\,\mathrm{cm}^{-1}$ were obtained by matching the model with a full-wave simulation for different IR-incidence angles ϑ (absorption contour plot in Fig. 8.2(b)). Strong coupling is achieved between the monopolar resonance and the propagating surface polariton as $g_1 = 22\,\mathrm{cm}^{-1} > (\gamma_{\mathrm{M}} + \gamma_{\mathrm{SPhP}})/2 = (4.2\,\mathrm{cm}^{-1} + 5.4\,\mathrm{cm}^{-1})/2 = 4.8\,\mathrm{cm}^{-1}$. Although an avoided crossing between dipolar resonance and propagating polariton is apparent, the coupling is not yet in the strong coupling regime as $g_2 = 5\,\mathrm{cm}^{-1} < (\gamma_{\mathrm{D}} + \gamma_{\mathrm{SPhP}})/2 = (10.8\,\mathrm{cm}^{-1} + 5.4\,\mathrm{cm}^{-1})/2 = 8.1\,\mathrm{cm}^{-1}$. The linewidths were determined through analysis of the theoretical data of the uncoupled modes in Fig. 8.2(b).

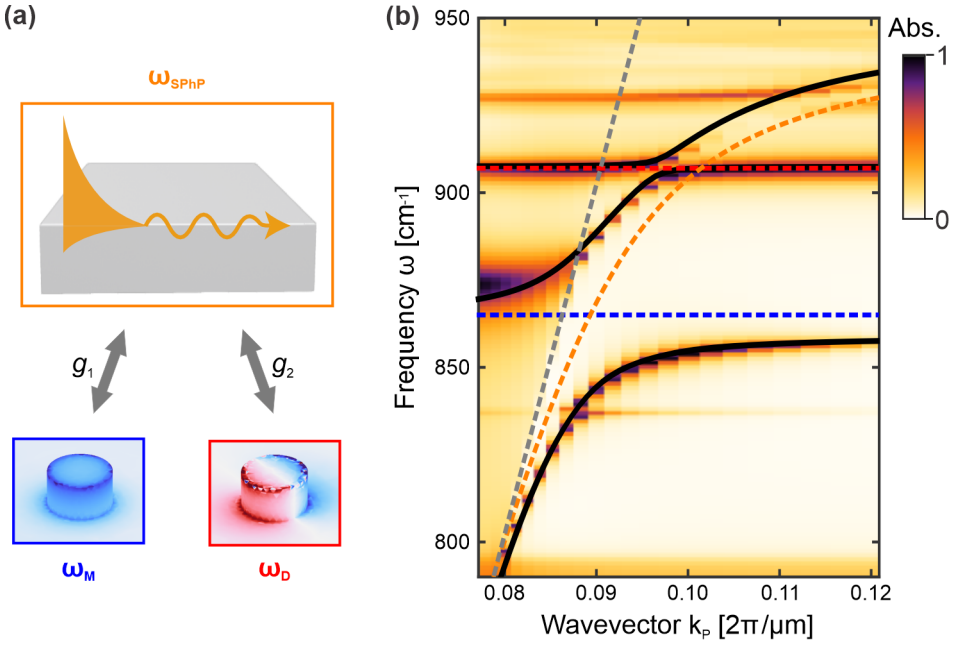

Figure 8.2. *Hybridization of propagating and localized SPhP modes.* (a) Sketch of a propagating surface polariton (orange) and simulations of the electric field on the surface of the micropillars for localized monopole (blue) and dipole (red) modes, respectively. (b) Dispersion plot with frequencies for individual, uncoupled modes (dashed lines) and hybridized polariton modes (black solid lines). The density plot is a full-wave simulation with COMSOL and the solid lines have been calculated with the coupled-oscillator model.

8.2 Experimental dispersion from azimuthal sample rotation using spectro-microscopy

With the technique of spectro-microscopy, the dispersion of hybridized propagating and localized polaritons can be directly measured by an azimuthal rotation of the sample, see Fig. 8.3(a). Since the polaritons have a much larger momentum than the photons, their dispersion is mostly below the light line (compare black lines with gray dashed line in Fig. 8.2) which usually prohibits direct excitation by an IR laser. However, this momentum mismatch can be overcome making use of the periodic lattice structure of the sample created by the micropillars. It provides reciprocal lattice vectors $\mathbf{G}_\mathrm{x}$ and $\mathbf{G}_\mathrm{y}$ for far-field excitation (Fig. 8.3(b)) according to

$$\mathbf{k}_\mathrm{exc} = \mathbf{k}_\mathrm{pt,ip} + m\mathbf{G}_\mathrm{x} + n\mathbf{G}_\mathrm{y}. \tag{8.2.1}$$

Here, m, n denote integers and $\mathbf{k}_\mathrm{pt,ip}$ is the in-plane photon momentum. A polariton with wavenumber k_P can be excited with the IR incidence angle ϑ and the azimuthal sample angle φ (Fig. 8.3(a)) if

$$k_\mathrm{P}^2 = \left(k_\mathrm{pt}\sin\vartheta\cos\varphi + m\frac{2\pi}{P}\right)^2 + \left(k_\mathrm{pt}\sin\vartheta\sin\varphi + n\frac{2\pi}{P}\right)^2 \tag{8.2.2}$$

is fulfilled, with P being the lattice periodicity. This is shown in Fig. 8.3(b), depicting an example of the lower polariton branch at a fixed incidence angle $\vartheta = 46°$, where the black line illustrates the isofrequency contour of the polariton. For the depicted case at an azimuthal angle of $\varphi = 30°$, momentum matching can be achieved for $m = -1$ and $n = 0$.

Thus, the rotation of the sample gives access to a range of polariton momenta for different frequencies. This makes it possible to measure different parts of the polariton dispersion, by recording spectra at different azimuthal angles, see Fig. 8.3(c). The violet graph (lowest plot) shows the spectrum for the unrotated sample, where two main peaks are apparent at roughly $\omega_\mathrm{IR} = 880\,\mathrm{cm}^{-1}$ and $\omega_\mathrm{IR} = 905\,\mathrm{cm}^{-1}$ corresponding to the upper polariton branch and the dipolar mode, respectively. The sample rotation leads to a blue shift of the resonance peaks, and also gives access to the lower polariton branch, which could not be excited in the unrotated sample. These spectra can be used to map out the dispersion of the hybridized polaritons, as shown in Fig. 8.3(d). The black solid lines depict the analytical model, as was used in Fig. 8.2, and match the measured data excellently. In comparison to the simulations, the spectral width of the hybridized polaritonic resonances is larger, which could be caused by local disorders in the lattice, distributions of φ and ϑ due to mild focusing of the IR laser or due to the IR laser's bandwidth ($\approx 0.6\,\%$). The x-axis is also gives the wavevectors (top x-axis) according to Eq. (8.2.2) with $m = -1$ and $n = 0$ for better comparison to the simulation in Fig. 8.2.

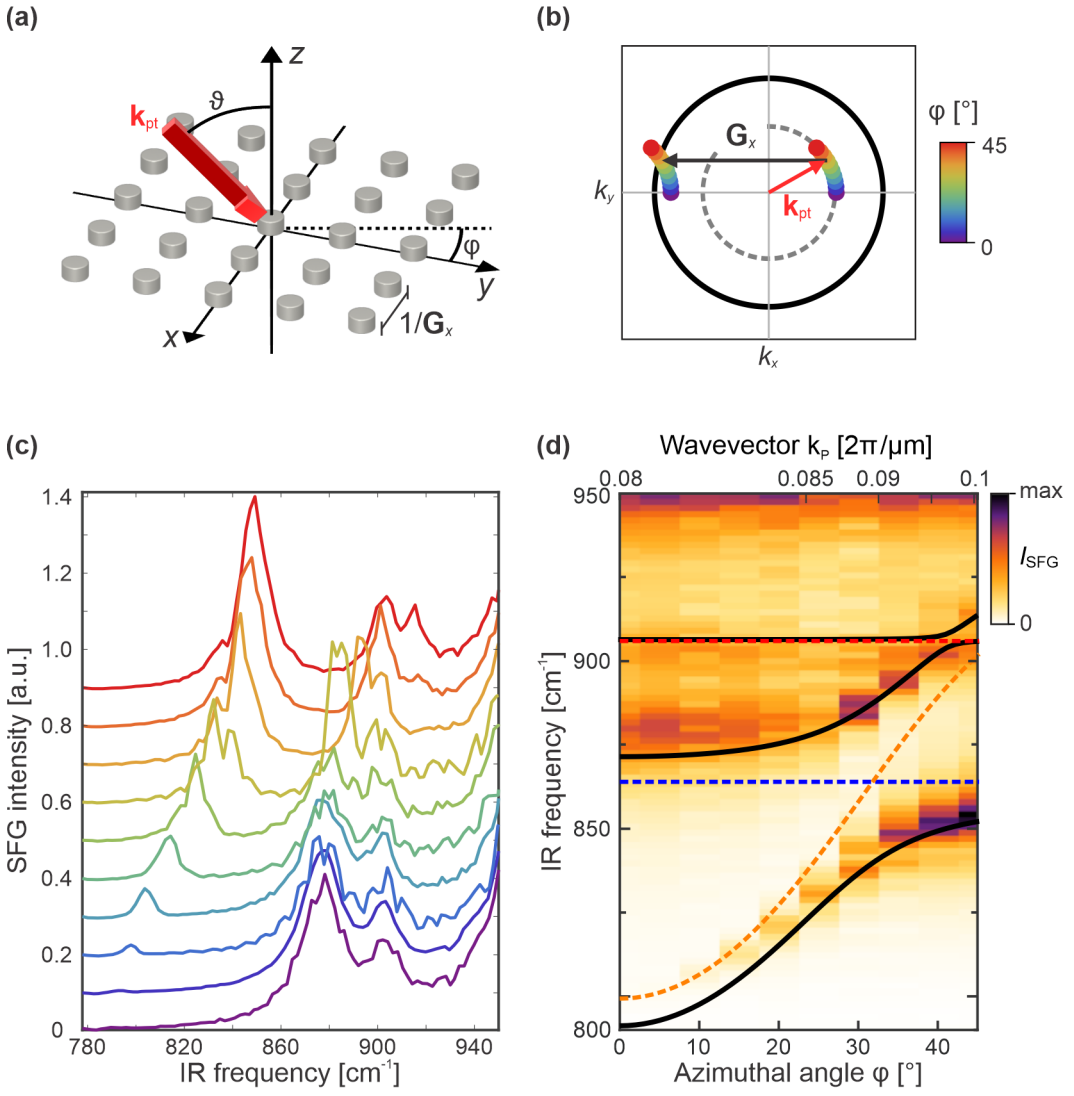

Figure 8.3. *Experimental dispersion of a SiC metasurface using SFG spectro-microscopy.* (a) Sketch of azimuthal sample rotation with angle φ and IR incidence angle ϑ. (b) Isofrequency contour of hybridized surface polariton (black). A polariton can be excited through momentum matching of the incident light $\mathbf{k}_{\mathrm{pt}}$ with a reciprocal lattice vector $\mathbf{G}_{\mathrm{x}}$ for a specific incidence angle φ. (c) SFG spectra for different azimuthal angles $\varphi = 0\,\mathrm{to}\,45°$ (colorcode as in (b)). (d) Dispersion of hybridized polaritons measured by azimuthal sample rotation. Spectra were measured in 5° steps. Dashed and solid lines belong to the uncoupled resonances and the calculated hybridized polariton dispersions as in Fig. 8.2, respectively.

As can be seen in Fig. 8.3(d), the avoided crossing between the dipole frequency and the SPhP dispersion cannot be resolved anymore. In contrast, the anti-crossing of the monopolar resonance and the SPhP dispersion is very clearly observed and is clearly within the strong coupling regime with $g_1 = 24\,\mathrm{cm}^{-1} > (\gamma_{\mathrm{M}} + \gamma_{\mathrm{SPhP}})/2 = (9.0\,\mathrm{cm}^{-1} + 7.9\,\mathrm{cm}^{-1})/2 \approx 8.5\,\mathrm{cm}^{-1}$. The linewidths γ_{M} and γ_{SPhP} belong to the uncoupled states, and were measured previously using thermal emission spectroscopy [62].

8.3 Dispersion from interferometric imaging

In addition to resonance imaging at different rotation angles, the hybridized polariton dispersion can also be measured with interferometry of propagating polaritons. Even at off-resonant conditions ($\varphi = 0$), when no momentum matching is provided, a finite SFG signal can be detected, see Fig. 8.4(a). Interestingly, the SFG intensity varies with position and shows vertical fringes close to the edge of the metasurface. These fringes become more clear in linescans extracted by vertical integration of the images, shown in Fig. 8.4(b). The fringes occur perpendicular to the IR incidence direction, and parallel to the metasurface edge, with decreasing amplitude away from the edge. This observation leads to the assumption that propagating polariton waves are launched by the edge of the micropillar array with a fringe period as well as the propagation length strongly dependent on the excitation frequency of the IR laser, see Fig. 8.4(b).

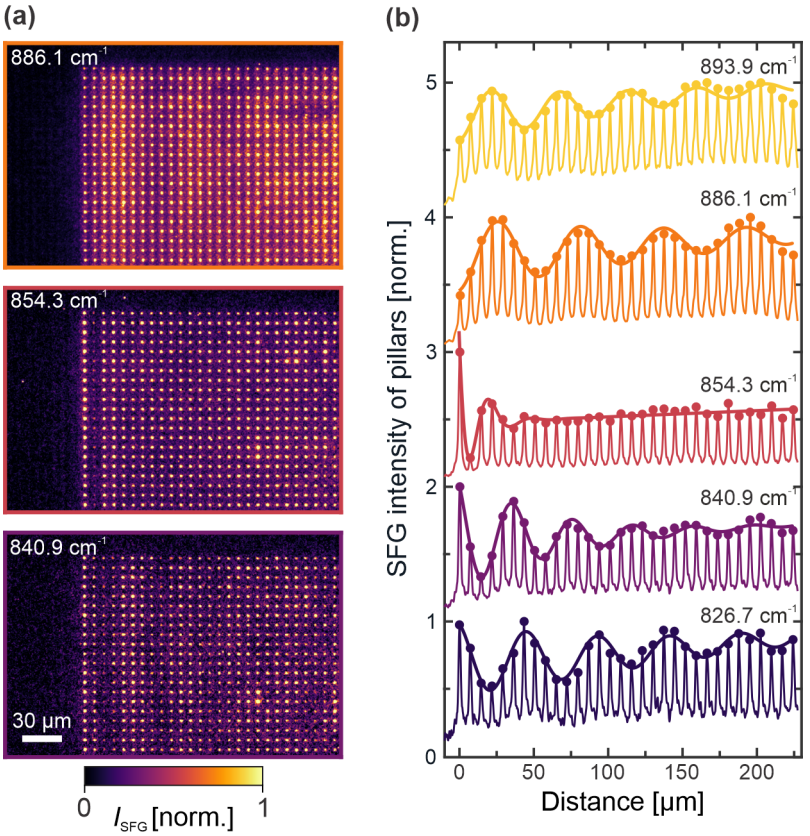

Figure 8.4. *SFG images and line scans of propagating SPhP waves along the SiC surface.* (a) SFG intensity images for different frequencies. Scale bar is 30 µm. (b) Line scans of propagating polaritons by vertically integrating over the images. Dots represent the pillars and lines represent the SFG intensity. Bold solid lines show the corresponding fit according to Eq. (8.3.1).

The fringes can be modeled by assuming that a propagating polariton launched at the edge of the pillar array interferes with the incident IR laser field, illustrated in Fig. 8.5. This model is similar to the discussion in Chapter 6 or to the interpretation of inference fringes in s-SNOM images [137].

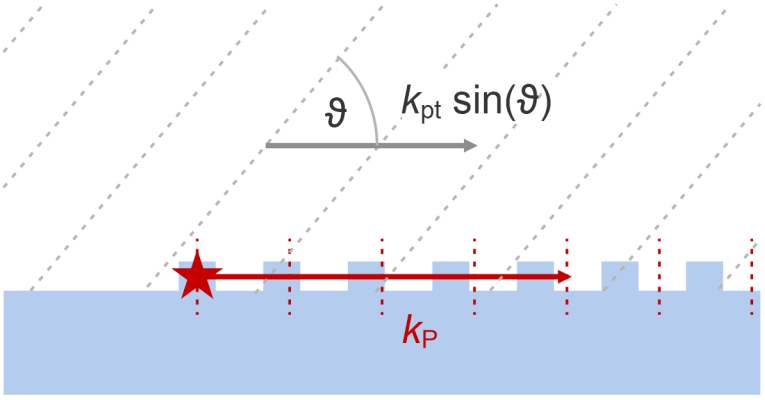

Figure 8.5. *Sketch of interference of propagating SPhP and incoming IR beam.* Propagating waves occur due to edge launching of the edge pillars and interfere with the incoming IR beam. Dashed lines show wave fronts of SPhP (red) and IR beam (gray).

The spatial modulation of the observed SFG intensity along the micropillar array can be fit with

$$I(x) = |\underbrace{Ae^{ik_P x + i\xi}}_{\text{polariton}} + \underbrace{Be^{ik_{pt}\sin\vartheta x}}_{\text{photon}}|^2 + \underbrace{I_0 + I_1 x}_{\text{background}}, \tag{8.3.1}$$

with the complex polariton wavenumber k_P, a phase shift ξ, the amplitudes A and B for the polariton and photon waves, respectively, and an additional linear background. The fit is applied to the data shown in Fig. 8.4 where it is depicted as thick solid lines on top of the line scans and gives a good match with the measured data. From the fit, the wavenumber k_P can be extracted, which relates to the fringe period as $\Lambda_x = 2\pi/[\Re(k_P) - k_{pt}\sin\vartheta]$. Λ_x is much larger than the actual polariton wavelength λ_P which is expected for polaritons in co-propagation with the incoming photons (see also discussion in Sec. 8.3.1). In the case of launching by the top edge, perpendicular to the direction of incoming IR light, the IR light would not affect the fringe period leading to $\Lambda_y = \lambda_P$. This scenario is apparently far less efficient and not observed in the SFG images.

By extraction of $\Re[k_P(\omega)]$ from the fit, the analysis of the interference patterns for different IR frequencies provides a second complementary approach to measure the hybridized polariton dispersion. The results are plotted in Fig. 8.6(a), where again the data points match the analytically calculated dispersion (black lines) nicely. Thus, the dispersion measured with this interferometric approach is in excellent agreement with the dispersion from resonant imaging (Fig. 8.3) although it was extracted using a completely different method: in Sec. 8.2, the complex polariton frequency $\omega_P(k)$ was probed for real wavevectors k originating from the phase matching by a reciprocal lattice vector. The interferometric imaging discussed here probes the complex polariton wavevector $k_P(\omega)$ for real frequencies ω set by the

IR laser.[9] The good agreement of both approaches is noteworthy since complex wavevector dispersions, as measured here, typically feature a backbending instead of an anti-crossing [170, 171].

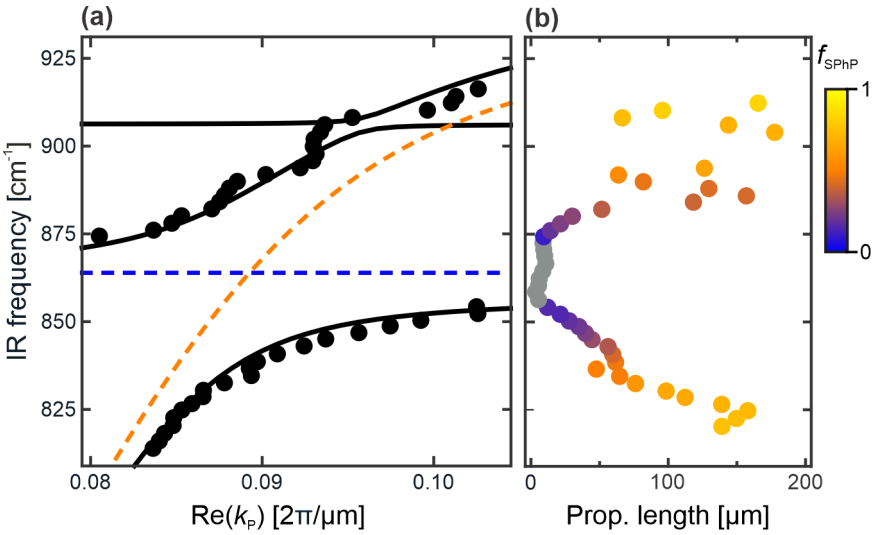

Figure 8.6. *Measured dispersion and propagation length of propagating SPhPs from interferometric imaging.* (a) Dispersion of the hybridized polaritons extracted from a fit of interference fringes with Eq. 8.3.1. (b) Corresponding propagation lengths $d_P = 1/\Im(k_P)$. The colorcode shows mixing fraction of propagating and localized polaritons with 1 = 100 % propagating character and 0 completely localized character.

Besides the dispersion, the polariton propagation length can be extracted from the fit by $d_P = 1/\Im(k_P)$ which is plotted in Fig. 8.6(b). It ranges from $d_P > 150\,\mu$m to close to 0 in the strong coupling gap, and is highly dependent on the IR frequency. These drastic changes can be explained from the hybridization of propagating SPhPs with the localized monopolar resonance of the pillars. The corresponding mixing fraction f_{SPhP} gives the proportion of propagating SPhP character in the hybridized polaritons (color code in Fig. 8.6(b)). It can be calculated using a two-mode coupled-oscillator model as

$$\begin{pmatrix} f_{SPhP,\pm}(k) \\ f_{M,\pm}(k) \end{pmatrix} = \text{eigvec}\left[\begin{pmatrix} \omega_{SPhP}(k) & g \\ g & \omega_M \end{pmatrix}\right]^2, \tag{8.3.2}$$

with $f_{SPhP,\pm}$ the SPhP population fraction and $f_{M,\pm}$ the monopole fraction, respectively, with the indices '+' for the upper polariton branch and '−' for the lower polariton branch. In the analytic expression, $f_{SPhP,\pm}$ reads

$$f_{SPhP,\pm}(k) = \left[\omega_M - \omega_{SPhP}(k) \pm \sqrt{4g^2 + (\omega_M - \omega_{SPhP}(k))^2}\right]^2 / 4g^2, \tag{8.3.3}$$

[9] The complex polariton frequency ω_P was determined through spectroscopic linewidths, where the imaginary part is given by the losses to the system. The complex wavenumber k_P can be determined by the real part originating from the periodicity of the polaritonic waves and extracting the imaginary part from the corresponding propagation lengths.

and $f_{\mathrm{M},\pm} = 1 - f_{\mathrm{SPhP},\pm}$.

Indeed, the measured propagation length of the hybridized polaritons scales with f_{SPhP}. Polaritons close to the resonance frequency ω_{M} of the localized monopolar mode only have a small, close to zero, proportion of propagating SPhP character, giving rise to a mainly localized character with a very short propagation length. Contrarily, polaritons with a large detuning from ω_{M} are mainly of propagating SPhP character and accordingly have a large propagation length. The polaritons of the lower branch have a mixing fraction varying in the range $f_{\mathrm{SPhP}} = 80\,\%$ to $15\,\%$ indicating a nearly complete inversion in polaritonic character. In the band gap, originating from the avoided crossing of the lower and upper polariton branches, propagation into the metasurface is forbidden, hence the hybridized polaritons are completely localized (Fig. 8.6(e), gray).

8.3.1 Polariton interferometry for different propagation directions

So far, only interference images of polaritons co-propagating with the IR photons were analyzed. However, interference fringes are also observed at the opposite edge of the metasurface. Example SFG images at $\omega_{\mathrm{IR}} = 826\,\mathrm{cm}^{-1}$ are shown in Fig. 8.7.

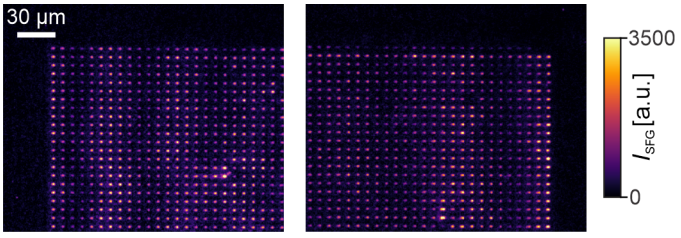

Figure 8.7. *SFG images of propagating waves of co- and counter-propagating polaritons and photons launched off the left and right edge of the metasurface.* Both edges launch propagating waves with the fringe period for the right edge slightly larger than the left-edge. Images taken at $\omega_{\mathrm{IR}} = 826\,\mathrm{cm}^{-1}$.

Fig. 8.8(a) shows the experimentally observed interference patterns with propagating waves on the substrate launched by left and right edge, respectively. The data points show the SFG intensity, after vertical integration over the whole SFG image, with a fit indicated by the solid line. It is striking that both sides launch waves with comparably similar fringe periods. For the left-edge launching, the detected wave is the interference of two co-propagating waves, while the waves are counter-propagating for the right-edge launched case. In Chapter 6, it was shown and discussed that fringes from counter-propagating waves have a much smaller fringe spacing than those from co-propagating waves. This behavior does not appear to be observed here.

A theoretical model based on the analytic polariton dispersion shown in Fig. 8.6(a) leads to the expected behavior with two very different fringe periods according to $\Lambda_{\mathrm{co}} = 2\pi/(\mathrm{Re}[k_{\mathrm{P}}] - k_{\mathrm{pt}} \sin\vartheta)$ and $\Lambda_{\mathrm{counter}} = 2\pi/(\mathrm{Re}[k_{\mathrm{P}}] + k_{\mathrm{pt}} \sin\vartheta)$, illustrated in Fig. 8.8(b).

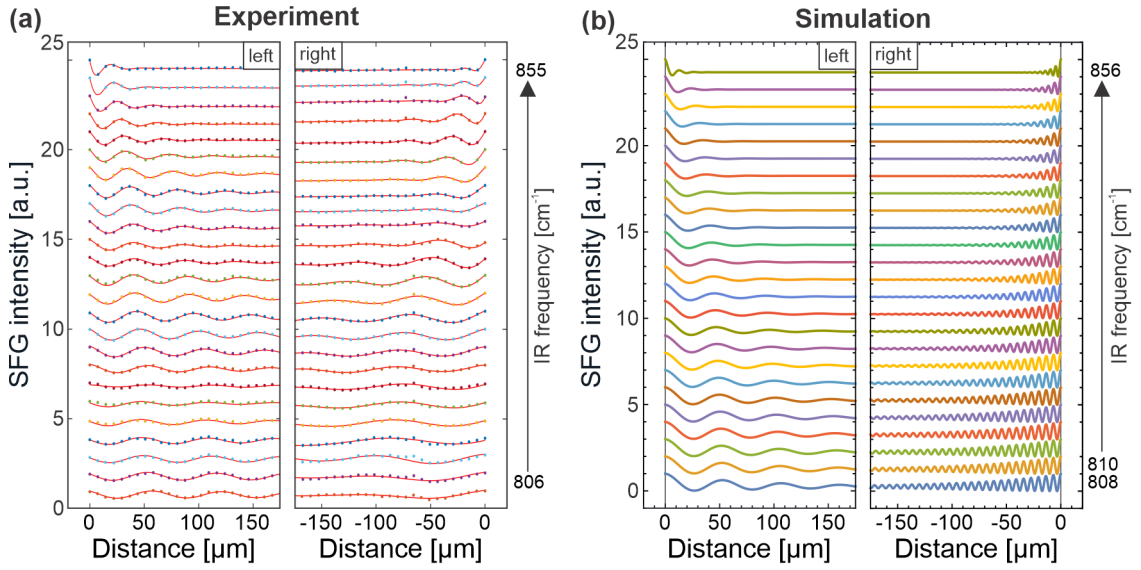

Figure 8.8. *Interference patterns from polaritons launched by left vs right edge.* (a) Experimental SFG intensity (data points) at the positions of the pillars from vertical integration of the SFG image. Solid lines are a fit. Left- and right-edge launched propagating waves have a comparable fringe period. (b) Theoretical model, calculated with Eq. (8.3.1) with the dispersion from Fig. 8.6(a) as input parameter. The right-edge launched propagating wave has a much smaller fringe period compared to the left-edge launched wave.

The observed mismatch can be explained with the lattice structure of the sample. When evaluating the interference intensity, the information is obtained only at the positions of the pillars, which have a much larger periodicity than the calculated fringe period of the counter-propagating interference wave. Thus, the imaged interference pattern is undersampled.

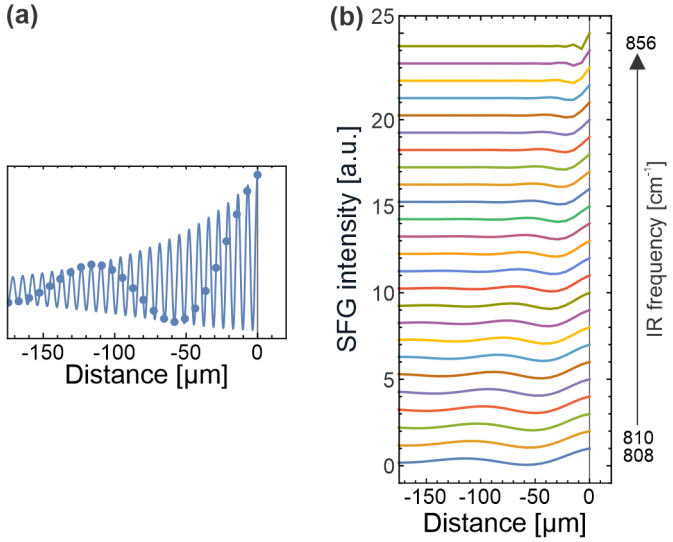

Figure 8.9. *Undersampling of interference pattern.* (a) Due to the difference in lattice constant (pillars illustrated as dots) and much smaller fringe period, the read out undersamples the actual interference pattern (solid line). (b) Connecting the dots in (a) leads to a much larger fringe period.

Fig. 8.9(a) illustrates the case of undersampling, where the solid line shows the actual

fringe period and the dots show the pillar positions. When connecting the dots with a line, the resulting theoretical fringe period is in good agreement with the experimentally observed data (Fig. 8.8(a,right)).

8.4 Polaritonic edge states in strong coupling gap

The complete localization of hybridized polaritons in the strong-coupling gap gives rise to polaritonic edge states. An example SFG image with $\omega_{\mathrm{IR}} = 854.6\,\mathrm{cm}^{-1}$ is shown in Fig. 8.10, where the SFG intensity is largest at the edge of the micropillar array. A weak excitation of the pillars inside the metasurface is visible, due to the proximity to the upper polariton branch at $\omega_{\mathrm{P}}\,(\varphi = 0) \approx 880\,\mathrm{cm}^{-1}$.

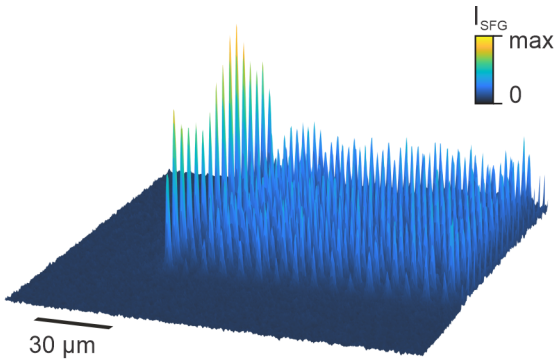

Figure 8.10. *3D-SFG intensity image of an edge state at* $\omega = 854.3\,cm^{-1}$.

In the angular polariton dispersion, an edge state appears as an additional resonance from resonant imaging for small rotations φ, when evaluating the SFG intensity not for the whole array, but only for the edge pillars (see magenta box in Fig. 8.11(a)). This is shown in Fig. 8.11(b), where direct comparison between the polariton dispersion plots for inside pillars and edge pillars reveals the additional resonance (also highlighted by a magenta box). A resonance occurs at $\omega_{\mathrm{edge}} = 860\,\mathrm{cm}^{-1}$ in the polaritonic band gap between upper and lower polariton branch without any frequency dependence on the azimuthal angle φ. The interplay of the two resonances leads to strong variation of the ratio of the metasurface edge and metasurface inside SFG intensities $I_{\mathrm{edge}}/I_{\mathrm{inside}}$ as a function of the IR frequency, especially in the strong-coupling gap, see Fig. 8.11(c). In the lower frequency region of the strong-coupling gap, close to the lower polariton branch, the edge intensity increases with respect to the entire metasurface. With increasing IR frequency, this behavior transitions to a decrease in intensity at the upper polariton branch. The maximum intensity ratio is reached at $\omega_{\mathrm{IR}} \approx 855\,\mathrm{cm}^{-1}$ and hence red shifted with respect to the edge-state frequency ω_{edge}.

In general, the excitation of the edge state is most efficient for $\varphi = 0°$. With increasing angle φ, the edge SFG intensity decreases and vanishes completely for $\varphi > 25°$. Hence, an interface perpendicular to the incident photons is needed for efficient excitation of edge states.

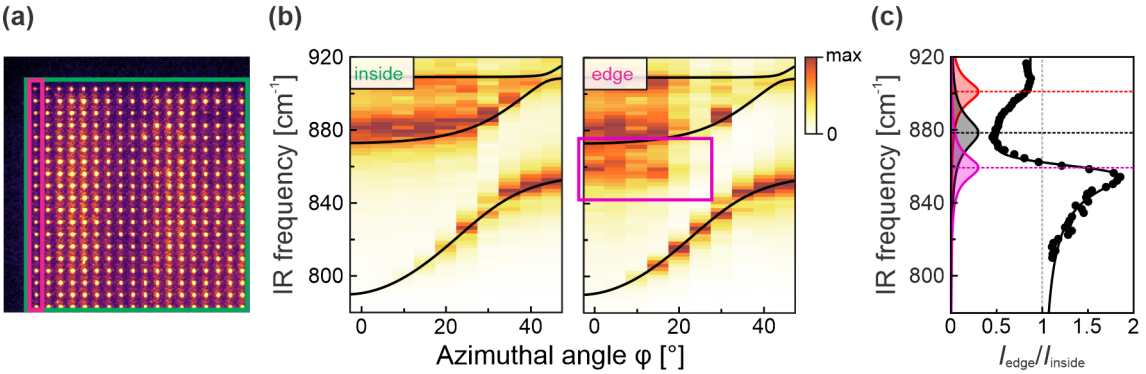

Figure 8.11. *Dispersion of metasurface inside and edge.* (a) SFG image with boxes highlighting the metasurface edge (magenta) and the metasurface inside (green). (b) Dispersion of entire metasurface (left) and edge pillars (right) with appearance of an additional edge state (magenta box). (c) Ratio of average SFG intensity of edge pillars I_{edge} and metasurface inside I_{inside} as function of IR frequency. The black solid line is a fit of an analytic model with three oscillators: edge state (magenta), upper polariton (black), and dipole mode (red).

A closer look at Fig. 8.10 reveals a wave pattern in the SFG intensity along the pillar edge. This wave pattern resembles the previously observed interference of propagating polaritons but along the edge instead of propagation across the entire metasurface. This propagation direction makes sense because the excitation frequency $\omega_{\mathrm{IR}} \approx 855\,\mathrm{cm}^{-1}$ is in the band gap between the upper and lower polariton branch. Here, propagation across the metasurface is physically forbidden but allowed along the metasurface edges. The observation has to be further validated in the future, to investigate whether the wave pattern belongs to a propagating edge wave which could be, e.g., launched at the corner. So far, coincidental interference due to lattice defects or IR beam profile imperfections is excluded because the pattern is only apparent in the edge pillars and not observable across the entire metasurface.

8.5 Discussion and Outlook

The technique of SFG spectro-microscopy enables the simultaneous measurement of polariton dispersions via interferometric imaging, as is often used in s-SNOM, as well as resonant spectral imaging, as used in nano-FTIR and reflection spectroscopy. In addition to the polariton dispersion, the propagation length of hybridized polaritons can also be analyzed, providing details on their polaritonic character. Due to the large FoV of the wide-field microscope, the approach is especially powerful for imaging of metasurfaces, where polaritons propagate over distances larger than 100 µm, and have near-fields confined to sub-µm mode-volumes of the individual microstructures at the same time.
Due to the IR sub-diffractional spatial resolution on the order of the micropillar sizes, localizations of polaritons to the edges of the arrays for frequencies inside the polaritonic band gap could be spatially resolved. The results clearly show that strong

coupling is not only a spectral feature but also has pronounced effects on polariton propagation and can lead to the activation of new states.

Beyond the strong coupling between localized and propagating polaritons, recent publications deal with the coupling of either of these modes with organic molecules [60, 61, 172]. The resulting vibrational strong coupling enables higher sensitivity in the monitoring of molecules [61] or local control of chemical properties [173, 174]. With its applicability to localized and propagating polaritons, the technique of SFG spectro-microscopy will be a useful far-field technique for imaging the hybridization between molecular vibrations and phonon polaritons in both structured and unstructured materials.
Furthermore, SFG spectro-microscopy will be an interesting approach to image topological structures, where polaritonic or photonic states are spatially confined to domain boundaries [64]. These states can be launched controllably into different directions by circular polarized light, making topological structures interesting for many applications [64, 175, 176]. However, imaging of such states has so far been challenging due to a limited spatial resolution offered by infrared microscopes and the limited spectral range of current near-field techniques [64, 177].
SFG spectro-microscopy thus extends the toolbox of imaging techniques with high spatial resolution applicable to a broad spectral range, offering detailed spectral and spatial information, while maintaining short acquisition times and a non-perturbative character.

9

Observation of Phonon Polariton Standing Waves in SiC Microrods

The occurence of standing waves in SiC microrods written onto a SiC substrate shall be discussed in the following chapter. After introducing the microrod geometry, Sec. 9.1 reports on the observation of standing waves, followed by a discussion of the excitation frequency dependence. A comparison is made between the results for SFG spectro-microscopy as a far-field technique and results of nano-FTIR as a near-field technique as well as to respective simulations. Thereafter, the role of the resonator geometry on the standing waves is discussed. Finally, the microrod as a launcher for propagating polaritons is discussed in Sec. 9.2 with a short outlook on future experiments.

The last chapters dealt with localized and hybridized modes in 1D and 2D lattices of SiC micropillars. The sizes of the individual micropillars were small compared to the incident IR wavelengths, leading to localized resonances at fixed IR wavelengths. In the following, larger rod-shaped microresonators with a length comparable to the IR wavelength will be considered. Structures with rectangular, rod-like shapes have been shown to support polaritonic standing waves similar to those observed in Fabry-Pérot cavities. These polaritonic standing waves are supported in a variety of metallic and dielectric materials, enabling control over mode profiles and resonances by, e.g., changing the aspect ratio of the rods [178–183]. Experiments have been performed on individual rods placed on substrates of different materials featuring plasmonic [178–180], as well as phonon-polaritonic [182, 183] resonances. So far, research is lacking experimental data on standing waves in rods on a substrate of the same material, where substrate-coupling is apparent. Several publications [57, 59, 184] discuss nanoresonator arrays in the form of cylindrical pillars made of 4H-SiC on the same substrate, supporting through-substrate coupling of PhPs, offering the ability of resonance tuning via parameter changes [59, 185]. Considering this coupling mechanism between the resonators and the substrate, it is not clear to what extent localized modes and standing waves are supported in individual substrate-coupled microrods, or if the confinement of light is suppressed by leakage into the substrate.

In the following, phonon polaritons of 4H-SiC microrods on a 4H-SiC substrate are discussed. Fig. 9.1 shows an SEM image of the sample. Different patterns have been created for rod widths of 0.4 µm, 1 µm and 2 µm with a constant height of 1 µm.

The rod length varies from 1 µm to 20 µm with roughly ±0.2 µm tolerance on each rod. Similar to the SiC micropillars, the rods have been fabricated using e-beam lithography.

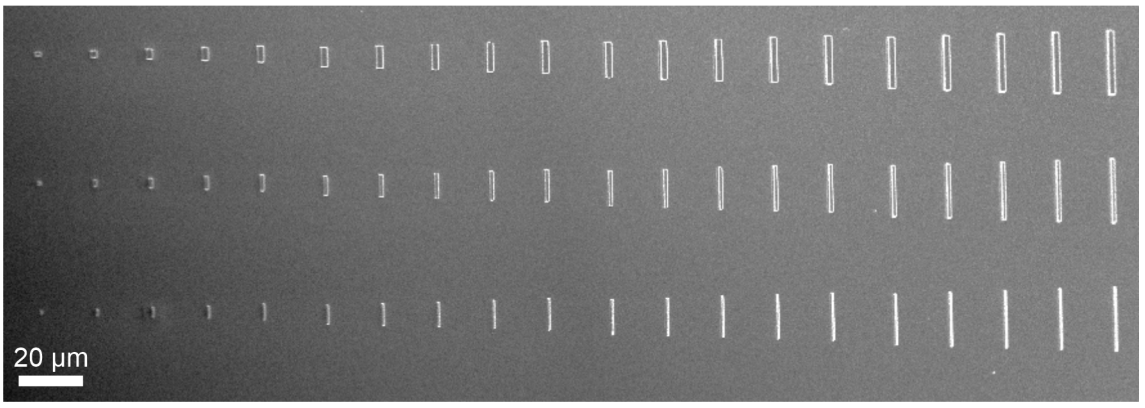

Figure 9.1. *4H-SiC microrods.* SEM image of microrods under a view angle of 30° from the left with lengths varying between 1-20 µm and widths of 0.4, 1, and 2 µm from bottom to top.

To observe polaritonic standing waves, SFG microscopy and s-SNOM/nano-FTIR[10] (nano-Fourier transform infrared) spectroscopy have been used to achieve both microscopic images and spectroscopic dispersion information. The results of the different techniques will be compared with simulations (*COMSOL multiphysics 5.6*), using plane-wave illumination, corresponding to the SFG microscopy experiments, and a point-dipole source located 100 nm above the microrod for the s-SNOM measurements.

9.1 Polariton standing waves

To experimentally test the IR response of SiC microrods on a substrate of the same material, images for frequencies within the Reststrahlen band of SiC have been recorded with SFG microscopy and s-SNOM. Example images from both methods are shown in Fig. 9.2(a) and (c), where the rods were illuminated from the left side with p-polarized IR light. The analyzed rods have a length of 8 µm and a width of 0.4 µm. As shown in the microscopic images, clear maxima are visible along the microrod that correspond to standing wave modes. With increasing IR frequency excitation, the resulting PhP wavelength is reduced, increasing the number of maxima inside the rod.
As visible in the SFG images in Fig. 9.2(a), at a frequency of $\omega_{\mathrm{IR}} = 873\,\mathrm{cm}^{-1}$, the wavelength is sufficiently large to support only a single polariton wavelength inside the rod, with a maximum located in the middle of the rod (left panel of (a)). By

[10] *Neaspec* setup with a conventional metal-coated tip. Nano-FTIR is realized by combining s-SNOM with FTIR-based detection. The tip tapping frequency was set to approx. 270 kHz, and the tip tapping amplitude was set to approx. 60 nm. Images and spectra were recorded with an integration time of 10 ms per pixel, and each spectrum has a resolution of $6.25\,\mathrm{cm}^{-1}$. Measurements of the results presented within this chapter were conducted by collaborators at Vanderbilt University.

increasing the IR frequency, the occurrence of additional maxima inside the rod indicates an increase in the standing wave order (middle and right panel in (a)). These results are compared to numerical simulations using plane-wave excitation, see Fig. 9.2(b). The corresponding images show the z-integrated E_z-field intensity across the microrod. The simulation shows a similar behavior to that of the SFG measurements. The intensity in the simulations is more pronounced on the left side of the rods, though, which can be explained with the left side of the rod facing the illuminating IR light, therefore leading to a stronger intensity at this side. In the microscope images, the spatial resolution is not high enough to distinguish between left and right side of the rods.

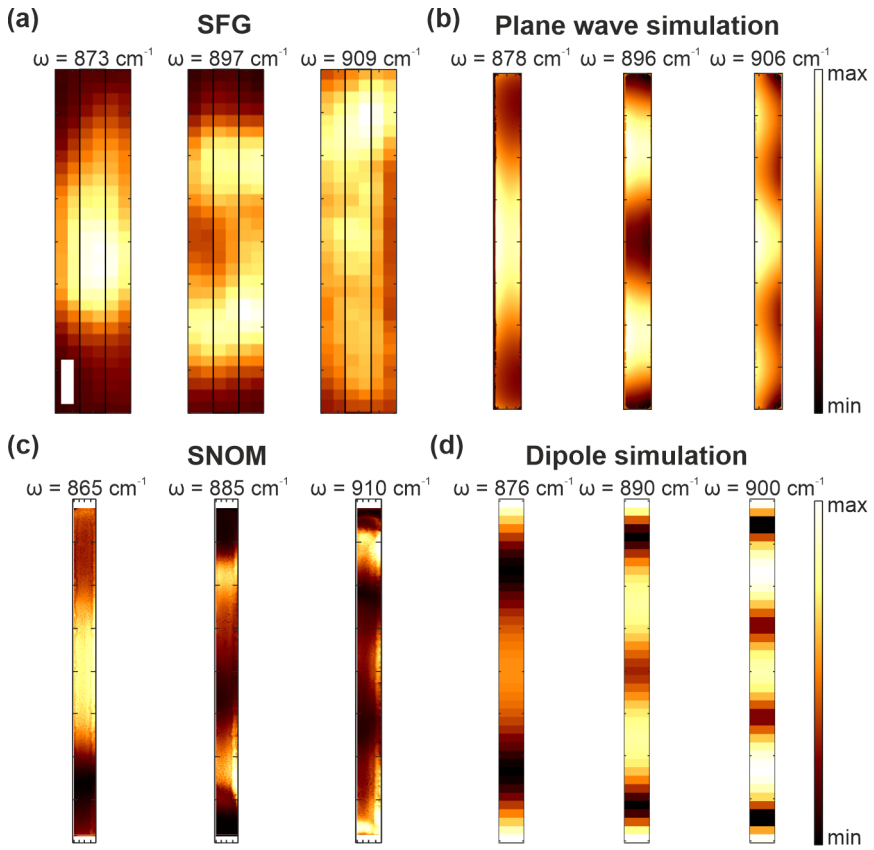

Figure 9.2. *Standing waves in SiC microrods.* a) SFG microscopy images of an individual SiC microrod (w = 0.4 µm, l = 8 µm) at different excitation frequencies showing one, two, and three intensity maxima from left to right. The black box illustrates the actual rod width and the white scale bar corresponds to 1 µm and is valid for all panels. b) Corresponding COMSOL simulations with plane-wave excitation showing the E_z-field intensity. c) s-SNOM images at different frequencies showing the different mode orders from left to right. d) Corresponding COMSOL simulations with dipole excitation showing the E_z-field intensity calculated in the center of the rod. The dipole was placed 100 nm above the rod and the field was detected 50 nm above the rod.

While the PhP resonances are observed from the far-field using SFG microscopy, they also can be excited using a near-field method like s-SNOM. Here, a metallic AFM tip is used as a local antenna and excites and detects the local electric field. While the excitation and detection mechanisms are clearly different for the two methods, comparable images for the same 4H-SiC microrod are observed. In the s-SNOM

images in Fig. 9.2(c), the number of intensity maxima increases with increasing IR frequency, and the outer maxima move towards the ends of the rod, as observed in the SFG images. The near-field results are further compared to numerical simulations using a scanning point-dipole excitation, where the dipole was placed 100 nm above the rod and scanned along the axis of the microrod. The field was evaluated 50 nm above the microrod for each point and shows comparable distributions as shown in Fig. 9.2(d).

9.1.1 Spatio-spectral response of microrods

To extend this analysis, the response of the rods across the whole spectral range of the SiC Reststrahlen band was measured. To compare the optical responses measured with the different experimental techniques and the corresponding numerical simulations, the results are plotted in spectro-spatial dispersion plots, Fig. 9.3. The plots show the measured (a,c) and simulated (b,d) intensity along the rod length (y-axis) as a function of the IR excitation frequency (x-axis). For each IR frequency, the optical response along the microrod as, e.g., in Fig. 9.2 for three IR frequencies corresponding to standing wave resonances, is plotted.

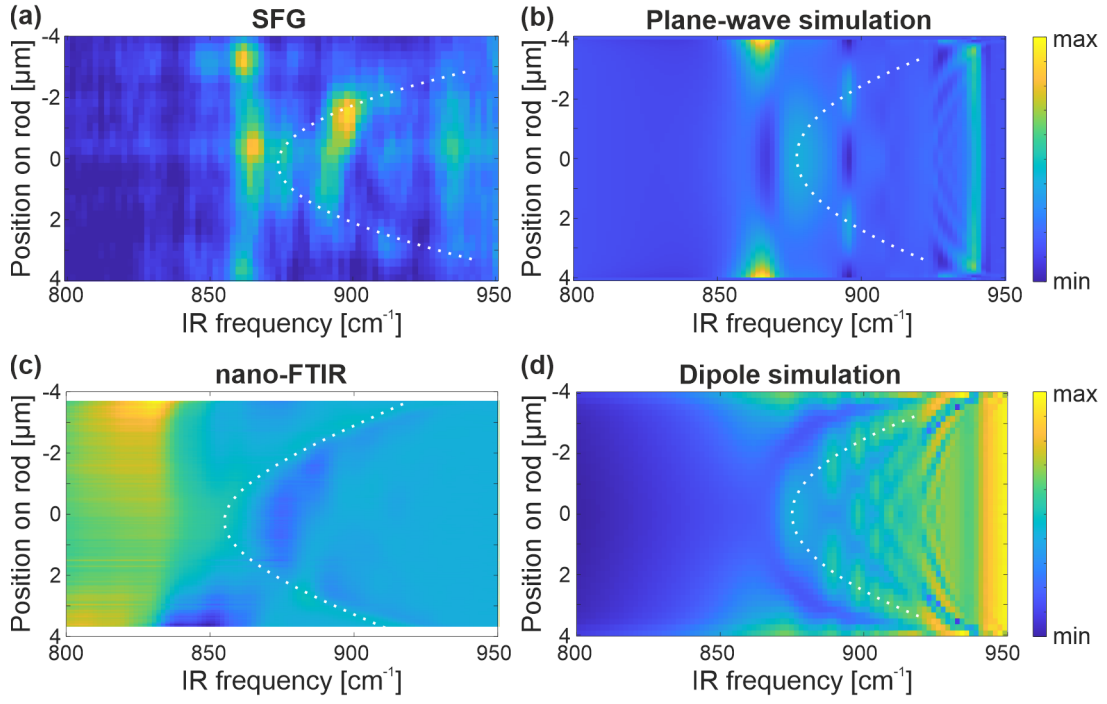

Figure 9.3. *Spatio-spectral response of SiC microrods.* (a) Spatio-spectral dispersion plot (intensity profile along the long axis of the rod at center of short axis vs. IR frequency) of the SFG microscopy measurements. (b) Dispersion of the simulated E_z-field with plane-wave illumination. (c) nano-FTIR dispersion measured along the length of the rod. (d) Dispersion of the simulated E_z-field with dipole excitation. White dots are lines to guide the eye for the dispersive region.

At $\omega_{IR} = 860\,\mathrm{cm}^{-1}$, an excitation of the rod edges is apparent for the SFG microscopy data, Fig. 9.3(a), in good agreement with the simulations, Fig. 9.3(b+d).

At higher wavelengths, $\omega_{\mathrm{IR}} \gtrsim 875\,\mathrm{cm}^{-1}$, the standing waves can be observed. The frequency range fits well with the extracted first standing wave modes in the images in Fig. 9.2(a). The outermost maxima of the standing wave modes are highlighted with a white dotted line to guide the eye. The comparison with the simulated data shows good agreement with the dispersive region for $\omega_{\mathrm{IR}} \gtrsim 875\,\mathrm{cm}^{-1}$ in the plane-wave simulation as well.

The spatio-spectral response measured by near-field spectroscopy (nano-FTIR), see Fig. 9.3(c), also shows the dispersive branching similar to the SFG microscopy results. However, the dispersive region of the near-field results is stretched compared to the far-field data starting at $\omega_{\mathrm{IR}} \gtrsim 860\,\mathrm{cm}^{-1}$. The comparison to the simulation shows a similar dispersive behavior again with a small blue shift of $\approx 15\,\mathrm{cm}^{-1}$ in the point-dipole simulation results with respect to the nano-FTIR data. By comparison of all four methods, only the nano-FTIR shows a noticeable difference for the lowest-order standing-wave frequency. This difference can be attributed tentatively to the different excitation and detection mechanisms in the near- and far-field methods as well as to the sample-tip interaction in nano-FTIR. Additionally, a discretized dispersion is obvious in the simulated results as well as in the SFG microscopy data. The nano-FTIR data, however, does not show a discrete behavior but a continuous mode. Further emphasis has to be put on this mismatch in future work, a first tentative explanation might be the difference in launching where the standing waves are launched by the edges of the rod in the far-field approach, but by the AFM-tip away from the edges in the nano-FTIR.

9.1.2 Role of resonator geometry

To analyze the microscopic origin of the deviations between far- and near-field excitation in the measurements, further experiments are needed. One possible approach is the exploration of the mode behavior for different lengths of the rod. While keeping the rod width constant, the optical response for different rod lengths, i.e., 8, 12 and 14 µm, is analyzed. The results are shown in Fig. 9.4. Here, the panels (a-c) illustrate the far-field excitation response as measured by the SFG microscope, while the panels (d-f) show the near-field excitation optical response by nano-FTIR spectroscopy. The white, horizontal lines in panels (a-c) illustrate the rod length.

The data from both techniques show similar behavior of a red-shift for the lower edge of the dispersive region (see area highlighted with dotted line) with increasing rod length, while the upper edge remains unaffected. Thus, the dispersive region's bandwidth changes depending on the rod length. The observed red-shift can be explained by the SPhP wavelength. The first-order mode, e.g., Fig. 9.2(a,left), of a longer rod corresponds to a larger spacing between the maxima of the standing wave: To match the resonance frequency for a standing wave with one pole, the wavelength of the propagating polariton has to become larger, thus leading to a shift to lower frequencies.

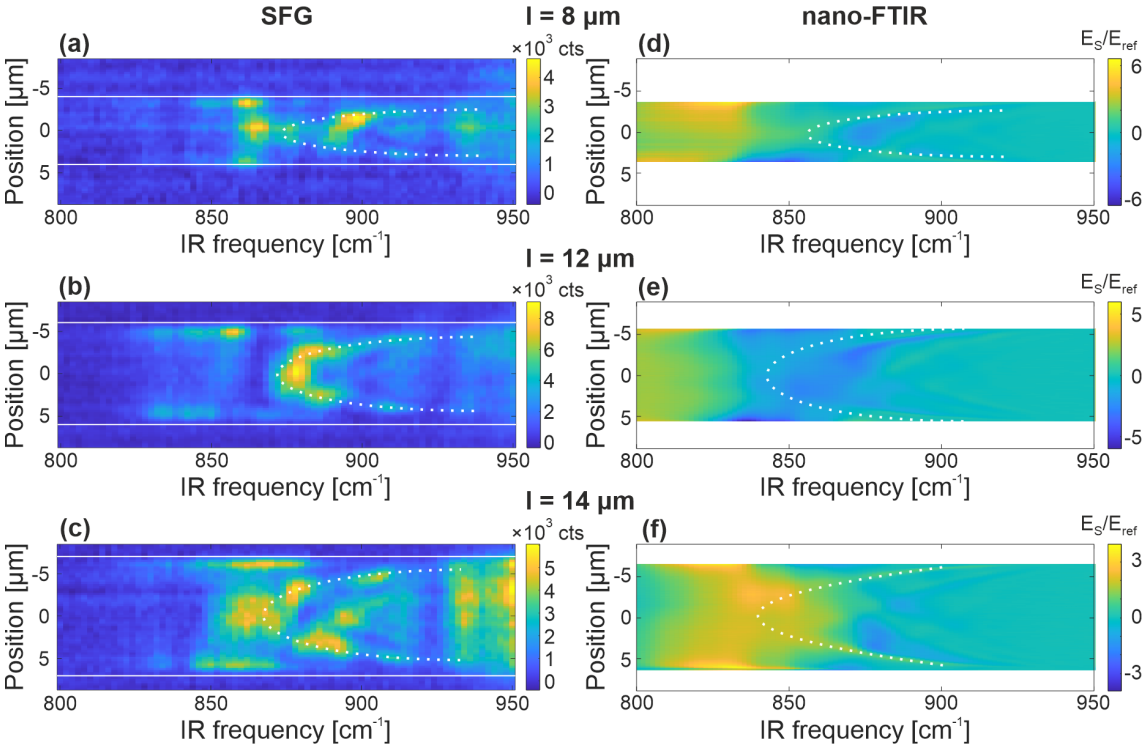

Figure 9.4. *Effect of SiC rod length on standing waves.* (a–c) SFG dispersion of rods with different lengths of $l = 8\,\mu\text{m}$, $l = 12\,\mu\text{m}$, and $l = 14\,\mu\text{m}$ and a constant width of $w = 0.4\,\mu\text{m}$, respectively. The white lines show the nominal length of the microrods. (d–f) nano-FTIR measurements along the rod length of the same SiC microrods. The nano-FTIR scans were acquired on the flat surface on top of the microrods.

9.2 Outlook: Microrods as launcher for propgating polaritons

Focusing not on the microrods themselves but on the optical response of the substrate reveals that the rods act as excellent launchers for propagating waves on the substrate. Similarly to the discussion in Chapter 6, the polaritons are launched along the long edge of the rod and propagate in $\pm x$ direction towards neighboring rods. Depending on the IR wavelength, the propagation length and mode intensity changes, as depicted in Fig. 9.5, and interference between waves launched by neighboring edges can be observed. Hence, standing waves are not only observable inside the rod due to localization of fields, but also outside the rod along the substrate due to interference of propagating polaritons.

This observation rises the question of how to tune and control not only the standing waves, but also the propagating waves launched by the microrods to enable future usage in waveguiding or nanophotonic devices [16, 17]. For further measurements, a differently designed sample with identical rod lengths would be beneficial to avoid aspect ratio influences on the propagating wave results. Emphasis could instead be placed on the change in interference of propagating waves for different rod spacings.

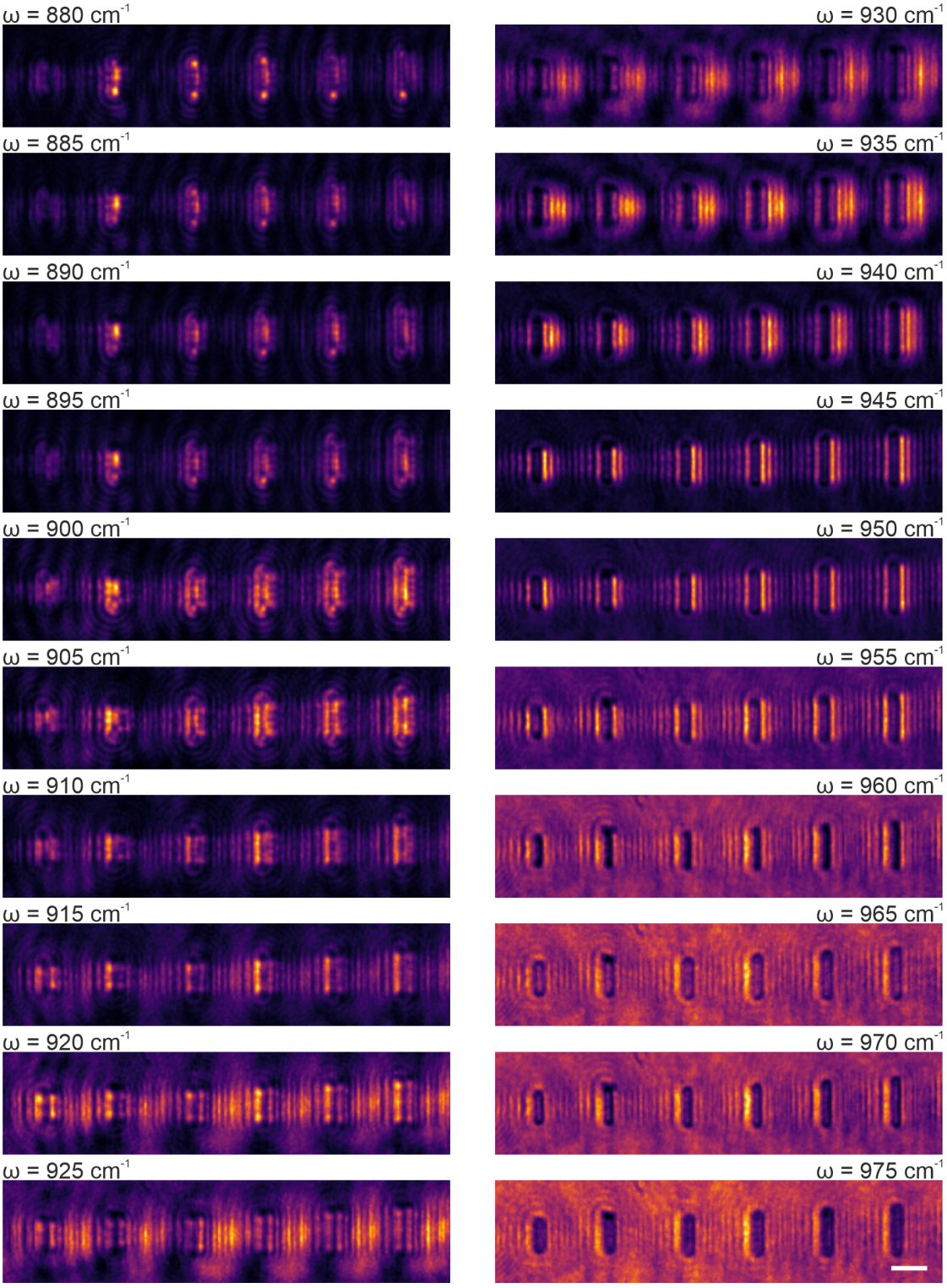

Figure 9.5. *Propagating waves launched by microrods.* SFG images showing the launching of propagating waves by the microrod ($d = 2\,\mu m$, $l = 9 - 14\,\mu m$) in the IR-frequency range of $880\,cm^{-1}$ to $975\,cm^{-1}$. The white scale bar in the bottom right corner has a length of $10\,\mu m$.

10

Discussion and Outlook

During this thesis, a new microscope based on sum-frequency generation has been built and characterized as well as intensively used to study surface phonon polaritons.
Upconverting the IR resonance laser with visible light of much shorter wavelength inherently provides the opportunity of IR sub-diffractional imaging. The introduced microscope provides a spatial resolution of $\approx 1.4\,\mu m$ which is well below the mid- to far-IR excitation wavelength. The technique not only allows for highly resolved images but also offers the simultaneous acquisition of local spectra due to the combination with a spectrally tunable IR-FEL. Pixel-wise spectroscopic analysis enables detailed insight into regions of interest.
It was shown that the technique of SFG spectro-microscopy is an ideal tool to study propagating polaritons and localized resonances in sub-diffractional sized microstructures. Their hybridization provided the opportunity to extensively study strong coupling in metasurfaces of SiC micropillars simultaneously by resonance spectral imaging and spatial interferometry.

The spatial resolution of $1.4\,\mu m$ was determined using an IR wavelength of $\approx 11\,\mu m$ and corresponds to $\sim \lambda_{IR}/9$. A higher relative resolution as stated in experiments using, e.g., s-SNOM can easily be achieved for larger IR wavelengths. With the upgrade of the FHI-FEL, wavelengths up to $160\,\mu m$ can be reached and thus softer materials like ionic and salt crystals like KBr or LiF become of interest. The current setup is, however, limited to a maximum relative resolution of $\approx \lambda_{IR}/35$ corresponding to the current maximum in IR wavelength of $\omega_{IR} \approx 50\mu m$ provided by the FEL. Additionally, a long-wave limit is set by the necessity of spectral separability of the VIS and SFG beams by a spectral filter in front of the objective. In addition to the reduced possible relative resolution, the current back-illumination setup is limited to transparent samples only. By changing to, e.g., oblique visible incidence, the microscope becomes applicable to a broader range of small band gap materials such as GaAs and respective heterostructures.
Experiments discussed within this thesis have been performed with $\approx 2\,\%$ of the total energy available for the visible beam. Thus, polaritonic resonances in materials with less field enhancement might still be measureable, without the necessity of integration for long periods of time. The setup, therefore, might also be appropriate to study 2D materials and monolayers, providing high sensitivity to SFG signal in, e.g., hBN [186, 187] or oxide perovskites [188].

The gap towards more chemistry-relevant research can be bridged by, e.g., chiral

polaritons [189, 190]. In a first attempt, left-handed and right-handed chiral photonic structures offer a basic investigation of polaritonic measurements with circular polarized light. By combination of chiral light and chiral material excitation, chiral polaritons can be examined. For interaction with optical modes, systems using resonators with chiral matter have been proven successful [191, 192]. With the wide spectral range offered by the FEL, many molecular polaritonic resonances can be reached. First experiments on creating circular polarized light with the FEL have been successful. The high-resolution resonant imaging offered by the SFG microscope makes the turn towards chiral polaritons an interesting opportunity. Additionally, chirality breaks the inversion symmetry, thus experiments can be done in materials which usually do not exhibit a non-zero $\chi^{(2)}$.

Circularly polarized light can also be utilized to directly launch polaritons in topological metasurfaces, where they are confined to specifically designed domain boundaries [175, 176]. With circularly polarized excitation, propagation can be steered into certain directions [64]. The ability of directionally controlled propagation along arbitrary paths makes topological polaritons a great tool applicable to, e.g., quantum nanophotonics [193] or heat transfer [194]. To date, the imaging of topological states is challenging, due to a lack of spatial resolution and limitations of the spectral range of common near-field techniques [64, 177]. Therefore, SFG spectro-microscopy is the ideal tool to overcome these limitations, and extends the available palette of imaging techniques by a fast and non-perturbative, spectrally-broad microscopic technique.

So far, the work has focused on surface phonon polaritons only. But not only SPhPs are accessible with the SFG microscope setup, a current project examines phonons and their utilization for switching material properties [195, 196]. By applying the SFG spectro-microscopy technique, domains in ferroic materials can be studied non-invasively. Such experiments are expected to give insight to energy-efficient and stable inversion of magnetization or ferroelectric polarization.

A

Appendix

A.1 Agilite 569 Burst Laser System

After Sec. 4.2.2 discussed the working principle of the seed laser and the amplification process in detail, this section provides supporting information on the setup of the seeder and the amplifier system.

A.1.1 Seed Oscillator

The setup of the seed oscillator is illustrated in Fig. A.1. All relevant components are numbered and described in Tab. A.1. The resonator beam is depicted in red and the output beam in blue.

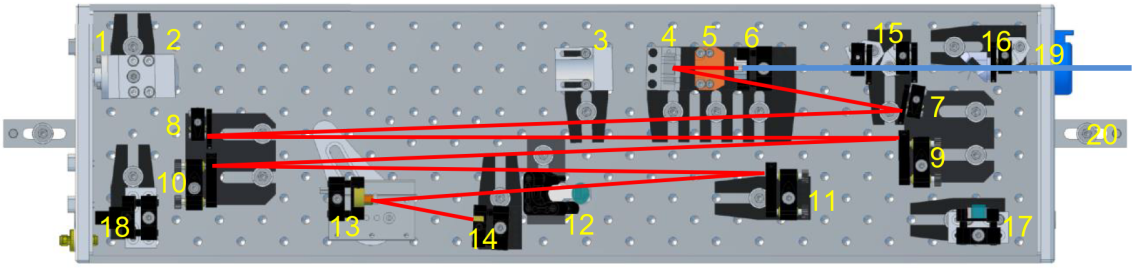

Figure A.1. *Montfort Seeder Setup.* Top view schematic of seed oscillator with numbering of all relevant items. Image from user manual.

Pulse Length

The pulse length of the micro pulses has been determined using a home-built autocorrelation setup. For this purpose, the seed laser beam without amplification was split in two beams by a 50/50-beam splitter and overlapped on a BBO crystal. One of the beams was guided over a translation stage to tune the timing between both beams. At sufficient temporal overlap of both pulses, a photodiode could detect SHG light behind the crystal. Fig. A.2 shows the results of an autocorrelation measurement over a range of 100 ps.

From the Lorentzian fit the FWHM $\approx$ 15.4 ps can be extracted leading to a pulse length of $\tau_{\text{micro}} = \text{FWHM}/\sqrt{2} \approx 11$ ps.

Table A.1. Optical elements of seed laser setup.

#	*Optical element*
1	SMA connector
2	Pump collimation lens L1
3	Pump focusing lens L2
4	Dichroic mirror, i.e., transparent for pump light, reflective for cavity beam
5	Laser gain medium
6	Outcoupling mirror, cavity mirror C1
7-11	Laser mirrors M1-M5
12	Brewster window
13	Laser mirror M6 on voltage controlled piezo and translation stage
14	SeSAM, cavity mirror C2
15	Output collimating lens
16	Pick-off mirror, a small part of the output beam is guided onto a photo detector (18)
17	Periscope
18	Photo detector
19	Shutter
20	Clamp

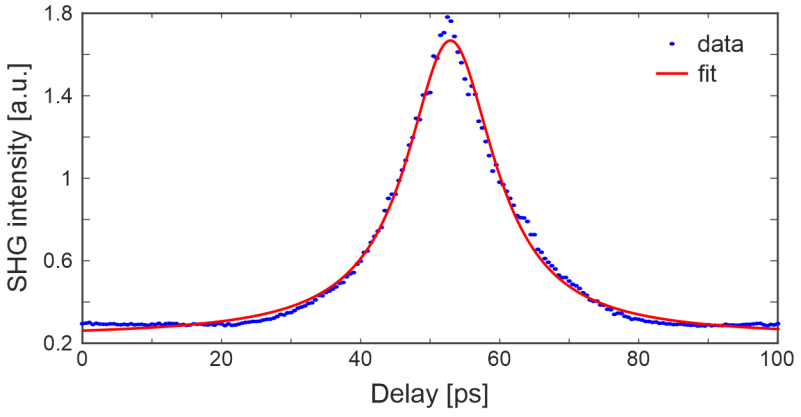

Figure A.2. *Auto-correlation measurement for pulse length estimation.* SHG intensity (blue dots) as a function of the delay of one seed laser beam. Lorentzian fit shown in red.

A.1.2 Amplitude amplifier system

Fig. A.3 shows the setup of the amplifier system. The most important components are highlighted in green and summarized in Tab. A.2.

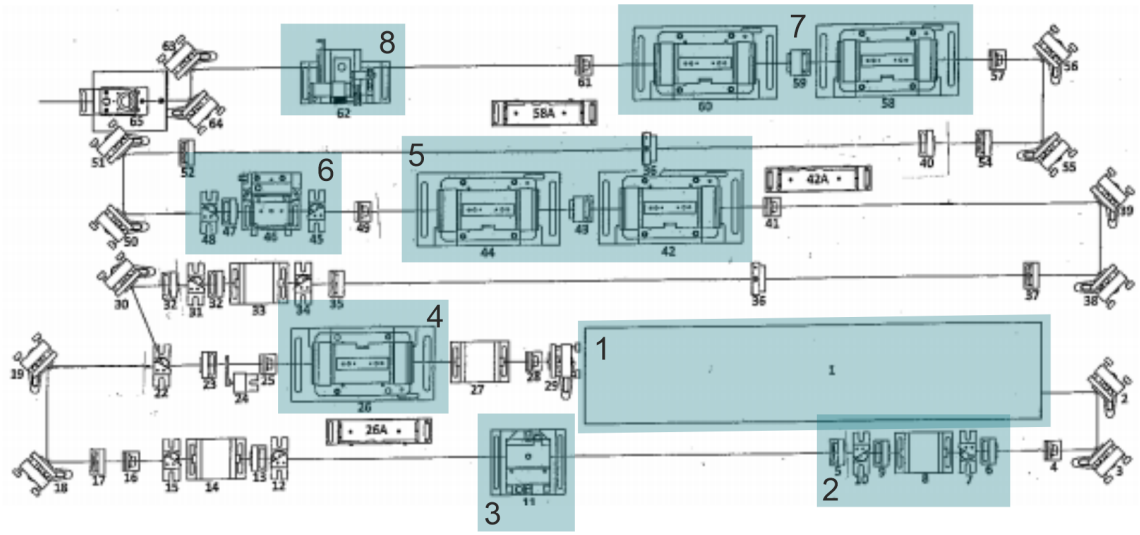

Figure A.3. *Agilite amplifier setup.* Image from user manual.

Table A.2. Main components of amplification setup.

#	*Device*	
1	Seed laser	
2	Faraday isolator	protects seeder from any feedback from the amplification
3	AOM	shapes micropulses into 10 Hz macropulse structure
4	5 mm amplifier	in double pass configuration, the beam is guided twice through the amplifier
5	6 mm amplifier	single pass configuration with two amplifiers in a row
6	Pockels cell	suppresses spontaneous emission and sharpens the macropulse structure
7	9 mm amplifier	as #5
8	KTP crystal	second-harmonic generation of the 1064 nm light, generation of 532 nm visible light

Table A.3. Timing values for beam amplification process. Alignment mode in brackets.

device	*time* [µs]
AOM	279
Pockels cell	279.3
5 mm amplifier	133
6 mm amplifier	60
9 mm amplifier	60 (500)

Timing Values

Table A.3 contains the timing values for the individual parts of the amplification process as discussed in Sec. 4.2.2. Depending on the amplification mode, i.e., measurement mode or alignment mode, the 9 mm amplifier starts charging either 60 µs or 500 µs after the trigger.

Bibliography

[1] M. A. Iqbal, M. Malik, N. Anwar, S. Bakhsh, S. Javeed, S. Sarah Maidin, K. Morsy, R. Y. Capangpangan, A. C. Alguno, and J. R. Choi, *Basic concepts, advances and emerging applications of nanophotonics*, Arabian Journal of Chemistry, 16 (2023), p. 105040.

[2] M. Francoeur, M. P. Mengüç, and R. Vaillon, *Near-field radiative heat transfer enhancement via surface phonon polaritons coupling in thin films*, Applied Physics Letters, 93 (2008), p. 043109.

[3] H. A. Atwater and A. Polman, *Plasmonics for improved photovoltaic devices*, Nature Materials, 9 (2010), pp. 205–213.

[4] S. Zeng, D. Baillargeat, H.-P. Ho, and K.-T. Yong, *Nanomaterials enhanced surface plasmon resonance for biological and chemical sensing applications*, Chem. Soc. Rev., 43 (2014), pp. 3426–3452.

[5] J. J. Mock, R. T. Hill, Y.-J. Tsai, A. Chilkoti, and D. R. Smith, *Probing Dynamically Tunable Localized Surface Plasmon Resonances of Film-Coupled Nanoparticles by Evanescent Wave Excitation*, Nano Letters, 12 (2012), pp. 1757–1764.

[6] X. He, H. Hu, Z. Yang, Y. Cai, W. Wang, Z. Han, J. Shi, and H. Xu, *On-Chip Detection of Multiwavelength Surface Plasmon Polaritons Based on Plasmonic Demultiplexers*, ACS Photonics, 9 (2022), pp. 391–397.

[7] Y. Zhang, C.-K. Lim, Z. Dai, G. Yu, J. W. Haus, H. Zhang, and P. N. Prasad, *Photonics and optoelectronics using nano-structured hybrid perovskite media and their optical cavities*, Physics Reports, 795 (2019), pp. 1–51.

[8] A. V. Zayats, I. I. Smolyaninov, and A. A. Maradudin, *Nano-optics of surface plasmon polaritons*, Physics Reports, 408 (2005), pp. 131–314.

[9] J. M. Pitarke, V. M. Silkin, E. V. Chulkov, and P. M. Echenique, *Theory of surface plasmons and surface-plasmon polaritons*, Reports on Progress in Physics, 70 (2006), p. 1.

[10] J. Zhang, L. Zhang, and W. Xu, *Surface plasmon polaritons: physics and applications*, Journal of Physics D: Applied Physics, 45 (2012), p. 113001.

[11] R. S. Anwar, H. Ning, and L. Mao, *Recent advancements in surface plasmon polaritons-plasmonics in subwavelength structures in microwave and terahertz regimes*, Digital Communications and Networks, 4 (2018), pp. 244–257.

[12] M. Fleischmann, P. Hendra, and A. McQuillan, *Raman spectra of pyridine adsorbed at a silver electrode*, Chemical Physics Letters, 26 (1974), pp. 163–166.

[13] P. Zijlstra, J. W. M. Chon, and M. Gu, *Five-dimensional optical recording mediated by surface plasmons in gold nanorods*, Nature, 459 (2009), pp. 410–413.

[14] J.-F. Li, C.-Y. Li, and R. F. Aroca, *Plasmon-enhanced fluorescence spectroscopy*, Chem. Soc. Rev., 46 (2017), pp. 3962–3979.

[15] J. D. Caldwell, L. Lindsay, V. Giannini, I. Vurgaftman, T. L. Reinecke, S. A. Maier, and O. J. Glembocki, *Low-loss, infrared and terahertz nanophotonics using surface phonon polaritons* , Nanophotonics, 4 (2015), pp. 44–68.

[16] C. R. Gubbin, S. De Liberato, and T. G. Folland, *Surface phonon polaritons for infrared optoelectronics*, Journal of Applied Physics, 131 (2022), p. 030901.

[17] S. Foteinopoulou, G. C. R. Devarapu, G. S. Subramania, S. Krishna, and D. Wasserman, *Phonon-polaritonics: enabling powerful capabilities for infrared photonics*, Nanophotonics, 8 (2019), pp. 2129–2175.

[18] A. Hartschuh, *Tip-Enhanced Near-Field Optical Microscopy*, Angewandte Chemie International Edition, 47 (2008), pp. 8178–8191.

[19] X. Chen, D. Hu, R. Mescall, G. You, D. N. Basov, Q. Dai, and M. Liu, *Modern Scattering-Type Scanning Near-Field Optical Microscopy for Advanced Material Research*, Advanced Materials, 31 (2019), p. 1804774.

[20] P. Achmari, A. M. Siddiquee, G. Si, J. Lin, B. Abbey, and S. Kou, *Investigating the probe-tip influence on imaging using scanning near-field optical microscopy*, OSA Continuum, 4 (2021), pp. 1143–1154.

[21] L. Schermelleh, A. Ferrand, T. Huser, C. Eggeling, M. Sauer, O. Biehlmaier, and G. P. C. Drummen, *Super-resolution microscopy demystified*, Nature Cell Biology, 21 (2019), pp. 72–84.

[22] Y. R. Shen, *Fundamentals of Sum-Frequency Spectroscopy*, Cambridge Molecular Science, Cambridge University Press, 2016.

[23] V. Raghunathan, Y. Han, O. Korth, N.-H. Ge, and E. O. Potma, *Rapid vibrational imaging with sum frequency generation microscopy*, Opt. Lett., 36 (2011), pp. 3891–3893.

[24] K. Cimatu and S. Baldelli, *Sum Frequency Generation Microscopy of Microcontact-Printed Mixed Self-Assembled Monolayers*, The Journal of Physical Chemistry B, 110 (2006), pp. 1807–1813.

[25] A. Hanninen, M. W. Shu, and E. O. Potma, *Hyperspectral imaging with laser-scanning sum-frequency generation microscopy*, Biomed. Opt. Express, 8 (2017), pp. 4230–4242.

[26] R. Claus and L. Merten, *Light scattering by phonon-polaritons*, Springer tracts in modern physics, Springer, Berlin [u. a.], 1975.

[27] J. J. Hopfield, *Theory of the Contribution of Excitons to the Complex Dielectric Constant of Crystals*, Phys. Rev., 112 (1958), pp. 1555–1567.

[28] K. U. N. Huang, *Lattice Vibrations and Optical Waves in Ionic Crystals*, Nature, 167 (1951), pp. 779–780.

[29] R. S. Knox, *Theory of excitons*, Academic Press New York, New York, 1963.

[30] E. Burstein and S. italiana di fisica, *Atomic Structure and Properties of Solids*, no. Bd. 52 in Atomic Structure and Properties of Solids, Academic Press, 1972.

[31] R. G. Lerner, *Concise encyclopedia of solid state physics*, Addison-Wesley, Reading, Mass., 1983.

[32] D. T. Ha, D. T. Thuy, V. T. Hoa, T. T. T. Van, and N. A. Viet, *On the theory of three types of polaritons (phonon, exciton and plasmon polaritons)*, Journal of Physics: Conference Series, 865 (2017), p. 012007.

[33] H. Klapper and T. Hahn, *Point-group symmetry and physical properties of crystals*, 01 2002, pp. 804–808.

[34] P. Drude, *Zur Elektronentheorie der Metalle*, Annalen der Physik, 306 (1900), pp. 566–613.

[35] H. Lorentz, *The Theory of Electrons and Its Applications to the Phenomena of Light and Radiant Heat: A Course of Lectures Delivered in Columbia*

University, New York, in March and April, 1906, no. Nr. 2 in B.G. Teubners Sammlung von Lehrbüchern auf dem Gebiete der mathematischen Wissenschaften mit Einschluss ihrer Anwendungen, B.G. Teubner, 1909.

[36] P. YU AND M. CARDONA, *Fundamentals of Semiconductors: Physics and Materials Properties*, Graduate Texts in Physics, Springer Berlin Heidelberg, 2010.

[37] G. CZYCHOLL, *Theoretische Festkörperphysik*, 4. aufl. ed., 2016.

[38] S. ADACHI, *The Reststrahlen Region*, Springer US, Boston, MA, 1999, pp. 33–62.

[39] F. GERVAIS AND B. PIRIOU, *Anharmonicity in several-polar-mode crystals: adjusting phonon self-energy of LO and TO modes in Al_2O_3 and TiO_2 to fit infrared reflectivity*, Journal of Physics C: Solid State Physics, 7 (1974), p. 2374.

[40] R. H. LYDDANE, R. G. SACHS, AND E. TELLER, *On the Polar Vibrations of Alkali Halides*, Phys. Rev., 59 (1941), pp. 673–676.

[41] M. BASS, *Handbook of optics*, MacGraw-Hill, New York [u. a.], 3. ed. ed., 2010.

[42] G. ZHIZHIN, M. MOSKALOVA, E. SHOMINA, AND V. YAKOVLEV, *Chapter 3 - Surface Electromagnetic Wave Propagation on Metal Surfaces*, in Surface Polaritons, V. Agranovich and D. Mills, eds., vol. 1 of Modern Problems in Condensed Matter Sciences, Elsevier, 1982, pp. 93–144.

[43] N. C. PASSLER, *Phonon Polaritons in Polar Dielectric Heterostructures*, dissertation, Freie Universität Berlin, 2020.

[44] C. R. GUBBIN, S. A. MAIER, AND S. DE LIBERATO, *Theoretical investigation of phonon polaritons in SiC micropillar resonators*, Phys. Rev. B, 95 (2017), p. 035313.

[45] G. SÜSSMANN, *Über den Impuls der Schallquanten I*, Zeitschrift für Naturforschung A, 11 (1956), pp. 1–14.

[46] N. C. PASSLER, I. RAZDOLSKI, S. GEWINNER, W. SCHÖLLKOPF, M. WOLF, AND A. PAARMANN, *Second-Harmonic Generation from Critically Coupled Surface Phonon Polaritons*, ACS Photonics, 4 (2017), pp. 1048–1053.

[47] M. HARAGUCHI, M. FUKUI, AND S. MUTO, *Experimental observation of attenuated-total-reflection spectra of GaAs/AlAs superlattice*, Phys. Rev. B, 41 (1990), pp. 1254–1257.

[48] A. J. Huber, B. Deutsch, L. Novotny, and R. Hillenbrand, *Focusing of surface phonon polaritons*, Applied Physics Letters, 92 (2008), p. 203104.

[49] M. Kohlmann, C. Denker, N. Passler, J. Kredl, M. Wolf, M. Münzenberg, and A. Paarmann, *Second harmonic generation from grating-coupled hybrid plasmon–phonon polaritons*, Applied Physics Letters, 121 (2022), p. 191105.

[50] R. Hillenbrand, T. Taubner, and F. Keilmann, *Phonon-enhanced light–matter interaction at the nanometre scale*, Nature, 418 (2002), pp. 159–62.

[51] T. Wang, P. Li, B. Hauer, D. N. Chigrin, and T. Taubner, *Optical Properties of Single Infrared Resonant Circular Microcavities for Surface Phonon Polaritons*, Nano Letters, 13 (2013), pp. 5051–5055.

[52] Z. Fei, G. O. Andreev, W. Bao, L. M. Zhang, A. S. McLeod, C. Wang, M. K. Stewart, Z. Zhao, G. Dominguez, M. Thiemens, M. M. Fogler, M. J. Tauber, A. H. Castro-Neto, C. N. Lau, F. Keilmann, and D. N. Basov, *Infrared Nanoscopy of Dirac Plasmons at the Graphene–SiO_2 Interface*, Nano Letters, 11 (2011), pp. 4701–4705.

[53] A. J. Huber, F. Keilmann, J. Wittborn, J. Aizpurua, and R. Hillenbrand, *Terahertz Near-Field Nanoscopy of Mobile Carriers in Single Semiconductor Nanodevices*, Nano Letters, 8 (2008), pp. 3766–3770.

[54] E. S. Kooij, W. Ahmed, H. J. W. Zandvliet, and B. Poelsema, *Localized Plasmons in Noble Metal Nanospheroids*, The Journal of Physical Chemistry C, 115 (2011), pp. 10321–10332.

[55] H. Mutschke, A. Andersen, D. Clément, T. Henning, and G. Peiter, *Infrared properties of SiC particles*, Astronomy & Astrophysics - ASTRON ASTROPHYS, 345 (1999).

[56] J. D. Caldwell, O. J. Glembocki, Y. Francescato, N. Sharac, V. Giannini, F. J. Bezares, J. P. Long, J. C. Owrutsky, I. Vurgaftman, J. G. Tischler, V. D. Wheeler, N. D. Bassim, L. M. Shirey, R. Kasica, and S. A. Maier, *Low-Loss, Extreme Subdiffraction Photon Confinement via Silicon Carbide Localized Surface Phonon Polariton Resonators*, Nano Letters, 13 (2013), pp. 3690–3697.

[57] C. R. Gubbin, F. Martini, A. Politi, S. A. Maier, and S. De Liberato, *Strong and Coherent Coupling between Localized and Propagating Phonon Polaritons*, Phys. Rev. Lett., 116 (2016), p. 246402.

[58] R. Berte, C. R. Gubbin, V. D. Wheeler, A. J. Giles, V. Giannini, S. A. Maier, S. De Liberato, and J. D. Caldwell, *Sub-nanometer Thin Oxide Film Sensing with Localized Surface Phonon Polaritons*, ACS Photonics, 5 (2018), pp. 2807–2815.

[59] Y. Chen, Y. Francescato, J. D. Caldwell, V. Giannini, T. W. W. Mass, O. J. Glembocki, F. J. Bezares, T. Taubner, R. Kasica, M. Hong, and S. A. Maier, *Spectral Tuning of Localized Surface Phonon Polariton Resonators for Low-Loss Mid-IR Applications*, ACS Photonics, 1 (2014), pp. 718–724.

[60] A. Bylinkin, M. Schnell, M. Autore, F. Calavalle, P. Li, J. Taboada-Gutièrrez, S. Liu, J. H. Edgar, F. Casanova, L. E. Hueso, P. Alonso-Gonzalez, A. Y. Nikitin, and R. Hillenbrand, *Real-space observation of vibrational strong coupling between propagating phonon polaritons and organic molecules*, Nature Photonics, 15 (2021), pp. 197–202.

[61] M. Autore, P. Li, I. Dolado, F. J. Alfaro-Mozaz, R. Esteban, A. Atxabal, F. Casanova, L. E. Hueso, P. Alonso-González, J. Aizpurua, A. Y. Nikitin, et al., *Boron nitride nanoresonators for phonon-enhanced molecular vibrational spectroscopy at the strong coupling limit*, Light: Science & Applications, 7 (2018), p. 17172.

[62] G. Lu, C. R. Gubbin, J. R. Nolen, T. Folland, M. J. Tadjer, S. De Liberato, and J. D. Caldwell, *Engineering the Spectral and Spatial Dispersion of Thermal Emission via Polariton–Phonon Strong Coupling*, Nano Letters, 21 (2021), pp. 1831–1838.

[63] J.-J. Greffet, R. Carminati, K. Joulain, J.-P. Mulet, S. Mainguy, and Y. Chen, *Coherent emission of light by thermal sources*, Nature, 416 (2002), pp. 61–64.

[64] S. Guddala, F. Komissarenko, S. Kiriushechkina, A. Vakulenko, M. Li, V. M. Menon, A. Alù, and A. B. Khanikaev, *Topological phonon-polariton funneling in midinfrared metasurfaces*, Science, 374 (2021), pp. 225–227.

[65] A. Konrad, A. M. Kern, M. Brecht, and A. J. Meixner, *Strong and Coherent Coupling of a Plasmonic Nanoparticle to a Subwavelength Fabry–Pérot Resonator*, Nano Letters, 15 (2015), pp. 4423–4428.

[66] N. C. Passler, C. R. Gubbin, T. G. Folland, I. Razdolski, D. S. Katzer, D. F. Storm, M. Wolf, S. De Liberato, J. D. Caldwell,

and A. Paarmann, *Strong Coupling of Epsilon-Near-Zero Phonon Polaritons in Polar Dielectric Heterostructures*, Nano Letters, 18 (2018), pp. 4285–4292.

[67] L. Novotny, *Strong coupling, energy splitting, and level crossings: A classical perspective*, American Journal of Physics, 78 (2010), pp. 1199–1202.

[68] D. S. Dovzhenko, S. V. Ryabchuk, Y. P. Rakovich, and I. R. Nabiev, *Light–matter interaction in the strong coupling regime: configurations, conditions, and applications*, Nanoscale, 10 (2018), pp. 3589–3605.

[69] R. Kiessling, Y. Tong, A. J. Giles, S. Gewinner, W. Schöllkopf, J. D. Caldwell, M. Wolf, and A. Paarmann, *Surface Phonon Polariton Resonance Imaging Using Long-Wave Infrared-Visible Sum-Frequency Generation Microscopy*, ACS Photonics, 6 (2019), pp. 3017–3023.

[70] W. Gerabek, B. Haage, G. Keil, and W. Wegner, *Enzyklopädie Medizingeschichte*, De Gruyter, 2011.

[71] M. M. Freundlich, *Origin of the Electron Microscope*, Science, 142 (1963), pp. 185–188.

[72] J. T. Cremer, M. A. Piestrup, H. Park, C. K. Gary, R. H. Pantell, C. J. Glinka, and J. G. Barker, *Imaging hydrogenous materials with a neutron microscope*, Applied Physics Letters, 87 (2005), p. 161913.

[73] B. W. Ward, J. A. Notte, and N. P. Economou, *Helium ion microscope: A new tool for nanoscale microscopy and metrology*, Journal of Vacuum Science & Technology B: Microelectronics and Nanometer Structures Processing, Measurement, and Phenomena, 24 (2006), pp. 2871–2874.

[74] H. F. Wetzlar, *Handbuch der Mikroskopie in der Technik*, Umschau-Verl., Frankfurt am Main, 1957.

[75] M. W. D. Douglas B. Murphy, *Fundamentals of Light Microscopy*, John Wiley and Sons, Ltd, 2012, ch. 1, pp. 1–19.

[76] E. Abbe, *Beiträge zur Theorie des Mikroskops und der mikroskopischen Wahrnehmung*, Archiv für mikroskopische Anatomie, (1873).

[77] *Transactions of the Cambridge Philosophical Society*, Cambridge Philosophical Society, 1835, ch. Transactions of the Cambridge Philosophical Society: On the Diffraction of an Object-glass with Circular Aperture .

[78] L. R. F.R.S., *XXXI. Investigations in optics, with special reference to the spectroscope*, The London, Edinburgh, and Dublin Philosophical Magazine and Journal of Science, 8 (1879), pp. 261–274.

[79] M. J. Booth, *Microscope Resolution Estimation and Normalised Coordinates*, Dec. 2020.

[80] R. Borlinghaus, *Unbegrenzte Lichtmikroskopie: Über Auflösung und Super-Hochauflösung und die Frage, ob man Moleküle sehen kann*, essentials, Springer Fachmedien Wiesbaden, 2015.

[81] S. Kawata, T. Ichimura, A. Taguchi, and Y. Kumamoto, *Nano-Raman Scattering Microscopy: Resolution and Enhancement*, Chemical Reviews, 117 (2017), pp. 4983–5001.

[82] S. Kaščáková, L. Maigre, J. Chevalier, M. Réfrégiers, and J.-M. Pagès, *Antibiotic Transport in Resistant Bacteria: Synchrotron UV Fluorescence Microscopy to Determine Antibiotic Accumulation with Single Cell Resolution*, PLOS ONE, 7 (2012), pp. 1–9.

[83] G. Vicidomini, P. Bianchini, and A. Diaspro, *STED super-resolved microscopy*, Nature Methods, 15 (2018).

[84] T. A. Klar, S. Jakobs, M. Dyba, A. Egner, and S. W. Hell, *Fluorescence microscopy with diffraction resolution barrier broken by stimulated emission*, Proceedings of the National Academy of Sciences, 97 (2000), pp. 8206–8210.

[85] R. Heintzmann and T. Huser, *Super-Resolution Structured Illumination Microscopy*, Chemical Reviews, 117 (2017), pp. 13890–13908.

[86] G. Ball, J. Demmerle, R. Kaufmann, I. Davis, I. M. Dobbie, and L. Schermelleh, *SIMcheck: a Toolbox for Successful Super-resolution Structured Illumination Microscopy*, Scientific Reports, 5 (2015), p. 15915.

[87] M. Bates, S. Jones, and X. Zhuang, *Stochastic Optical Reconstruction Microscopy (STORM): A Method for Superresolution Fluorescence Imaging*, Cold Spring Harbor protocols, 2013 (2013).

[88] B. Huang, W. Wang, M. Bates, and X. Zhuang, *Three-dimensional super-resolution imaging by stochastic optical reconstruction microscopy*, Science, 319 (2008), pp. 810–3.

[89] C. A. Combs, *Fluorescence microscopy: a concise guide to current imaging methods, journal = Curr Protoc Neurosci*, Chapter 2 (2010), p. Unit2.1.

[90] H. Heinzelmann and P. D.W., *Scanning near-field optical microscopy*, Applied Physics A, (1994).

[91] G. Longo, M. Girasole, G. Pompeo, and A. Cricenti, *Optical super-resolution using higher harmonics and different acquisition modes in an aperture tapping SNOM*, physica status solidi (b), 247 (2010), pp. 2056–2060.

[92] A. Dazzi, *Photothermal Induced Resonance. Application to Infrared Spectromicroscopy*, vol. 118, 12 2009, pp. 469–503.

[93] Z. Li, K. Aleshire, M. Kuno, and G. V. Hartland, *Super-Resolution Far-Field Infrared Imaging by Photothermal Heterodyne Imaging*, The Journal of Physical Chemistry B, 121 (2017), pp. 8838–8846.

[94] T. Meyer, M. Schmitt, B. Dietzek, and J. Popp, *Accumulating advantages, reducing limitations: Multimodal nonlinear imaging in biomedical sciences – The synergy of multiple contrast mechanisms*, Journal of Biophotonics, 6 (2013), pp. 887–904.

[95] V. Parodi, E. Jacchetti, R. Osellame, G. Cerullo, D. Polli, and M. T. Raimondi, *Nonlinear Optical Microscopy: From Fundamentals to Applications in Live Bioimaging*, Frontiers in Bioengineering and Biotechnology, 8 (2020).

[96] C. A. Combs, *Fluorescence Microscopy: A Concise Guide to Current Imaging Methods*, Current Protocols in Neuroscience, 50 (2010), pp. 2.1.1–2.1.14.

[97] Y. Shen, *The Principles of Nonlinear Optics*, Wiley, 1984.

[98] R. Boyd and D. Prato, *Nonlinear Optics*, Elsevier Science, 2008.

[99] K. Buschow, *Encyclopedia of Materials: Science and Technology*, no. Bd. 10 in Encyclopedia of Materials: Science and Technology, Elsevier, 2001.

[100] C. J. Winta, *Second-Harmonic Phonon Spectroscopy Using an Infrared Free-Electron Laser*, dissertation, Freie Universität Berlin, 2021.

[101] C. Garrett, *Nonlinear optics, anharmonic oscillators, and pyroelectricity*, IEEE Journal of Quantum Electronics, 4 (1968), pp. 70–84.

[102] M. Bass, P. A. Franken, A. E. Hill, C. W. Peters, and G. Weinreich, *Optical Mixing*, Phys. Rev. Lett., 8 (1962), pp. 18–18.

[103] J. Schaefer, G. Gonella, M. Bonn, and E. H. G. Backus, *Surface-specific vibrational spectroscopy of the water/silica interface: screening and interference*, Phys. Chem. Chem. Phys., 19 (2017), pp. 16875–16880.

[104] S. M. Piontek, D. Naujoks, T. Tabassum, M. J. DelloStritto, M. Jaugstetter, P. Hosseini, M. Corva, A. Ludwig, K. Tschulik, M. L. Klein, and P. B. Petersen, *Probing the Gold/Water Interface with Surface-Specific Spectroscopy*, ACS Physical Chemistry Au, 3 (2023), pp. 119–129.

[105] M. Bonn, C. Hess, S. Funk, J. H. Miners, B. N. J. Persson, M. Wolf, and G. Ertl, *Femtosecond Surface Vibrational Spectroscopy of CO Adsorbed on Ru(001) during Desorption*, Phys. Rev. Lett., 84 (2000), pp. 4653–4656.

[106] W.-T. Liu and Y. R. Shen, *In situ sum-frequency vibrational spectroscopy of electrochemical interfaces with surface plasmon resonance*, Proceedings of the National Academy of Sciences, 111 (2014), pp. 1293–1297.

[107] S. Mukamel, *Principles of Nonlinear Optical Spectroscopy*, Oxford series in optical and imaging sciences, Oxford University Press, 1995.

[108] F. Vidal and A. Tadjeddine, *Sum-frequency generation spectroscopy of interfaces*, Reports on Progress in Physics, 68 (2005), p. 1095.

[109] P. D. Maker, R. W. Terhune, M. Nisenoff, and C. M. Savage, *Effects of Dispersion and Focusing on the Production of Optical Harmonics*, Phys. Rev. Lett., 8 (1962), pp. 21–22.

[110] W.-T. Liu and Y. R. Shen, *Sum-frequency phonon spectroscopy on α-quartz*, Phys. Rev. B, 78 (2008), p. 024302.

[111] M. Flörsheimer, C. Brillert, and H. Fuchs, *Chemical imaging of interfaces by sum-frequency generation*, Materials Science and Engineering: C, 8-9 (1999), pp. 335–341.

[112] H. Wang and W. Xiong, *Vibrational Sum-Frequency Generation Hyperspectral Microscopy for Molecular Self-Assembled Systems*, Annual Review of Physical Chemistry, 72 (2021), pp. 279–306.

[113] R. D. Schaller, J. C. Johnson, K. R. Wilson, L. F. Lee, L. H. Haber, and R. J. Saykally, *Nonlinear Chemical Imaging Nanomicroscopy: From Second and Third Harmonic Generation to Multiplex (Broad-Bandwidth) Sum Frequency Generation Near-Field Scanning Optical Microscopy*, The Journal of Physical Chemistry B, 106 (2002), pp. 5143–5154.

[114] D. M. P. Hoffmann, K. Kuhnke, and K. Kern, *Sum-frequency generation microscope for opaque and reflecting samples*, Review of Scientific Instruments, 73 (2002), pp. 3221–3226.

[115] M. B. Raschke, M. Schubert, P. Narang, and A. Paarmann, *Optical nanoprobe imaging and spectroscopy*, Applied Physics Letters, 123 (2023), p. 230401.

[116] K. Inoue, M. Fujii, and M. Sakai, *Development of a Non-Scanning Vibrational Sum-Frequency Generation Detected Infrared Super-Resolution Microscope and its Application to Biological Cells*, Applied Spectroscopy, 64 (2010), pp. 275–281.

[117] R. Kiessling, *Optical Sum-Frequency Response of Lattice Vibrations and Pulse Timing at a Free-Electron Laser*, dissertation, Freie Universität Berlin, 2020.

[118] Z. Sun, D. Zheng, and S. Baldelli, *Distortion Correction for a Brewster Angle Microscope Using an Optical Grating*, Analytical Chemistry, 89 (2017), pp. 2186–2190.

[119] K. Michel, *Die Mikrophotographie*, Die wissenschaftliche und angewandte Photographie, Springer, Wien, 1957.

[120] G. Lan and M. D. Twa, *Theory and design of Schwarzschild scan objective for Optical Coherence Tomography*, Opt. Express, 27 (2019), pp. 5048–5064.

[121] W. Schöllkopf, *The New IR FEL Facility at the Fritz-Haber-Institut in Berlin*, Stockholm, Schweden, 2014. Workshop on the scientific opportunities of a THz-FEL in Sweden, AlbaNova University Center.

[122] C. A. Brau, *Free-electron lasers*, Advances in electronics and electron physics, Academic Pr., Boston [u. a.], 1990.

[123] Y. U. Jeong, K.-H. Jang, S. Bae, V. Pathania, J. Mun, and K. Lee, *Prospects of a terahertz free-electron laser for field application*, Journal of the Korean Physical Society, 80 (2022), pp. 367–376.

[124] A. Nassiri, B. Chase, P. Craievich, A. Fabris, H. Frischholz, J. Jacob, E. Jensen, M. Jensen, R. Kustom, and R. Pasquinelli, *History and Technology Developments of Radio Frequency (RF) Systems for Particle Accelerators*, IEEE Transactions on Nuclear Science, 63 (2015), pp. 1–1.

[125] P. Schmüser, M. Dohlus, J. Rossbach, and C. Behrens, *Free-Electron Lasers in the Ultraviolet and X-Ray Regime: Physical Principles, Experimental*

Results, Technical Realization, vol. 258, 01 2014.

[126] P. Ribic and G. Margaritondo, *Status and prospects of X-ray free-electron lasers (X-FELs): a simple presentation*, Journal of Physics D-applied Physics - J PHYS-D-APPL PHYS, 45 (2012).

[127] A. He, L. Yang, and L. Yu, *High-Gain Free-Electron Laser Theory, Introduction*, Springer International Publishing, Cham, 2014, pp. 1–37.

[128] W. Schöllkopf, S. Gewinner, H. Junkes, A. Paarmann, G. von Helden, H. P. Bluem, and A. M. M. Todd, *The new IR and THz FEL facility at the Fritz Haber Institute in Berlin*, 9512 (2015), pp. 238 – 250.

[129] W. Schöllkopf, W. Colson, M. D. Pas, D. Dowell, S. Gewinner, S. Gottschalk, H. Junkes, G. Meijer, J. Rathke, T. Schultheiss, A. Todd, L. Young, and G. von Helden, *The FHI FEL Upgrade Design*, in Proc. FEL'19, no. 39 in Free Electron Laser Conference, JACoW Publishing, Geneva, Switzerland, nov 2019, pp. 52–55.

[130] G. R. Jacobovitz-Veselka, U. Keller, and M. T. Asom, *Broadband fast semiconductor saturable absorber*, Opt. Lett., 17 (1992), pp. 1791–1793.

[131] R. Kiessling, W. B. Colson, S. Gewinner, W. Schöllkopf, M. Wolf, and A. Paarmann, *Femtosecond single-shot timing and direct observation of subpulse formation in an infrared free-electron laser*, Phys. Rev. Accel. Beams, 21 (2018), p. 080702.

[132] A. Franzen. http://www.gwoptics.org/ComponentLibrary/.

[133] G. Lu, C. R. Gubbin, J. R. Nolen, T. G. Folland, K. Diaz-Granados, I. I. Kravchenko, J. A. Spencer, M. J. Tadjer, O. J. Glembocki, S. De Liberato, and J. D. Caldwell, *Collective Phonon–Polaritonic Modes in Silicon Carbide Subarrays*, ACS Nano, 16 (2022), pp. 963–973.

[134] B. Zhang, J. Zerubia, and J.-C. Olivo-Marin, *A study of Gaussian approximations of fluorescence microscopy PSF models*, in Three-Dimensional and Multidimensional Microscopy: Image Acquisition and Processing XIII, J.-A. Conchello, C. J. Cogswell, and T. Wilson, eds., vol. 6090, International Society for Optics and Photonics, SPIE, 2006, p. 60900K.

[135] D. Thomann, D. R. Rines, P. K. Sorger, and G. Danuser, *Automatic fluorescent tag detection in 3D with super-resolution: application to the analysis of chromosome movement*, Journal of Microscopy, 208 (2002), pp. 49–64.

[136] A. Huber, N. Ocelic, D. Kazantsev, and R. Hillenbrand, *Near-field imaging of mid-infrared surface phonon polariton propagation*, Applied Physics Letters, 87 (2005), p. 081103.

[137] J. Barnett, D. Wendland, M. Lewin, K. G. Wirth, A. Hessler, and T. Taubner, *Investigation of low-confinement surface phonon polariton launching on SiC and $SrTiO_3$ using scanning near-field optical microscopy*, Applied Physics Letters, 120 (2022), p. 211107.

[138] J. Schoenwald, E. Burstein, and J. Elson, *Propagation of surface polaritons over macroscopic distances at optical frequencies*, Solid State Communications, 88 (1993), pp. 1067–1071.

[139] D.-Z. A. Chen and G. Chen, *Measurement of silicon dioxide surface phonon-polariton propagation length by attenuated total reflection*, Applied Physics Letters, 91 (2007), p. 121906.

[140] T. G. Folland, L. Nordin, D. Wasserman, and J. D. Caldwell, *Probing polaritons in the mid- to far-infrared*, Journal of Applied Physics, 125 (2019), p. 191102.

[141] N. Li, C. P. Ho, S. Zhu, Y. H. Fu, Y. Zhu, and L. Y. T. Lee, *Aluminium nitride integrated photonics: a review*, Nanophotonics, 10 (2021), pp. 2347–2387.

[142] G. Álvarez Pérez, T. G. Folland, I. Errea, J. Taboada-Gutiérrez, J. Duan, J. Martín-Sánchez, A. I. F. Tresguerres-Mata, J. R. Matson, A. Bylinkin, M. He, W. Ma, Q. Bao, J. I. Martín, J. D. Caldwell, A. Y. Nikitin, and P. Alonso-González, *Infrared Permittivity of the Biaxial van der Waals Semiconductor α-MoO_3 from Near- and Far-Field Correlative Studies*, Advanced Materials, 32 (2020), p. 1908176.

[143] A. W. Bruch, X. Liu, J. B. Surya, C.-L. Zou, and H. X. Tang, *On-chip $\chi^{(2)}$ microring optical parametric oscillator*, Optica, 6 (2019), pp. 1361–1366.

[144] Y. Tang, Z. Gong, X. Liu, and H. X. Tang, *Widely separated optical Kerr parametric oscillation in AlN microrings*, Opt. Lett., 45 (2020), pp. 1124–1127.

[145] J. B. Surya, X. Guo, C.-L. Zou, and H. X. Tang, *Efficient third-harmonic generation in composite aluminum nitride/silicon nitride microrings*, Optica, 5 (2018), pp. 103–108.

[146] D. Sam-Giao, D. Néel, S. Sergent, B. Gayral, M. J. Rashid, F. Semond, J. Y. Duboz, M. Mexis, T. Guillet, C. Brimont, S. David,

X. Checoury, and P. Boucaud, *High quality factor AlN nanocavities embedded in a photonic crystal waveguide*, Applied Physics Letters, 100 (2012), p. 191104.

[147] S. Zhao, A. T. Connie, M. H. T. Dastjerdi, X. H. Kong, Q. Wang, M. Djavid, S. Sadaf, X. D. Liu, I. Shih, H. Guo, and Z. Mi, *Aluminum nitride nanowire light emitting diodes: Breaking the fundamental bottleneck of deep ultraviolet light sources*, Scientific Reports, 5 (2015), p. 8332.

[148] W. Ma, P. Alonso-González, S. Li, A. Y. Nikitin, J. Yuan, J. Martín-Sánchez, J. Taboada-Gutiérrez, I. Amenabar, P. Li, S. Vélez, C. Tollan, Z. Dai, Y. Zhang, S. Sriram, K. Kalantar-Zadeh, S.-T. Lee, R. Hillenbrand, and Q. Bao, *In-plane anisotropic and ultra-low-loss polaritons in a natural van der Waals crystal*, Nature, 562 (2018), pp. 557–562.

[149] G. Hu, Q. Ou, G. Si, Y. Wu, J. Wu, Z. Dai, A. Krasnok, Y. Mazor, Q. Zhang, Q. Bao, C.-W. Qiu, and A. Alù, *Topological polaritons and photonic magic angles in twisted α-MoO_3 bilayers*, Nature, 582 (2020), pp. 209–213.

[150] J. Duan, G. Álvarez Pérez, C. Lanza, K. Voronin, A. I. F. Tresguerres-Mata, N. Capote-Robayna, J. Álvarez Cuervo, A. Tarazaga Martín-Luengo, J. Martín-Sánchez, V. S. Volkov, A. Y. Nikitin, and P. Alonso-González, *Multiple and spectrally robust photonic magic angles in reconfigurable α-MoO_3 trilayers*, Nature Materials, 22 (2023), pp. 867–872.

[151] Y. Wu, Q. Ou, Y. Yin, Y. Li, W. Ma, W. Yu, G. Liu, X. Cui, X. Bao, J. Duan, G. Álvarez Pérez, Z. Dai, B. Shabbir, N. Medhekar, X. Li, C.-M. Li, P. Alonso-González, and Q. Bao, *Chemical switching of low-loss phonon polaritons in α-MoO_3 by hydrogen intercalation*, Nature Communications, 11 (2020), p. 2646.

[152] H.-S. Kim, J. B. Cook, H. Lin, J. S. Ko, S. H. Tolbert, V. Ozolins, and B. Dunn, *Oxygen vacancies enhance pseudocapacitive charge storage properties of MoO_{3-x}*, Nature Materials, 16 (2017), pp. 454–460.

[153] Z. Zheng, N. Xu, S. L. Oscurato, M. Tamagnone, F. Sun, Y. Jiang, Y. Ke, J. Chen, W. Huang, W. L. Wilson, A. Ambrosio, S. Deng, and H. Chen, *A mid-infrared biaxial hyperbolic van der Waals crystal*, Science Advances, 5 (2019), p. eaav8690.

[154] P. Li, M. Lewin, A. V. Kretinin, J. D. Caldwell, K. S. Novoselov,

T. Taniguchi, K. Watanabe, F. Gaussmann, and T. Taubner, *Hyperbolic phonon-polaritons in boron nitride for near-field optical imaging and focusing*, Nature Communications, 6 (2015), p. 7507.

[155] W. D. Newman, C. L. Cortes, A. Afshar, K. Cadien, A. Meldrum, R. Fedosejevs, and Z. Jacob, *Observation of long-range dipole-dipole interactions in hyperbolic metamaterials*, Science Advances, 4 (2018), p. eaar5278.

[156] A. Paarmann, I. Razdolski, S. Gewinner, W. Schöllkopf, and M. Wolf, *Effects of crystal anisotropy on optical phonon resonances in mid-infrared second harmonic response of SiC*, Phys. Rev. B, 94 (2016), p. 134312.

[157] W. J. Moore, J. Freitas, J. A., R. T. Holm, O. Kovalenkov, and V. Dmitriev, *Infrared dielectric function of wurtzite aluminum nitride*, Applied Physics Letters, 86 (2005), p. 141912.

[158] F. Keilmann, *Surface-polariton propagation for scanning near-field optical microscopy application*, Journal of Microscopy, 194 (1999), pp. 567–570.

[159] A. Ambrosio, M. Tamagnone, K. Chaudhary, L. A. Jauregui, P. Kim, W. L. Wilson, and F. Capasso, *Selective excitation and imaging of ultraslow phonon polaritons in thin hexagonal boron nitride crystals*, Light: Science & Applications, 7 (2018), p. 27.

[160] H. J. Falge and A. Otto, *Dispersion of Phonon-Like Surface Polaritons on α-Quartz Observed by Attenuated Total Reflection*, physica status solidi (b), 56 (1973), pp. 523–534.

[161] L. Caldwell and M. R. Tarbutt, *Enhancing Dipolar Interactions between Molecules Using State-Dependent Optical Tweezer Traps*, Phys. Rev. Lett., 125 (2020), p. 243201.

[162] O. Quevedo-Teruel, H. Chen, A. Díaz-Rubio, G. Gok, A. Grbic, G. Minatti, E. Martini, S. Maci, G. V. Eleftheriades, M. Chen, N. I. Zheludev, N. Papasimakis, S. Choudhury, Z. A. Kudyshev, S. Saha, H. Reddy, A. Boltasseva, V. M. Shalaev, A. V. Kildishev, D. Sievenpiper, C. Caloz, A. Alù, Q. He, L. Zhou, G. Valerio, E. Rajo-Iglesias, Z. Sipus, F. Mesa, R. Rodríguez-Berral, F. Medina, V. Asadchy, S. Tretyakov, and C. Craeye, *Roadmap on metasurfaces*, Journal of Optics, 21 (2019), p. 073002.

[163] P. Li, I. Dolado, F. J. Alfaro-Mozaz, F. Casanova, L. E. Hueso, S. Liu, J. H. Edgar, A. Y. Nikitin, S. Vélez, and R. Hillenbrand,

Infrared hyperbolic metasurface based on nanostructured van der Waals materials, Science, 359 (2018), pp. 892–896.

[164] Y. Wu, J. Duan, W. Ma, Q. Ou, P. Li, P. Alonso-González, J. D. Caldwell, and Q. Bao, *Manipulating polaritons at the extreme scale in van der Waals materials*, Nature Reviews Physics, 4 (2022), pp. 578–594.

[165] I. Razdolski, Y. Chen, A. J. Giles, S. Gewinner, W. Schöllkopf, M. Hong, M. Wolf, V. Giannini, J. D. Caldwell, S. A. Maier, and A. Paarmann, *Resonant Enhancement of Second-Harmonic Generation in the Mid-Infrared Using Localized Surface Phonon Polaritons in Subdiffractional Nanostructures*, Nano Letters, 16 (2016), pp. 6954–6959.

[166] I. Razdolski, N. C. Passler, C. R. Gubbin, C. J. Winta, R. Cernansky, F. Martini, A. Politi, S. A. Maier, M. Wolf, A. Paarmann, and S. De Liberato, *Second harmonic generation from strongly coupled localized and propagating phonon-polariton modes*, Phys. Rev. B, 98 (2018), p. 125425.

[167] X. Hu, T. W. Lo, A. Mancini, C. R. Gubbin, F. Martini, J. Zhang, Z. Gong, A. Politi, S. De Liberato, X. Zhang, D. Lei, and S. A. Maier, *Near-field nano-spectroscopy of strong mode coupling in phonon-polaritonic crystals*, Applied Physics Reviews, 9 (2022), p. 021414.

[168] N. C. Passler, X. Ni, G. Hu, J. R. Matson, G. Carini, M. Wolf, M. Schubert, A. Alù, J. D. Caldwell, T. G. Folland, and A. Paarmann, *Hyperbolic shear polaritons in low-symmetry crystals*, Nature, 602 (2022), pp. 595–600.

[169] X. Ni, G. Carini, W. Ma, E. M. Renzi, E. Galiffi, S. Wasserroth, M. Wolf, P. Li, A. Paarmann, and A. Alù, *Observation of directional leaky polaritons at anisotropic crystal interfaces*, Nature Communications, 14 (2023), p. 2845.

[170] P. Kusch, N. S. Mueller, M. T. Hartmann, and S. Reich, *Strong light-matter coupling in* MoS_2, Phys. Rev. B, 103 (2021), p. 235409.

[171] C. Wolff, K. Busch, and N. A. Mortensen, *Modal expansions in periodic photonic systems with material loss and dispersion*, Phys. Rev. B, 97 (2018), p. 104203.

[172] I. Dolado, C. Maciel-Escudero, E. Nikulina, E. Modin, F. Calavalle, S. Chen, A. Bylinkin, F. J. Alfaro-Mozaz, J. Li, J. H. Edgar, F. Casanova, S. Vélez, L. E. Hueso, R. Esteban, J. Aizpu-

rua, and R. Hillenbrand, *Remote near-field spectroscopy of vibrational strong coupling between organic molecules and phononic nanoresonators*, Nature Communications, 13 (2022), p. 6850.

[173] A. Thomas, J. George, A. Shalabney, M. Dryzhakov, S. J. Varma, J. Moran, T. Chervy, X. Zhong, E. Devaux, C. Genet, J. A. Hutchison, and T. W. Ebbesen, *Ground-State Chemical Reactivity under Vibrational Coupling to the Vacuum Electromagnetic Field*, Angewandte Chemie International Edition, 55 (2016), pp. 11462–11466.

[174] T. W. Ebbesen, *Hybrid Light–Matter States in a Molecular and Material Science Perspective*, Accounts of Chemical Research, 49 (2016), pp. 2403–2412.

[175] J. W. You, Z. Lan, Q. Ma, Z. Gao, Y. Yang, F. Gao, M. Xiao, and T. J. Cui, *Topological metasurface: from passive toward active and beyond*, Photon. Res., 11 (2023), pp. B65–B102.

[176] X. Ni, S. Yves, A. Krasnok, and A. Alù, *Topological Metamaterials*, Chemical Reviews, 123 (2023), pp. 7585–7654.

[177] L. Sun, B. Bai, J. Wang, M. Zhang, X. Zhang, X. Song, and L. Huang, *Probing the Photonic Spin–Orbit Interactions in the Near Field of Nanostructures*, Advanced Functional Materials, 29 (2019), p. 1902286.

[178] J. Dorfmüller, R. Vogelgesang, R. T. Weitz, C. Rockstuhl, C. Etrich, T. Pertsch, F. Lederer, and K. Kern, *Fabry-Pérot Resonances in One-Dimensional Plasmonic Nanostructures*, Nano Letters, 9 (2009), pp. 2372–2377.

[179] D. Rossouw, M. Couillard, J. Vickery, E. Kumacheva, and G. A. Botton, *Multipolar Plasmonic Resonances in Silver Nanowire Antennas Imaged with a Subnanometer Electron Probe*, Nano Letters, 11 (2011), pp. 1499–1504.

[180] O. Nicoletti, M. Wubs, N. A. Mortensen, W. Sigle, P. A. van Aken, and P. A. Midgley, *Surface plasmon modes of a single silver nanorod: an electron energy loss study*, Opt. Express, 19 (2011), pp. 15371–15379.

[181] C. T. Ellis, J. G. Tischler, O. J. Glembocki, F. J. Bezares, A. J. Giles, R. Kasica, L. Shirey, J. C. Owrutsky, D. N. Chigrin, and J. D. Caldwell, *Aspect-ratio driven evolution of high-order resonant modes and near-field distributionsin localized surface phonon polariton nanostructures*, Scientific Reports, 6 (2016), p. 32959.

[182] F. J. Alfaro-Mozaz, P. Alonso-González, S. Vélez, I. Dolado, M. Autore, S. Mastel, F. Casanova, L. E. Hueso, P. Li, A. Y. Nikitin, and R. Hillenbrand, *Nanoimaging of resonating hyperbolic polaritons in linear boron nitride antennas*, Nature Communications, 8 (2017), p. 15624.

[183] Y. Li, R. Qi, R. Shi, N. Li, and P. Gao, *Manipulation of surface phonon polaritons in SiC nanorods*, Science Bulletin, 65 (2020), pp. 820–826.

[184] G. Lu, C. R. Gubbin, J. R. Nolen, T. G. Folland, K. Diaz-Granados, I. I. Kravchenko, J. A. Spencer, M. J. Tadjer, O. J. Glembocki, S. De Liberato, and J. D. Caldwell, *Collective Phonon–Polaritonic Modes in Silicon Carbide Subarrays*, ACS Nano, 16 (2022), pp. 963–973.

[185] J. D. Caldwell, A. V. Kretinin, Y. Chen, V. Giannini, M. M. Fogler, Y. Francescato, C. T. Ellis, J. G. Tischler, C. R. Woods, A. J. Giles, M. Hong, K. Watanabe, T. Taniguchi, S. A. Maier, and K. S. Novoselov, *Sub-diffractional volume-confined polaritons in the natural hyperbolic material hexagonal boron nitride*, Nature Communications, 5 (2014), p. 5221.

[186] S. Dai, W. Fang, N. Rivera, Y. Stehle, B. Jiang, J. Shen, R. Tay, C. Ciccarino, Q. Ma, D. Rodan-Legrain, P. Jarillo-Herrero, E. Teo, M. Fogler, P. Narang, J. Kong, and D. Basov, *Phonon Polaritons in Monolayers of Hexagonal Boron Nitride*, Advanced Materials, 31 (2019), p. 1806603.

[187] N. Li, X. Guo, X. Yang, R. Qi, T. Qiao, Y. Li, R. Shi, Y. Li, K. Liu, Z. Xu, L. Liu, F. J. García de Abajo, Q. Dai, E.-G. Wang, and P. Gao, *Direct observation of highly confined phonon polaritons in suspended monolayer hexagonal boron nitride*, Nature Materials, 20 (2021), pp. 43–48.

[188] D. M. Juraschek and P. Narang, *Highly Confined Phonon Polaritons in Monolayers of Perovskite Oxides*, Nano Letters, 21 (2021), pp. 5098–5104.

[189] D. G. Baranov, C. Schäfer, and M. V. Gorkunov, *Toward Molecular Chiral Polaritons*, ACS Photonics, 10 (2023), pp. 2440–2455.

[190] C. Schäfer and D. G. Baranov, *Chiral Polaritonics: Analytical Solutions, Intuition, and Use*, The Journal of Physical Chemistry Letters, 14 (2023), pp. 3777–3784.

[191] D. G. Baranov, B. Munkhbat, N. O. Länk, R. Verre, M. Käll, and

T. Shegai, *Circular dichroism mode splitting and bounds to its enhancement with cavity-plasmon-polaritons*, Nanophotonics, 9 (2020), pp. 283–293.

[192] J. Guo, G. Song, Y. Huang, K. Liang, F. Wu, R. Jiao, and L. Yu, *Optical Chirality in a Strong Coupling System with Surface Plasmons Polaritons and Chiral Emitters*, ACS Photonics, 8 (2021), pp. 901–906.

[193] D. N. Basov, R. D. Averitt, and D. Hsieh, *Towards properties on demand in quantum materials*, Nature Materials, 16 (2017), pp. 1077–1088.

[194] B. X. Wang and C. Y. Zhao, *Topological phonon polariton enhanced radiative heat transfer in bichromatic nanoparticle arrays mimicking Aubry-André-Harper model*, Phys. Rev. B, 107 (2023), p. 125409.

[195] T. Jia, Z. Cheng, H. Zhao, and H. Kimura, *Domain switching in single-phase multiferroics*, Applied Physics Reviews, 5 (2018), p. 021102.

[196] L. Li, L. Xie, and X. Pan, *Real-time studies of ferroelectric domain switching: a review*, Reports on Progress in Physics, 82 (2019), p. 126502.

List of Acronyms

2D-FFT	two-dimensional fast-Fourier transform
AlN	aluminum nitride
AOM	Acousto-optical modulator
ASE	amplified spontaneous emission
BBO	barium borate
BPhP	bulk phonon polariton
CCD	charge-coupled device
DFG	difference-frequency generation
FEL	free-electron laser
FHI	Fritz Haber Institute
FO	fiber oscillator
FoV	field of view
FTIR	Fourier-transform infrared (spectroscopy)
FWHM	full width half maximum
GaSe	gallium selenide
hBN	hexagonal boron nitride
IR	infrared
KRS-5	thallium bromo-iodide
KTP	potassium titanyl phosphate
linac	linear accelerator
LO	longitudinal optical
LSPhP	localized surface phonon polariton
MO	master oscillator
MoO_3	molybdenum trioxide
MP	micropillar
NA	numerical aperture

nano-FTIR	nano-Fourier transform infrared (spectroscopy)
Nd:Van	neodymium-doped vanadate
Nd:YAG	neodymium-doped yttrium aluminum garnet
OR	optical rectification
PhP	phonon polariton
PP	plasmon polariton
PTIR	photothermal induced resonance (microscopy)
RF	radio frequency
SEM	scanning-electron microscope
SeSAM	semiconductor saturable absorber mirror
SFG	sum-frequency generation
SHG	second-harmonic generation
SiC	silicon carbide
SIM	structured illumination microscopy
s-SNOM	scattering-type scanning near-field optical microscopy
SPhP	surface phonon polariton
SPP	surface plasmon polariton
STED	stimulated emission depletion (microscopy)
STORM	stochastic optical reconstruction microscopy
TD	transverse dipole
TO	transversal optical
UV	ultraviolet
VIS	visible

List of Publications

[P1] Richarda Niemann, Sören Wasserroth, Guanyu Lu, Sandy Gewinner, Marco De Pas, Wieland Schöllkopf, Joshua D. Caldwell, Martin Wolf, and Alexander Paarmann.
Long-wave infrared super-resolution wide-field microscopy using sum-frequency generation.
Appl. Phys. Lett. 120, 131102 (2022)
https://doi.org/10.1063/5.0081817

[P2] Tuhin Khan, Ben John, Richarda Niemann, Alexander Paarmann, Martin Wolf, and Martin Thämer.
Compact oblique-incidence nonlinear widefield microscopy with paired-pixel balanced imaging.
Opt. Express 31, 28792-28804 (2023)
https://doi.org/10.1364/OE.495903

[P3] Richarda Niemann*, Niclas S. Müller*, Sören Wasserroth, Guanyu Lu, Martin Wolf, Joshua D. Caldwell, and Alexander Paarmann.
* These authors contributed equally to this work.
Spectroscopic and interferometric sum-frequency imaging of strongly coupled phonon polaritons in SiC metasurfaces.
arXiv 2311.13284 (2023)
https://doi.org/10.48550/arXiv.2311.13284

Acknowledgements

A lot of people had a great impact on me, my work and finishing this thesis, for which I am extremely thankful.

First of all I would like to thank Martin Wolf. Thank you for supervising my thesis and for the wonderful working atmosphere you created in the department. I am really glad I could make my doctorate at the FHI PC department.

Thanks a lot to Katharina Franke for taking the role as my second supervisor.

My special thanks goes to Alex Paarmann. You are doing an amazing job as a group leader and I could not have asked for any better person for that job. Thank you for being my go-to person for any kinds of problems and discussions and for always being keen to help and find solutions. You created a wonderful atmosphere in the group, with a lot of laughter, fun and sociability next to great research questions and scientific discussions.

It couldn't have been done without the Lattice Dynamics Group. Thanks to the current members Giulia, Dory and Niclas as well as to the former members Sören, Chris, Niko, Riko and Gonzalo. Thanks for the support in the lab, for the karaoke during long beam times, for game nights, after-work beers and picknicks in the park. Without you the time wouldn't have been so much fun and felt so short. It was a pleasure! A special thanks to Sören as my main companion during the first three years and the birth of the microscope. I learned a lot from you and had tons of fun working with you.

A great thank you to the whole PC department. I enjoyed working here the last four years so much, with chats in the kitchen area, great laughs about the current coffee meme and fun times during the workshops and PhD days we shared.

Nothing would have been possible without the FEL team Wieland Schöllkopf, Sandy Gewinner and Marco De Pas. Thank you for running the FEL for my experiments and for putting so much effort in satisfying our beamtime needs as good as possible.

Thanks a lot to our in-house collaborators Ben, Tuhin and Martin for all the meetings we had on SFG microscopy and the knowledge we shared. Outside FHI, it was a pleasure to collaborate with Josh, Guanyu, Chris, Simone, Pablo, Gonzalo und Javier. Thank you for the fruitful discussions we had and for the preparation of all the samples.

A big thank you to all the other experimentalists who shared their problems with me, making disaster tourism possible and showing that it's not only the own experiment which sometimes just does not want to behave.

Thank you so much to the PC Gang, Max^2, Michael, Luis, Joanna, Dory, Ben and Vivien. I enjoyed every coffee break with you, beers in the park, swimming in the lake and all the work and non-work related activities we shared. Thank you for making

the institute feel much more like a home and for being so wonderful companions on my way.

I would like to thank my very much loved friends from home. Thanks to the Seppel, especially in the last year you guys did an amazing job on clearing my mind and distracting me from work stress and making me relax. I promise, I will stop talking so much about my work - at least I'll try.
Thanks to Marcel for all your effort and doing an amazing job on keeping my mind sane in stressful work times as well as in chaotic corona times. I know, it was far from easy sometimes.
Thank you, Tobi, for teaching me my experimental skill set, for planting the wish of building my own experiment in my head after we spent so much time on yours, and for staying a mentor even after my graduation. Thanks for all the great hikes we had, the amazing spots we camped on, the beautiful views we shared and for all of these to come.

A special thanks to Niclas, Michael and Tobi for proof-reading my thesis so carefully and to Olli for the latex support.

Lastly, I want to thank my wonderful family. Thank you for your love and for supporting me on my way, no matter which direction I take. Most important, Fritzi, thank you for your infinite optimism and your ability to always cheer me up.

Declaration of Authorship

I declare to the Freie Universität Berlin that I have completed the submitted dissertation independently and without the use of sources and aids other than those indicated. The present thesis is free of plagiarism. I have marked as such all statements that are taken literally or in content from other writings. This dissertation has not been submitted in the same or similar form in any previous doctoral procedure.

I agree to have my thesis examined by a plagiarism examination software.

Berlin, December 20, 2023

_____

Richarda Niemann